



Resolving 3D coseismic deformation of the 2019 Mw 7.1 Ridgecrest earthquake using radar and optical data

Institute of Photogrammetry

Geodesy and Geoinformatics Master of Science

by

CAROLINA CAÑIZARES

submitted to:

Prof. Dr. Mahdi Motagh

Hannover, February 28, 2020

Contents

1	Introduction	1
1.1	Motivation	1
1.2	Objective	2
1.3	Related work	2
1.4	Outline	3
2	Fundamentals	5
2.1	Observing Systems	5
2.1.1	Radar Systems	5
2.1.2	Optical Systems	11
2.2	Sentinel Missions	14
2.2.1	Sentinel-1 Mission	14
2.2.2	Sentinel-2 Mission	17
2.3	Least Squares Adjustment (LSA)	19
2.3.1	Non-weighted Least Squares Adjustment	20
2.3.2	Weighted Least Squares Adjustment	21
3	Methodology	25
3.1	Study Area	25
3.2	3-Dimensional Decomposition	25
3.2.1	Interferometry processing	27
3.2.2	Offset Tracking processing	29
3.3	Radar and Optical Observations Combination	37
3.3.1	Functional Models	39
3.3.2	Stochastic Models	40
4	Results	53
4.1	3-Dimensional Decomposition	53
4.1.1	Sentinel-1 (Interferometric + Offset Tracking)	53
4.1.2	Sentinel-1 (Interferometric + Offset Tracking) + Sentinel-2	54
4.1.3	Sentinel-1 (Interferometric) + Sentinel-2	55
4.2	Validation	59
4.3	Limitations	72
4.4	Conclusions	73
A	Phase Interferometric Processing	75

B Amplitude Offset Tracking Processing	79
C Cosi-Corr Image Processing	83
D MicMac Image Processing	85
D.1 Image format conversion	85
D.2 MicMac MM2DPosSism command runnig	86
D.3 Pixel to metric displacement conversion	87
D.4 Additional processing steps	87
Bibliography	93

1 Introduction

1.1 Motivation

Measuring displacements associated with earthquakes offers information such as the geometry of the rupture fault, the released energy and the ground displacement. Nowadays, there is more than one method that allows to retrieve this information. The geodetic data most extensively used in earthquake source imaging are Global Navigation Satellite System (GNSS) and Interferometric Synthetic Aperture Radar (InSAR) observations. The GNSS technique is based on field measurements, however; the fault area is normally hard to access and complex fault ruptures are not easy to be detected in the field. Additionally, depending on the fault slip extend, it can only be measured in a specific number of locations. The drawback in this case is that the coverage from GNSS observations is sparse and it is not possible to measure the area if it is not kept under surveillance. On the other hand, by using satellite imagery, it is possible to cover large areas so that the fault rupture can be partially or totally visible. The satellites can be equipped either with radar or optical sensors. The problem of the radar observing technique is that it cannot provide displacement maps in the near-field of the fault due to large displacement, causing phase decorrelation. In addition, techniques such as InSAR, are mostly sensitive to changes in distance along the line of sight (LOS), meaning that it provides only one component of the surface displacement vector [Sudhaus and Jónsson, 2009]. In contrast, the main advantage of radar technique over the optical is that the waves, emitted from a pulse-generating device linked to the radar system antenna, propagate through atmospheric media without almost no signal loss, providing all weather conditions capabilities [Massonnet and Feigl, 1998]. Furthermore, radar sensors are active sensors, which means that they provide their own energy source, while optical are passive sensors that depend on external energy sources to capture an scene. The advantages and disadvantages of all these techniques are important to be considered when monitoring rapid phenomena, such as earthquakes, volcanic eruptions, glacier movements, flooding, etc [Yun, 2007]. For this reason, the study of such events can be better monitored and analyzed if a combination of these different techniques is applied, taking advantage of their individual benefits, but bringing them together for a greater contribution, which in this study is the 3-dimensional decomposition of ground displacement occurred after an earthquake.

1.2 Objective

The objective is to provide a methodology to retrieve information in the near-field of an earthquake affected area by combining radar and optical measuring techniques, by also considering different weighting cases for the observations. This methodology is applied in the surroundings of Ridgecrest, California, which was affected after a M_w 6.4 and M_w 7.1 earthquake that took place on July, 2019. There are already studies which have focused their attention in this particular earthquake. However, this case was motivated by the fact that the combination of radar and optical images for 3-dimensional displacement retrieval, obtained from weighted and non-weighted least squares adjustment, has not yet been assessed before. In this way, the expected results will contribute to have a better understanding of the affected area and its surroundings, which leads not only to a better monitoring of the fault and the mitigation of possible future risks within the study area, but also to replicate this methodology in any other place of the world where ground displacement has been observed from radar and optical sensors.

1.3 Related work

InSAR is a 1-dimensional imaging technique, which provides the phase difference between repeated SAR acquisitions of the same spot on the ground. The phase difference is related to the change in distance from the antenna to the spot, along the satellite LOS, meaning that each pixel in the InSAR interferogram provides information on the displacement projection along its LOS [Bechor, 2006]. For this reason, a limiting factor of the InSAR technique is that it can only measure 1-dimensional ground motion. Therefore, the decomposition from 1-dimensional to 3-dimensional displacement has already been studied from different approaches, which includes: **a)** InSAR only based methods combining range and azimuth measurements (see [Fiako, 2001], [Wright et al., 2004], [Hu et al., 2014], [Gradin et al., 2016], [Mehrabi et al., 2019]) and assessing alternative acquisition geometries from different incidence and heading angles (see [Wright et al., 2004]), **b)** InSAR and GNSS observations combination (see [Hu et al., 2012]), **c)** InSAR based methods using an a priori and geophysical models (see [Motagh et al., 2010]), and **d)** optical based data only applying offset tracking methods (see [Van Puymbroeck et al., 2000], [Milliner and Donnellan, 2020]). The combination of interferometric phase observations with amplitude offset tracking was first implemented by [Fiako, 2001], but the development of all these related works have brought the possibility to better constraint physical models, such as earthquake and volcano source models [Simons and Rosen, 2015], and by constraining sources of deformation in geophysical phenomena [Mehrabi et al., 2019] better understanding, and thus risk management, can be achieved. The aggregated value of the proposed methodology is the implementation and analysis of different weighting criteria applied for three different combinations of observations using radar and optical observations.

1.4 Outline

The study case has been organized in four chapters. Chapter 2 provides the theoretical background concerning the radar and optical observation techniques, and the description of the sensors which provided the images before and after the earthquake of interest. In addition, the most important theory of Least Squares Adjustment (LSA), weighted and non-weighted, is also described. Having understood these concepts, chapter 3 provides the detailed explanation of the methodology which has formulated for this case, together with the description of all the generated displacement maps used as input data for the 3-dimensional decomposition. Additionally, an overview of the functional and stochastic models that belong the adjustment methodology is also part of this chapter. Finally, chapter 4, presents the results of the decomposition for each of the cases which were formulated, with their corresponding validation, and the most important conclusions and suggestions for possible future work. The last part of the document compiles all the detailed description of the processing steps applied in different, free and commercial, used software.

2 Fundamentals

This chapter compiles the most important concepts concerning the principles behind the radar and optical acquisition techniques and their corresponding satellite missions. Moreover, an insight in the Least Square Adjustment (LSA) theory and the semi-variogram estimation process is also presented. The goal of the chapter is to give the needed information that leads to the possibility of easily interpret the implemented methodology (chapter 3) and the result (chapter 4) of the 3-dimensional decomposition.

2.1 Observing Systems

The data acquisition system mostly consists of sensor and the platform on which the sensor resides. The platform may be on the surface, in the air or in space. Spacelborne platforms are mainly satellites and space shuttles. Considering satellite sensor systems only, they are classified in two types: active and passive. Passive sensors detect natural radiation that is emitted by the object being viewed or reflected by the object from a source other than the instrument. Reflected sunlight is the most common external source of radiation sensed by this type of sensors. On the other hand, active sensors provide their own electromagnetic radiation to illuminate the scene they observe. They send a pulse of energy from the sensor to the scene and then receive the radiation that is backscattered from that scene [Liang et al., 2012]. The most important concepts of these two types of sensors are given in the following sections.

2.1.1 Radar Systems

Radio Detection and Ranging (Radar), is referred to a technique but also to an instrument for measuring the distance of objects. When talking about radar instrument, it works by emitting electromagnetic pulses in the radio and microwave regime and detecting the reflected pulses from the objects in its line of sight (LOS) [Skolnik, 1981]. Radar instruments operate between 1 mm to 1 meter, this means, in the microwave portion of the electromagnetic field. The microwave region includes K (1.5 cm), X (3 cm), C (6 cm) and L (24 cm) bands. A radar instrument

is also characterized for being an active sensor system, which means that it provides its own electromagnetic energy. The main benefits of systems operating with long wavelengths are the improvement of signal penetration, mainly in the atmosphere, and that their operation is independent of weather conditions [Henderson and Lewis, 1998]. For example, in Europe only 10% of all acquired optical data are useful for topographic mapping due to cloud cover while, especially over tropical regions, cloud cover is almost continuous, whereas high-altitude regions are not illuminated by the sun for several months per year [Hanssen, 2001].

The radar technique uses the two-way travel time of the pulse to determine the range to the detected object and its backscatter intensity to infer physical quantities such as size or surface roughness [Skolnik, 1981]. A signal of electromagnetic energy is transmitted from the sensor antenna, a part of the terrain is illuminated and reflected, and the reflected signal from the target surface is measured back on the sensor. The backscattered energy is amplified and analyzed so that location, electrical properties and surface configuration of the objects can be determined [Henderson and Lewis, 1998] [Gupta, 2003].

For some time, radar has been used as a remote sensor of the weather. It was also used in the past to probe the moon and the planets (radar astronomy). The contribution of radar to remote sensing includes the measurements and mapping of sea conditions, water resources, ice cover, agriculture, forestry conditions, geological formations, and environmental pollution [Skolnik, 1981].

2.1.1.1 Real Aperture Radar (RAR)

These radar system were commonly used in initial stages. As previously explained, the technique performs observations which consist on emitting pulses, and the reflections from larger ranges arrive back at the instrument after proportionately larger time. The observation direction becomes the **range** direction. When the next pulse is transmitted, the radar instrument will have moved forward a relative short distance so that a slightly different strip of the surface will be imaged. These strips are then recorded side by side to build up the **azimuth** direction observations. In consequence, the image consists on a two-dimensional array [ESA, 2019b], as shown in figure 2.1.

The pulse of the electromagnetic energy illuminates the ground pointing to the side rather than in vertical direction (see section **a** in figure 2.2). This means that the path of the radar signal is oblique to the surface being imaged. The reason of this imaging system is that targets located at different distance from the radar sensor are better distinguished from a side-looking system [Dzurisin, 2007]. The side-looking distance from the sensor to the object is known as **slant range**. The echoes are received in order of arrival. The received signal is then converted into time-amplitude signal (see section **b** in figure 2.2).

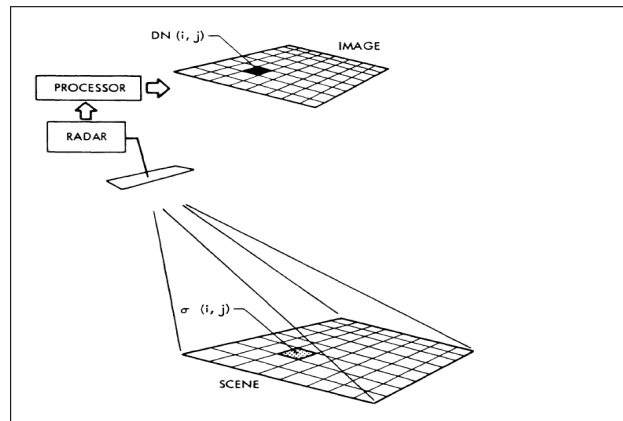


Figure 2.1: Radar system scene [Gupta, 2003]

Once the last echo is received, a new pulse of energy is emitted in the range direction. The closest and the farthest pulse define the **swath** width, which is the length between the **near range** to the **far range**. At the same time, the sensor moves along its trajectory in the azimuth direction, so that the radar beam sweeps perpendicular to the flight path, covering the terrain. The observations from the near to the far field are characterized by three formed angles from the relation between the antenna, incident ray and ground object. The **depression angle** is described by the transmitted ray and the horizontal plane, being smallest at the far range, and largest at the near range. The **look angle** is defined between the transmitted ray and the vertical plane. And the **incidence angle** is obtained from the intersection of the incident ray and the vertical on the ground. These three angles are shown in figure 2.3 [Gupta, 2003].

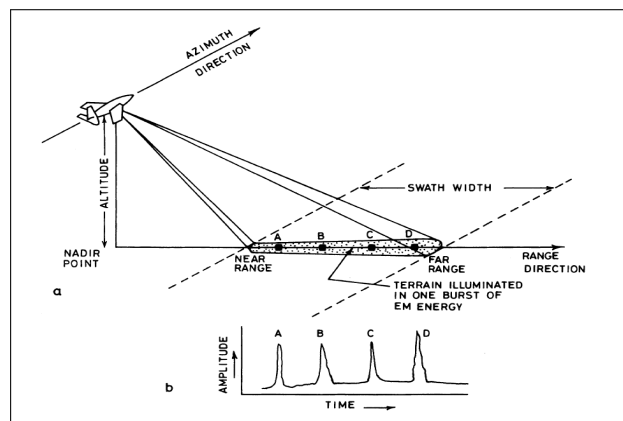


Figure 2.2: Radar working principle [Gupta, 2003]

The collected data result in an azimuth and range dimension, which in consequence, the image resolution is also defined in range and azimuth direction [Gupta, 2003]. The range resolution is the shortest range difference at which two scatters can be distinguished, defined by equation 2.1,

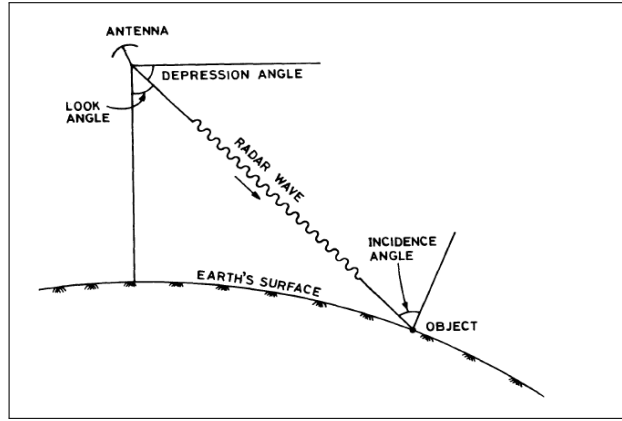


Figure 2.3: Radar system angles [Gupta, 2003]

$$R_r = \frac{\tau * c}{2 * \sin(\theta)} \quad (2.1)$$

where τ represents the emitted pulse duration, c is the speed of light and θ corresponds to the look angle. The product from the numerator defines the physical length of the signal, which explains why the shorter the pulse length, the finer the range resolution. However, there is always a trade-off because since the energy of the received pulse is 10^{-11} orders of magnitude smaller than the energy of the emitted pulse, the total energy illuminating the target is diminished and the signal can become too weak to be recorded as the pulse length reduces. Because the signal follows two ways, travelling to the target and returning back to the satellite, the range resolution is divided by factor 2. Additionally, as range resolution is defined in the ground, it varies across the ground range. Therefore, it is inversely proportional to the look angle, which means that for targets located in the near range the resolution is coarser than for targets at the far range [Henderson and Lewis, 1998] [Hanssen, 2001].

Likewise, azimuth resolution is the capability of discriminate targets situated in the azimuth direction and defined by equation 2.2,

$$R_a = R * \frac{\lambda}{L} \quad (2.2)$$

being R the slant range distance, λ the wavelength, and L is defined by the length of the antenna. Consequently, the longer the wavelength, the coarser the azimuth resolution. For example, X band sensors provide a better azimuth resolution than C and L band sensors. Moreover, the azimuth resolution is inversely proportional to the length of the antenna, which means that the resolution is finer as the antenna is longer. Ideally, the azimuth resolution is improved when a shorter wavelength, a smaller slant range and a larger antenna length is used. This ideal

case is however not easy to handle. Shorter wavelengths are attenuated in the atmosphere, reducing the slant range produces a coarser range resolution, and increasing the antenna length has, of course, physical limitations [Gupta, 2003]. However, the antenna length constraint has been solved by synthesizing a larger antenna, which is described from the next two types of radar systems: Synthetic Aperture Radar (SAR) and Interferometric Synthetic Aperture Radar (InSAR).

2.1.1.2 Synthetic Aperture Radar (SAR)

As explained in section 2.1.1.1, RAR systems show that their basic limitation is the insufficient azimuth resolution when the range distance increases. Additionally, objects which are located farther away from the sensor, are observed for a longer duration (greater number of sweeps). SAR systems are the solution for a finer azimuth resolution by synthesizing the antenna length. All the observations are integrated and successive antenna positions are treated as if they were individual elements of one long antenna array [Gupta, 2003] as shown in figure 2.4. This methodology leads to an increase in three orders of magnitude in the azimuth resolution. Equation 2.2 is then expressed as equation 2.3,

$$R_a = \frac{l}{2} \quad (2.3)$$

with l being the antenna length. In this sense, the most obvious differences between equation 2.2 and 2.3 are the omission of range distance and wavelength, and that the antenna length is directly proportional to the resolution.

SAR mapping systems are normally operated from airborne and spaceborne platforms. The radar signal is acquired as a complex signal comprising real and imaginary components. These values contain information about the amplitude and the phase based on the relation shown in equation 2.4 and 2.5, respectively

$$Amplitude = \sqrt{(Imaginary^2) + (Real^2)} \quad (2.4)$$

$$Phase = \arctan \frac{Imaginary}{Real}. \quad (2.5)$$

2.1.1.3 Interferometry Synthetic Aperture Radar (InSAR)

As previously mentioned, two objects at an identical range are indistinguishable because points located near the vertical are almost at the same range from the radar, which means that radars cannot look directly at the nadir. The solution for this problem is coming from nature, the use of two sensors observing from different

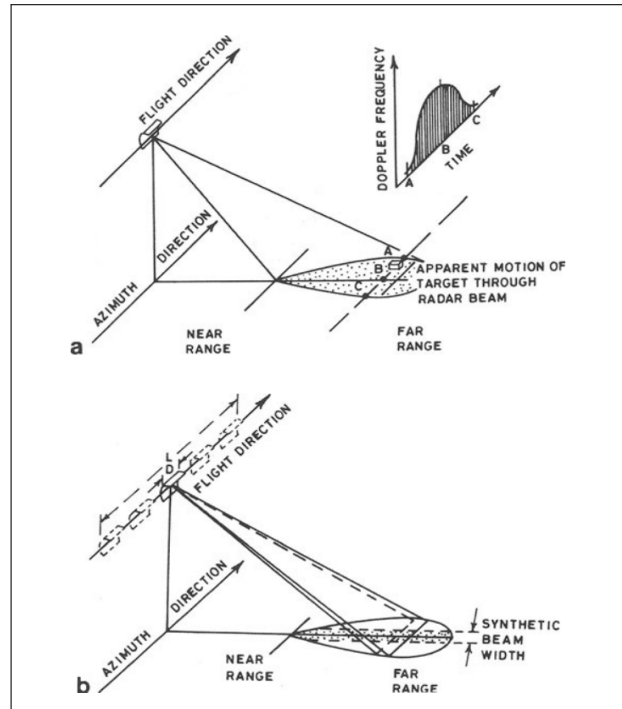


Figure 2.4: SAR working principle [Gupta, 2003]

angles. Using SAR images, acquired by two different antennas or using repeated acquisitions, it is possible to obtain distances as well as angular measurements [Hanssen, 2001] [Massonnet and Souyris, 2008].

Considering phase information only, the amount of phase of a single image may not be of any particular utility, but the phases of two SAR images of the same ground scene, acquired from slightly differing angles, possess phase difference. Therefore, the difference in slant ranges from two antenna positions can be measured with fractional wavelength accuracy in terms of phase difference. This characteristic is the basic strength of the SAR interferometry technique [Gupta, 2003].

Interference takes place when the phase of two different waves are not aligned because two images of the same scene cannot be overlaid directly, especially when the sensors follow a repeated orbit sensing from nearly the same or slightly divergent looking angle every pass, as shown in figure 2.5. This situation makes it necessary to resample one image to remove a linear shear. Then one image is multiplied by the complex conjugated of the other resulting in phase difference or interferogram [Gabriel et al., 1989].

Interferometry is classified in additive and multiplicative. The signal resulting from the additive interferometry is obtained by the incoherent summing of the amplitudes of two input signals, which result in amplitude fringes. In multiplicative interferometry, the interferometric phase is measured by coherent cross-multiplication of the two input signals. The phase data imply a high accuracy,

as the fraction of the phase cycle is accurately determine. In 2D applications, a 2π phase cycle is often referred to as a fringe [Hanssen, 2001] [Rosen, 2014] [ESA, 2019b].

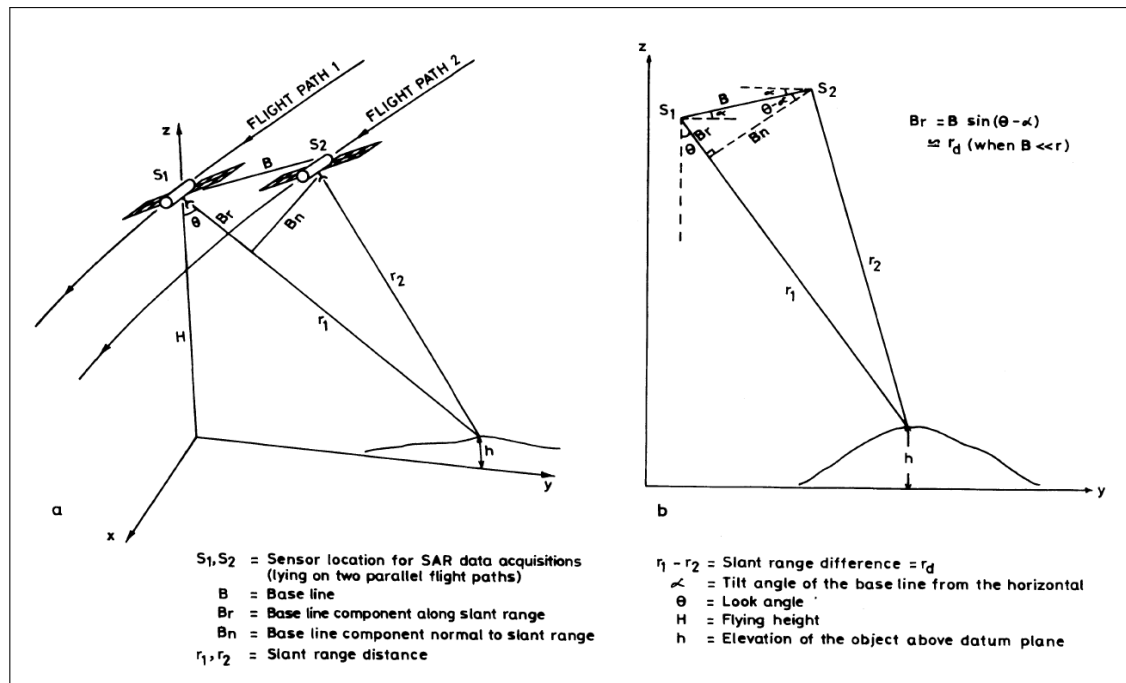


Figure 2.5: Interferometry principle [Gupta, 2003]

The drawback in this application is that the deformation signal is always mixed with topographic signal. The solution is already known as differential interferometry, where the topographic signal obtained from a Digital Elevation Model (DEM), is scaled to the deformation interferogram and subtracted from it, yielding in a differential interferogram [Hanssen, 2001]. Deformations on or around a fault, such as interseismic, aseismic, coseismic and postseismic events, changes of magma chambers of a volcano's plumbing system, and movements of land or glaciers, are part of the applications that can be assessed by using InSAR [Simons and Rosen, 2015].

2.1.2 Optical Systems

Satellite remote sensing started with optical-mechanical scanners working in the visible and infrared portion of the electromagnetic spectrum, making images from the emitted and reflected radiation from the Earth's surface and overlaying atmosphere, as shown in figure 2.6 [Emery and Camps, 2017] [IREA, 2020].

The strong interaction of the electromagnetic radiation at optical frequencies with the atmosphere and the presence of clouds constitute an important limiting factor

on the potential observation of the Earth surface. Similar to radar systems, optical remote sensing measurements collect radiation reflected and emitted from the observed surface; however, the difference relies on the source of energy. Optical sensors are passive, meaning that they do not provide their own energy but depend on external energy sources, such as the Sun. The data acquisition is realized with sensors that utilize optical instruments, lens for refraction or mirrors for reflection [IREA, 2020] [Hanssen, 2001].

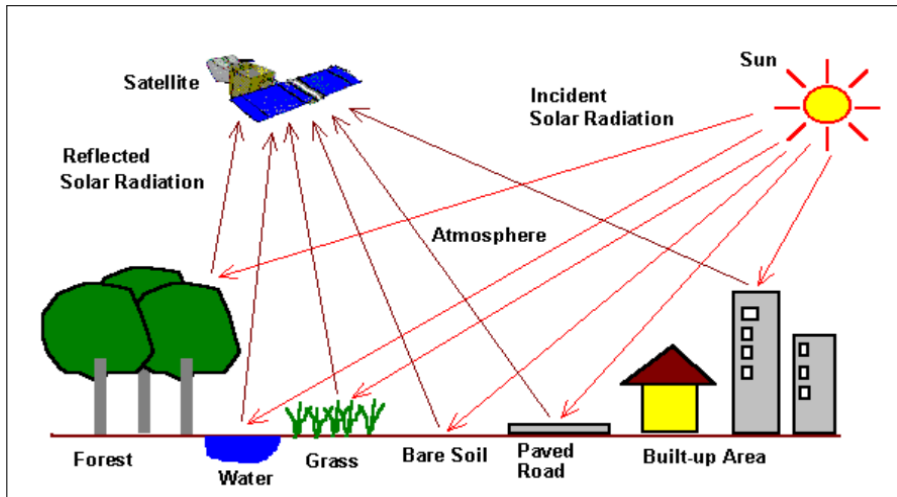


Figure 2.6: Optical remote sensing sensing technique [CRISP, 2001]

Optical remote sensing systems are classified depending on the number of spectral bands used in the imaging process [CRISP, 2001]:

- **Panchromatic imaging system:** The sensor is only a single channel detector sensitive to radiation within a broad wavelength range. When the wavelength range coincides with the visible range, the resulting images resemble black and white images, while the spectral information, or colour, is lost. The physical quantity measured is the brightness of the targets.
- **Multispectral imaging system:** The sensor is a multichannel detector with a few spectral bands. Each of these channels is sensitive to radiation within a narrow wavelength band. The resulting image is a multilayer image, which contains the brightness and spectral information of the sensed targets.
- **Superspectral imaging system:** The sensor has typically more channels than the multispectral sensor. The bands have narrower bandwidths, enabling the finer spectral characteristics of the targets to be captured.
- **Hyperspectral imaging system:** The imaging system is also known as an imaging spectrometer, and the sensor is capable of acquiring images in about a hundred or more contiguous spectral bands. The precise spectral information enables a better characterization and identification of targets, shown in image 2.7.

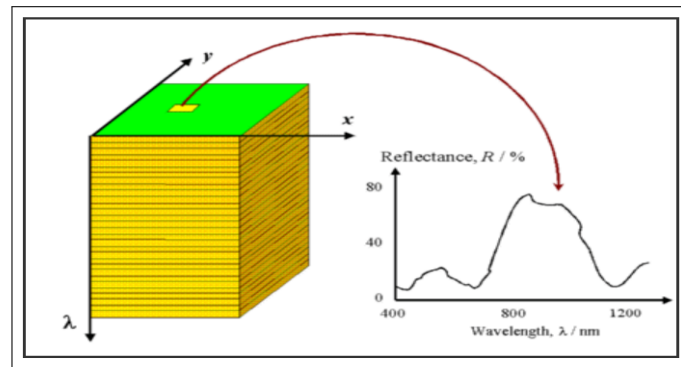


Figure 2.7: Hyperspectral image representation [CRISP, 2001]

Independently of the imaging system, all of those types of acquisitions are described by the following four types of resolutions [Khorram et al., 2012]:

- **Spatial resolution:** Is the measure of the fineness of detail of an image, referring to the ground area captured by a single pixel.
- **Spectral resolution:** Is represented by the width of the wavelength interval and/or number of spectral bands captured by the sensor, defines the storage of recorded electromagnetic energy and the sensor's ability to detect wavelength differences between objects.
- **Temporal resolution:** Is the time that takes a sensor to revisit a particular geographic location.
- **Radiometric resolution:** Is the sensitivity of a sensor to brightness values, the smallest differences in intensity that be detected.

Additionally, the acquisition of the systems are mainly two: across-track and along-track. The simplest is the across-track scanner, which can be subdivided in two types. The first across-track acquisition mode performs image capturing by using a rotating mirror that moves at a constant rate synchronized with the orbit of the satellite so that it increments the image each scan line. The second across-track acquisition mode is known as whisk-broom scanner because it uses an optical system that oscillates back and forth across the scan line, and relies on the forward motion of the spacecraft to increment the image one line at a time. On the other hand, the along-track scanners, also referred as push-broom scanners, samples the entire line, and at the same time using an across-track array. Figure 2.8 shows the across-track (left) and the along-track (right) scheme of the capturing concept, respectively.

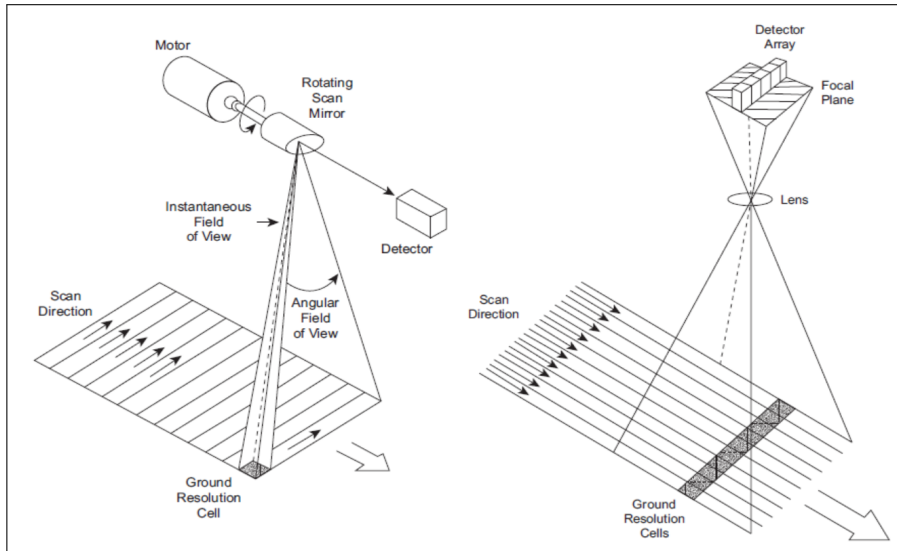


Figure 2.8: Across-track (left) and along-track (right) imaging sensors [CRISP, 2001]

2.2 Sentinel Missions

Sentinel satellites missions were created in order to provide information and support the operational needs of the Copernicus programme, headed by the European Commission (EC) in partnership with the European Space Agency (ESA). The goal of Sentinel program is to replace older Earth retired observation missions or which are reaching the end of their operation life span. In this way, it will possible to ensure a continuity of data so that studies are not affected by gaps. Each of the missions focus on different aspects of Earth observation, atmospheric, oceanic and land monitoring, and the data can be used in a diverse possibilities of applications [ESA, 2019a]. Sentinel-1 and Sentinel-2 missions are further explained in the next section.

2.2.1 Sentinel-1 Mission

Sentinel-1 platform operates a as C-band synthetic aperture radar system which has been used in applications such as monitoring sea-ice zones and polar environment, mapping in support of humanitarian aid in crisis situations, surveillance of marine environments, monitoring land surface motion risks and mapping of forest, water and soil [ESA, 2012].

This mission is composed of two satellites, Sentinel-1A and Sentinel-1B, both moving around the Earth in the same orbit. This configuration satisfies requirements within the resolutions specified in table 2.1.

Table 2.1: Sentinel-1 specifications [ESA, 2019c]

Resolution	Specifications
Spectral	5.405GHz (5.5 cm)
Spatial	5x5 m to 20x20 km
Temporal	12 days (Sun-synchronous)

Because of the orbit of the satellites, each satellite passes a certain location from south to north, known as the ascending orbit, and from north to south, called also descending orbit, as shown in figure 2.9.

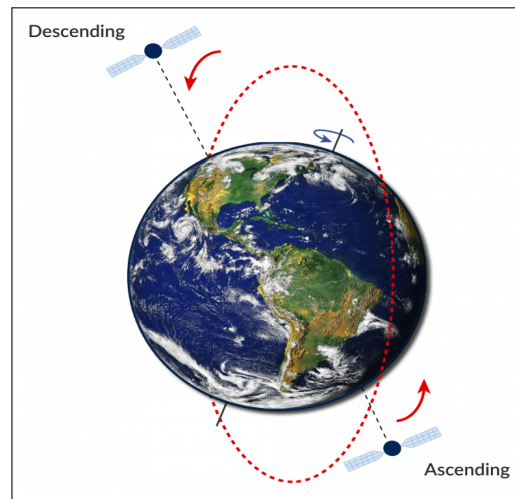


Figure 2.9: Sentinel-1 ascending and descending orbits [SkyGeo, 2020]

Based on current requirements, Sentinel-1 mission is operating in Interferometric Wide swath (IW) and Wave (WV) mode, but for continuity reasons and emerging user requirements, also Stripmap (SM) and Extra-Wide swath (EW) modes are in operation [ESA, 2012]. Figure 2.10 shows the operation of these four modes.

In order to meet the demanding image quality and swath width requirements, the IW mode operates under a steering beam observing in the range (ScanSAR) and azimuth (TOPSAR) direction.

- **Scanning Synthetic Aperture Radar (ScanSAR):** Steering beam in range direction imaging three sub-swaths.
- **Terrain Observation by Progressive Scans Synthetic Aperture Radar (TOPSAR):** Steering beam backward and forward in the azimuth direction imaging nine bursts per sub-swath.

The IW - TOPSAR observation mode allows the combination of a large swath width of 250km with the spatial resolution of 5x20m on the ground, allowing to harmonize the performance in the along-track direction, reducing scalloping, and

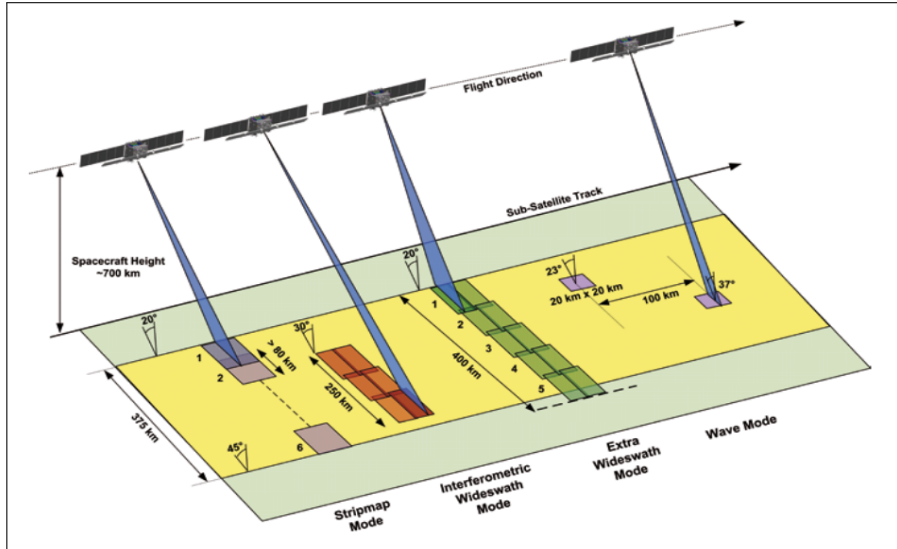


Figure 2.10: Sentinel-1 product modes [ESA, 2012]

providing an homogeneous image quality [ESA, 2012] [Veci, 2015]. The images obtained with this mode are classified in three levels.

- **Level-0:** Consists of compressed unfocused SAR raw data.
- **Level-1:** Produces Single Look Complex (SLC) and Ground Range Detected (GRD). SLC products consist of data comprising complex imaginary with amplitude and phase. GRD products consist of focused multi-looked intensity (amplitude) only data.
- **Level-2:** Consists data for retrieved geophysical parameters of the ocean.

The most demanded product data by users is Level-1, and in this study it is not the exception. Level-1 data is obtained after algorithms application into Level-0 data, and in the same way, Level-2 products are obtained based on processing Level-1 data. Level-1 SLC products are focused SAR data provided in in slant-range geometry. Slant range refers to the natural radar range observation coordinate, defined as the line of sight from the radar sensor to the reflecting object. SLC in the IW mode are made of three sub-swaths so that it has three images in single polarization and six images in dual polarization. Each sub-swath consist of nine burst observed in the azimuth direction. Images for all bursts in all sub-swaths are re-sampled to a common pixel spacing grid in range and azimuth direction [ESA, 2019c]. There are common and particular properties for each of the three sub-swaths, as defined in table 2.2. The SLC products used in this study can be seen in figure 2.11.

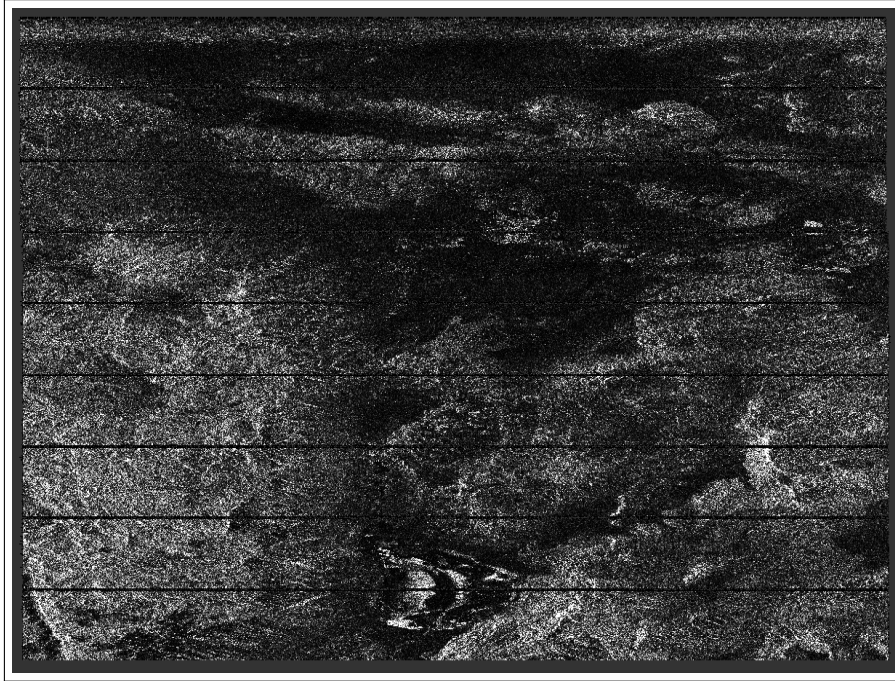


Figure 2.11: Level-1 SLC product (Intensity - Swath 2 - VH polarization)

Table 2.2: SLC product - IW mode properties [ESA, 2019c]

Properties	IW1	IW2	IW3
Spatial resolution rg x az [m]	2.7x22.5	3.1x22.7	3.5x22.6
Pixel spacing rg x az [m]	2.3x14.1		
Incidence angle [°]	32.9	38.3	43.1
Ground range coverage [km]	251.8		
Coordinate system	Slant range		

2.2.2 Sentinel-2 Mission

Similar to Sentinel-1 mission, Sentinel-2 comprises a constellation of two polar-orbiting satellites placed in the same sun-synchronous orbit, phase at 180° to each other. This platform has the mission to work for multispectral imaging for applications such as land cover and land usage change detection maps, geophysical variable maps, risk mapping and fast images for disaster relief efforts [ESA, 2020a].

The difference from Sentinel-1 mission is that Sentinel-2 carries an optical Multispectral Instrument (MSI) that samples 13 spectral bands observing a swath width of 290 km. The resolution specifications are shown in table 2.3.

Table 2.3: Sentinel-2 specifications [ESA, 2020a]

Resolution	Specifications
Radiometric	12 bits
Spectral	From VNIR (443 nm) to SWIR (2190 nm)
Spatial	10 m, 20 m and 60 m
Temporal	10 days (Sun-synchronous)

The spatial resolution of the 13 multispectral observed bands by the Sentinel-2 sensor is classified in three groups, 10 m, 20 m and 60 m. Figure 2.12 shows the spectrum of the four bands with the highest possible spatial resolution.

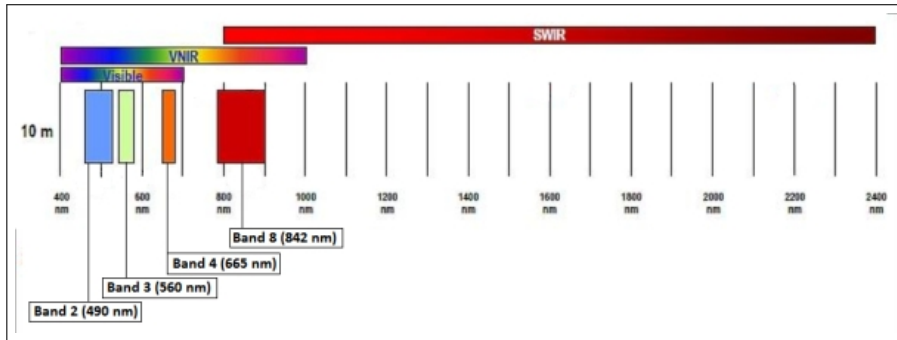


Figure 2.12: Sentinel-2 level-1C 10 m spatial resolution bands [ESA, 2020a]

The elementary level of Sentinel-2 MSI products are granules of a fixed size. A granule, also called tiles, is the minimum indivisible partition of a product containing all possible spectral bands and is dependent on the product level [ESA, 2020a].

- **Level-0, Level-1A and Level-1B:** These granules are a sub-image of a given number of lines along track. All these three products are not available for users.
- **Level-1C and Level-2A:** The image is divided into 100 km tile, generating $100 \times 100 \text{ km}^2$ orthoimages in UTM/WGS84 projection. These two products are available for users.

Level-1C processing includes radiometric and geometric corrections including orthorectification and spatial registration on a global reference system with sub-pixel accuracy while Level-2A processing includes a scene classification and an atmospheric correction applied to Top-Of-Atmosphere (TOA) Level-1C orthoimage products. Level-2A main output is an orthoimage Bottom-Of-Atmosphere (BOA) corrected reflectance product [ESA, 2020a]. One of the level-1C products used for this study case is shown in figure 2.13.



Figure 2.13: Level-1C product

2.3 Least Squares Adjustment (LSA)

In geodesy and geoinformatics, observations are normally collected with the aim of estimating parameters. Very frequently, one has to handle overdetermined systems equations. It means that there are more equations than unknowns so that the solution can be interpreted in the least squares sense [Awange et al., 2010], also called the Least Square Adjustment (LSA) method. LSA satisfy the condition from equation 2.6,

$$\sum v^2 = (v_1^2 + v_2^2 + v_3^2 + \dots + v_n^2) = \textit{minimum} \quad (2.6)$$

where n is the number of observations and v represents the residuals between observations and the estimation of the most probable value. Therefore, LSA condition states that the most probable value for a quantity obtained from repeated observations of equal weight is the value that renders the sum of the squared residuals a minimum. This condition is considered to be the fundamental principle of LSA where the observations have equal or unit weight. However, the more general case assumes that the observations have varying degrees of precision and thus, different weights [Ghinali, 2018].

Considering the case in which the observations do not have equal precision, the most probable value of a quantity obtained from repeated observations having var-

ious weights is that value that renders the sum of the weight times their respective squared residual a minimum, expressed by equation 2.7

$$\sum wv^2 = (w_1v_1^2 + w_2v_2^2 + w_3v_3^2 + \dots + w_nv_n^2) = \text{minimum}. \quad (2.7)$$

The only difference between equation 2.6 and 2.7 is the in incorporation of the weights w for each of the observations.

The mathematical model for an adjustment is the combination of an stochastic model and a functional model. Both models must be correct if the adjustment is to yield the most probable values. The stochastic model is the one related to the determination of variances, and subsequently to weights. On the other hand, the functional model in adjustment computations is an equation or set of equations that represents an adjustment condition. For these reason, it is just as important to use a correct stochastic model as it is to use a correct functional model [Ghinali, 2018].

2.3.1 Non-weighted Least Squares Adjustment

For the case in which no weights, or unit weights are assumed, the functional model is described by the observation equations described as shown in expression 2.8,

$$AX = L + V \quad (2.8)$$

with,

$$A = \begin{bmatrix} a_{11} & a_{12} & a_{13} & \dots & a_{1n} \\ a_{21} & a_{22} & a_{23} & \dots & a_{2n} \\ \cdot & \cdot & \cdot & \cdot & \cdot \\ \cdot & \cdot & \cdot & \cdot & \cdot \\ \cdot & \cdot & \cdot & \cdot & \cdot \\ a_{m1} & a_{m2} & a_{m3} & \dots & a_{mn} \end{bmatrix} \quad X = \begin{bmatrix} x1 \\ x2 \\ x3 \\ \dots \\ xn \end{bmatrix} \quad L = \begin{bmatrix} l1 \\ l2 \\ l3 \\ \dots \\ ln \end{bmatrix} \quad V = \begin{bmatrix} v1 \\ v2 \\ v3 \\ \dots \\ vn \end{bmatrix}$$

where A represents the coefficients of the unknowns, defined in X , while L contains the observations and V the residuals. Employing matrix algebra, the unknowns are defined by equation 2.9

$$X = (A^T A)^{-1}(A^T L). \quad (2.9)$$

For a unique solution, the number of equations has to be the same as the number of unknowns. Usually, the number there are more observations, hence equations,

than unknowns, which is in fact the why is possible to determine the most probable value of the unknowns based on LSA [Ghinali, 2018].

2.3.2 Weighted Least Squares Adjustment

The weighting of the observations controls the amount of correction that each observation receive during the adjustment [Ghinali, 2018]. Therefore, the essential prerequisite for unknowns estimation is the knowledge of the weights of the measured quantities. When the weights are not adequately known but are hypothetically established, it leads to systematic deviations in the results [Kubik, 1970] [Sudhaus and Jónsson, 2011].

In the case of performing calculations that involve multiple interferograms or a combination of different products, it is important to assess the error of each data set to weight the observations appropriately. For example, errors in interferograms arise from several different sources. There are noise sources at the radar instrument itself, on the path of the radar waves, at the reflecting surface and errors can be also introduced in the processing of radar records [Hanssen, 2001]. The main sources of errors are electronic noise from the instrument, atmospheric disturbance along radar wave paths, distribution of the scatterers for a given pixel, satellite orbit inaccuracies and Digital Elevation Model (DEM) [Decriem et al., 2010].

Similar to equation 2.8, a system of weighted linear observation equations can be expressed as equation 2.10,

$$X = (A^T W A)^{-1} (A^T W L) \quad (2.10)$$

where the weights are defined by W . When considering images as the observations, the weights are described as the inverse of the variance-covariance matrix of the pixels forming the image. A full variance-covariance matrix is constructed of three primary parts: **1.** the variance of a given pixel on the diagonal, **2.** the intra-image pixel to pixel covariance, and **3.** the image to image covariance.

For the first part, the pixel variance can be estimated from a small patch of pixels. Doing so for each image is important since different interferograms or offset images may have had different amount of filtering applied to them, as well as different amount of temporal decorrelation. The second part of the matrix is represented as the variance-covariance between pixels of the same image, which in many cases, these pixels have been typically assumed to be uncorrelated. This assumption is incorrect and is primarily dependent on the relative distance between pixels. Places close to one another tend to have similar values, whereas ones that are farther apart differ on average [Webster and Oliver, 2007]. When talking about InSAR products, it is well known that data are affected by spatially correlated phase delay that are mainly caused by spatiotemporal changes in water vapor

content in the atmosphere, which is known as the wet tropospheric delay [Hanssen et al., 1999]. One of the methods to built a variance-covariance matix between pixels from the same image is by assuming that errors in the data can be simulated using an exponential function with nugget, fitted to the isotropic experimental semi-variogram [Emardson et al., 2003] [Simons and Rosen, 2015].

Considering that general condition that values at two places near to one another are similar, whereas those at more widely separated places are less so [Webster and Oliver, 2007], the covariance is normally used to determine the relation between two observations, described by equation 2.11,

$$\hat{C}(z_1, z_2) = \frac{1}{n} \sum_{i=1}^n \{z_{i,1} - \bar{z}_1\} \{z_{i,2} - \bar{z}_2\} \quad (2.11)$$

where z_1 and z_2 are the variables, \bar{z}_1 and \bar{z}_2 are their mean values, respectively, and n is represents the number of observations. Extending this expression to random variables, equation 2.11 is then represented by expression,

$$C(x_1, x_2) = E[\{Z(x_1) - \mu(x_1)\} \{Z(x_2) - \mu(x_2)\}] \quad (2.12)$$

with $\mu(x_1)$ and $\mu(x_2)$ representing the mean value of Z at position (x_1) and (x_2) , respectively. The first concern is to understand what happens when (x_1) and (x_2) are the same. This case is known as variance, expressed by equation 2.13

$$C(x_1, x_2) = E[\{Z(x) - \mu\}^2]. \quad (2.13)$$

On the other hand, when (x_1) and (x_2) do not coincide, the covariance depends on their separation and not on their absolute position, which applies to any pair of points (x_i) and (x_j) separated by $h = (x_i) - (x_j)$. In general terms, equation 2.12 is described as,

$$C(x_i, x_j) = E[\{Z(x_i) - \mu\} \{Z(x_j) - \mu\}]$$

which is constant for any distance h , known as lag. In other words, the covariance is a function of the lag only, and can be rewritten as,

$$\begin{aligned} cov[(Z(x), Z(x+h))] &= E[\{Z(x) - \mu\} \{Z(x+h) - \mu\}] \\ cov[(Z(x), Z(x+h))] &= E[\{Z(x)\} \{Z(x+h)\} - \mu^2] \\ cov[(Z(x), Z(x+h))] &= C(h). \end{aligned}$$

Considering that, whereas in general the mean might not be constant, it could be so for small h at least, so the expected differences would be zero,

$$E[Z(x) - Z(x + h)] = 0.$$

Therefore, replacing the covariance by the variance difference as measures of spatial relation, the variance is then expressed by equation 2.14,

$$\begin{aligned} \text{var}[(Z(x) - Z(x + h))] &= E[\{Z(x) - Z(x + h)\}^2] \\ \text{var}[(Z(x) - Z(x + h))] &= 2\gamma(h) \end{aligned} \quad (2.14)$$

where $\gamma(h)$ is known as the semi-variance at lag h . The term *semi* refers to the fact that it is half of the variance. It is; nevertheless, the variance per point when the points are considered in pairs.

As a function of h it is the semi-variogram, which is usually known as variogram only. The variogram is a function of a stochastic process, and can be classified in regional and experimental variogram. The regional variogram is the one of the particular realization in a finite region, while the experimental or sample variogram is computed from data which constitute a sample from that region. This variogram summarizes the spatial relations in the data. However, the goal is to obtain a variogram to describe the variance of the region, which is normally continuous. Thus, the observed values are used as approximations to the function to be fitted to the observations. Another reason for fitting a continuous function is to describe the spatial variation. But how closely should one attempt to follow the experimental variogram? The answer is just to fit the simplest function that makes sense.

The shape of the variogram is generally described by three parameters, sill, nugget and range, as shown in figure 2.14.

If $h = 0$, equation 2.14 shows that,

$$\begin{aligned} \text{var}[(Z(x) - Z(x + 0))] &= E[\{Z(x) - Z(x + 0)\}^2] \\ \text{var}[(Z(x) - Z(x + 0))] &= 0 \end{aligned}$$

but when other value than 0 is obtained, this discrepancy is known as the **nugget** variance. It means that the data themselves differ from their neighbours in irregular steps, large or small, rather than in smooth progression. In addition, the variogram may reach upper bounds in which they remain after having initially increased, if so, this maximum value is defined as **sill**, and the lag distance at which the sill is defined is called **range**. Once the parameters of the best fitting solution are achieved, the variance is obtained from equation 2.15

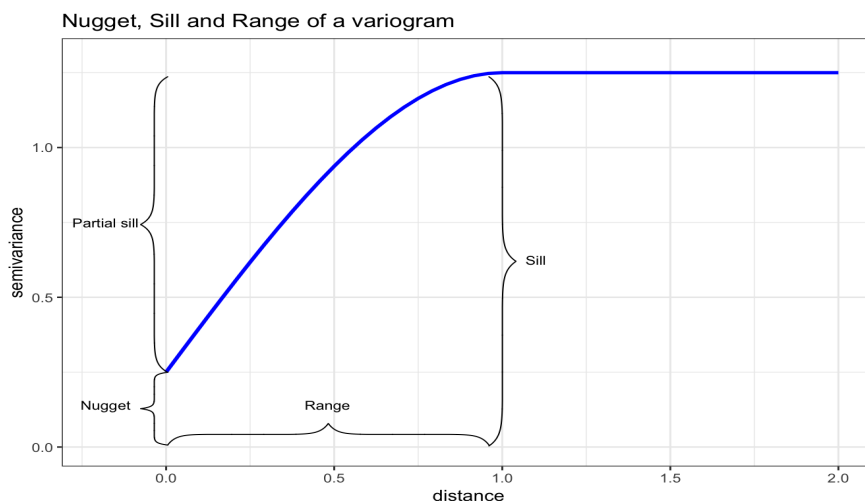


Figure 2.14: Variogram parameters [Hartmann et al., 2018]

$$\gamma(h) = \text{nugget} + \text{sill} \left\{ 1 - \exp\left(-\frac{h}{\text{range}}\right) \right\}. \quad (2.15)$$

Equation 2.15 allows the determination of the second part of a full variance-covariance matrix, while the last part of the full variance-covariance matrix can be obtained analytically [Simons and Rosen, 2015].

3 Methodology

This chapter aims to provide the defined methodology that has been generated for this case of study. The explanation starts with a description of the 3-dimensional decomposition, based on the LSA theory, followed by the detailed explanation of the criteria taken into account for the combinations of the radar and optical products sensed over the area of interest before and after the earthquake. This information will enable a complete assessment of the results and the possible improvements to be done.

3.1 Study Area

The region of interest for this study case is the Searles Valley, near the city of Ridgecrest, California. On 4 July 2019, a sequence of damaging earthquakes began near the city of Ridgecrest which included a foreshock with a moment magnitude (M_w) of 6.4 followed by a M_w 7.1 mainshock almost 34 hours later. These events were mainly felt in areas of California, Nevada, and Arizona, being Ridgecrest and Trona the most affected towns. These two events are part of a long-lived cluster historical earthquakes which started in 1872, including the 1992 M_w 7.3 Landers and 1999 M_w 7.1 Hector Mine ruptures [Milliner and Donnellan, 2020]. Space geodetic techniques indicate that since 1990, a right lateral shear reaches about 10 mm/yr [Chen et al., 2020]. An overview of the study area is shown in figure 3.1. The area surrounded by the yellow rectangle shows the region in which this study is focused.

3.2 3-Dimensional Decomposition

Earthquakes produce static displacement of the ground that can be observed near the fault which where slipped during the seismic rupture. Measurements of the displacements is a very important aspect, for example in seismotectonics, as it provides a better insight of the geometry of the fault and the energy released by the earthquake. Those measurements are generally performed based on field observations. However, the disadvantage is that the fault area is normally hard to access and not easy to be detected in the field. An alternative technique to

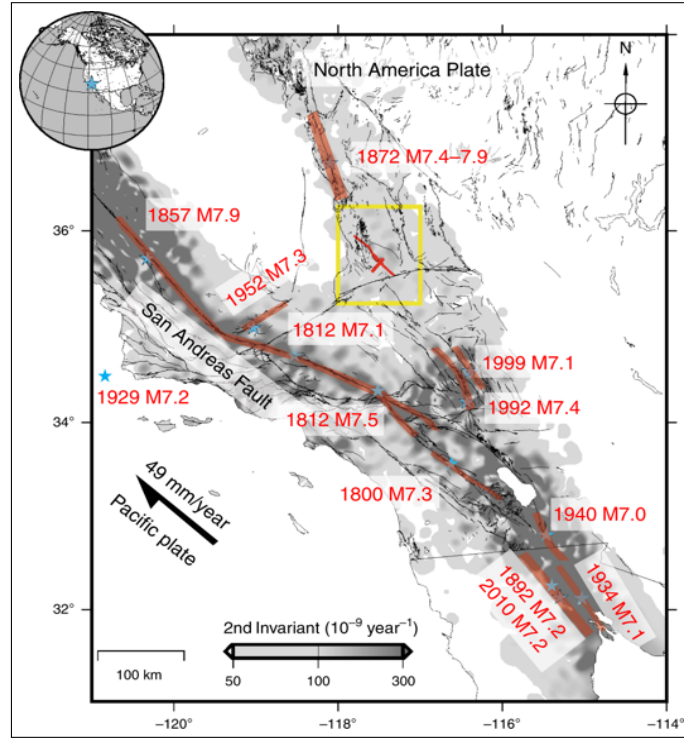


Figure 3.1: Area of study, Ridgecrest - California
[Chen et al., 2020]

obtain measurements is coming from Global Navigation Satellite Systems (GNSS) receivers. The drawback is that this technique has a sparse coverage over the affected area, in addition that the co-seismic ground displacement area is normally unknown a priori, so it is not possible to have measurements before the event, unless the receivers were already installed and were not damaged. Satellite images, when collected at regular intervals, can capture co-seismic displacements without advance knowledge of the earthquake's location. InSAR, first introduced in 1974 for topographic mapping, can also be used to detect changes in the ground surface. The Landers earthquake was the first earthquake that was imaged with InSAR. These studies were able to demonstrate the usefulness of satellite radar data for observing crustal deformation and they were the beginning of a number of spaceborne radar studies of crustal and ice deformation [Massonnet et al., 1993] [Van Puybroeck et al., 2000] [Jónsson et al., 2002] [Rosu et al., 2015].

Nevertheless, a very important aspect to be considered is that InSAR technique is not free of shortcomings. A significant limitation of InSAR technique is the inability of measuring in three dimensions, thus the radar instrument is capable of measuring only one-dimensional changes along the LOS. As explained in section 2.1.1.1, radar systems perform the observations based on a side looking geometry. This is the reason why deformation on the Earth are only sensed in the viewing direction, yet the actual deformation may have vertical and horizontal compo-

nents. In addition, due to satellite's flying direction, the measurements are much less sensitive in the along track direction. A solution to this problem is defined if other sets of interferograms can be made along other directions, then the surface motions may be recovered in their entirety by resolving the observations into their vector components [Gabriel et al., 1989].

The range displacement, along the LOS, is normally derived by conventional interferometric processing, while azimuth displacement is retrieved from offset tracking techniques or Multiaperture Interferometry (MAI) [Mehrabi et al., 2019]. For this case of study, the 3-dimensional displacement is computed not only from radar interferometric and offset tracking processing products, but also from sub-pixel cross correlation of optical observations. Even though each of these products are obtained from different observations systems and processed by different methodologies, they all provide information of the ground displacement; therefore, from now on, all these product are referred as **displacement maps**.

The radar data used in this project were obtained from Sentinel-1, while the optical images were captured by Sentinel-2 satellite. All the acquired products are freely available, and can be downloaded from the *ESA Copernicus Open Access Hub*.

3.2.1 Interferometry processing

InSAR has become a highly used technique for precise and detailed mapping of the Earth's surface deformation. Coherent radar echoes will be correlated with each other if each represents nearly the same interaction with a scatter or set of scatterers, which does not always happen. For example, in a water basin or densely vegetated area, the scatterers can totally change after a few milliseconds, whereas exposed rock or urban areas remain stable even after years [Zebker and Villasenor, 1992] [Bechor, 2006] [ESA, 2007]. In this study, it will be clearly shown that the lost of coherence is mainly evidenced from changes in damaged areas caused after an earthquake.

The three-dimensional displacement vector, with the East, North and Up component direction, is projected to the one range component in the LOS [Hanssen, 2001]. The linear equation describing the projection is mathematically expressed as equation 3.1,

$$d_r = d_U * \cos(\theta) - d_N * \cos(\alpha - \frac{3\pi}{2}) * \sin(\theta) - d_E * \sin(\alpha - \frac{3\pi}{2}) * \sin(\theta) \quad (3.1)$$

where α is the satellite's heading angle, θ corresponds to the incidence angle, and d_U , d_N and d_E represent the displacement in the Up, North and East component, respectively. Assuming that this linear equation is defined for the ascending and

descending images, the system of linear equation in matrix representation as show in 3.2.

$$\begin{bmatrix} d_{rAsc} \\ d_{rDes} \end{bmatrix} = \begin{bmatrix} \cos(\theta_a) & -\cos(\alpha_a - \frac{3\pi}{2})\sin(\theta_a) & -\sin(\alpha_a - \frac{3\pi}{2})\sin(\theta_a) \\ \cos(\theta_d) & -\cos(\alpha_d - \frac{3\pi}{2})\sin(\theta_d) & -\sin(\alpha_d - \frac{3\pi}{2})\sin(\theta_d) \end{bmatrix} \begin{bmatrix} d_U \\ d_N \\ d_E \end{bmatrix}. \quad (3.2)$$

The unknown parameters of the system of linear equations are d_U , d_N and d_E , meaning that at least three observations for each pixel where the 3-dimensional displacement is aimed to be obtained are needed. For this reason, the importance of combining the displacement computed from interferometric phase processing with products derived from other processing techniques, such as sub-pixel cross correlation, can lead to the optimal decomposition in three dimensions.

The displacement maps obtained after interferometric phase processing, detailed described in appendix A, are shown in figure 3.3, where the main faults are represented by the black continues lines, and the epicenter of the M_w 7.1 and M_w 6.4 are illustrated by the cyan and yellow star, respectively.

For this case, the observation data consist of two pairs of images, one ascending and one descending, sensed according to the information provided in table 3.1

Table 3.1: Sentinel-1 ascending and descending observations specifications

Specifications	Ascending track	Descending track
Master image date	28.06.2019	04.07.2019
Slave image date	10.07.2019	16.07.2019
Incidence angle	39.3974°	39.3157°
Heading angle	346.9272°	193.0393°

The left image at figure 3.2 shows the displacement obtained from phase observations in the ascending track, and the right image represents the displacement coming from the descending track. The red color in both displacement maps define the areas that subsidence is evidenced, while the blue colored areas denote uplift. It can be clearly seen that the areas showing uplift in the ascending observations show subsidence in the descending product. Due to the difference in the horizontal component of the LOS unit vectors, the pattern of the deformation is reversed between the ascending and descending interferograms [Decriem et al., 2010]. In addition, both displacement maps do also show gaps close to the faults. This areas illustrate the regions that where highly affected by the earthquake, which means that the properties of the scatterers change abruptly from first to the second acquisition, leading to a loss of coherence, which is always expected to be stronger close the faults, and attenuated as the distance to the fault increases.

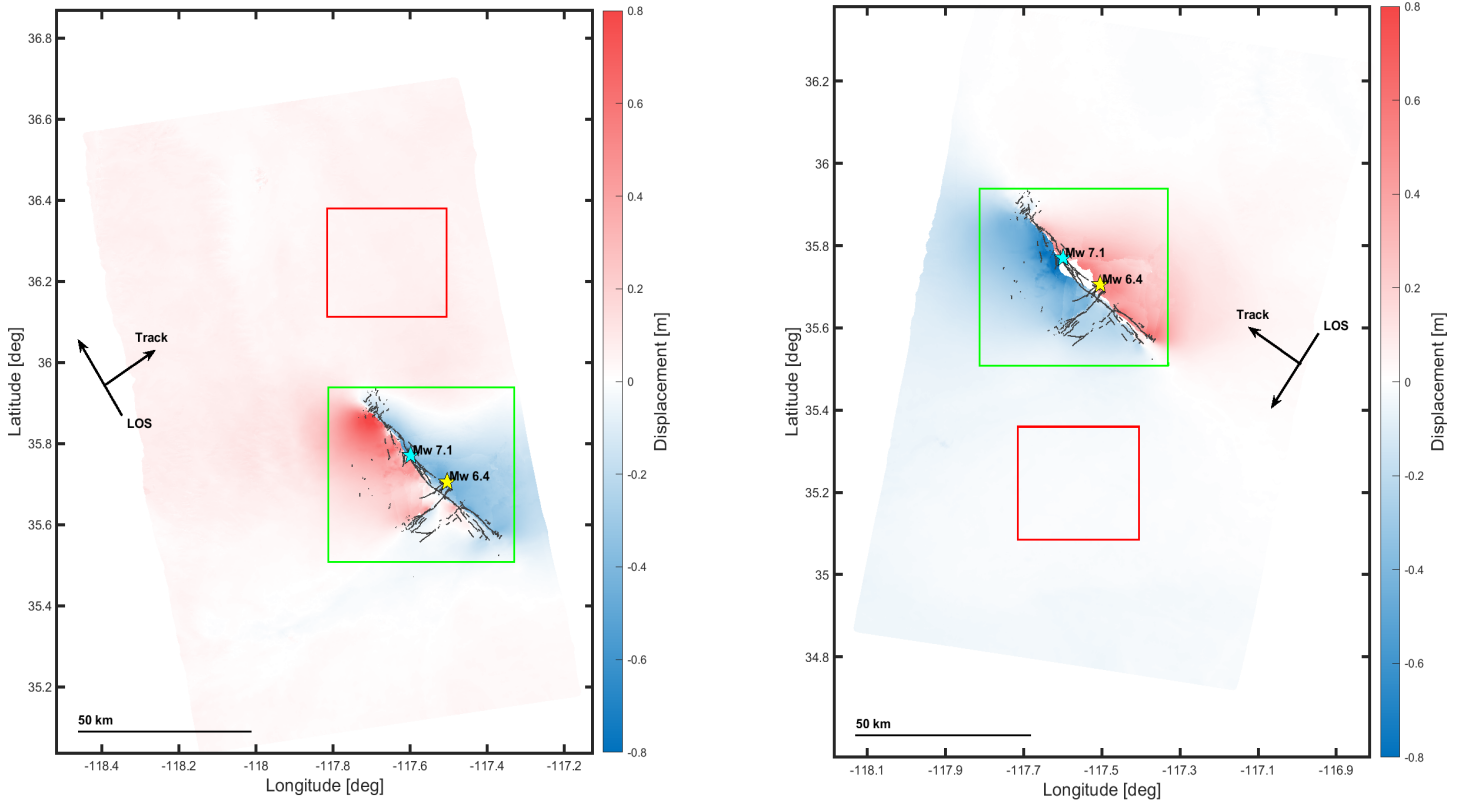


Figure 3.2: Displacement maps in the ascending track (left) and descending track (right) obtained from phase interferometry processing. Areas inside the green box represent the near field and the areas within the red box correspond to the far field. Faults and earthquake epicenters data courtesy of USGS

Finally, for this study purposes, the area of the displacement map inside the green square has been tagged as the **near field** (closer view shown in figure 3.3) and the region within the red square has been labelled as **far field**. The results of the displacement in the near field for both, the ascending and descending tracks, shows a magnitude between -0.8 and 0.8 meters of movement along the LOS, or in the range direction. These results coincides with the 3-dimensional displacement computed in previous studies (see [Fielding et al., 2019] and [Xu et al., 2019]).

3.2.2 Offset Tracking processing

Considering that offset between image pixels are partly originated from ground displacement; for example, from earthquakes, it has been proved that the magnitude of this type of offset is characterized by gradients typically lower than 0.1%, except within a few tens of meters of faults, which are generally smaller than the pixel size. Offsets may be determined from a broad range of techniques, but correlation methods using sliding windows have been proved to be efficient to measure such offsets [Massonnet et al., 1993] [Van Puymbroeck et al., 2000].

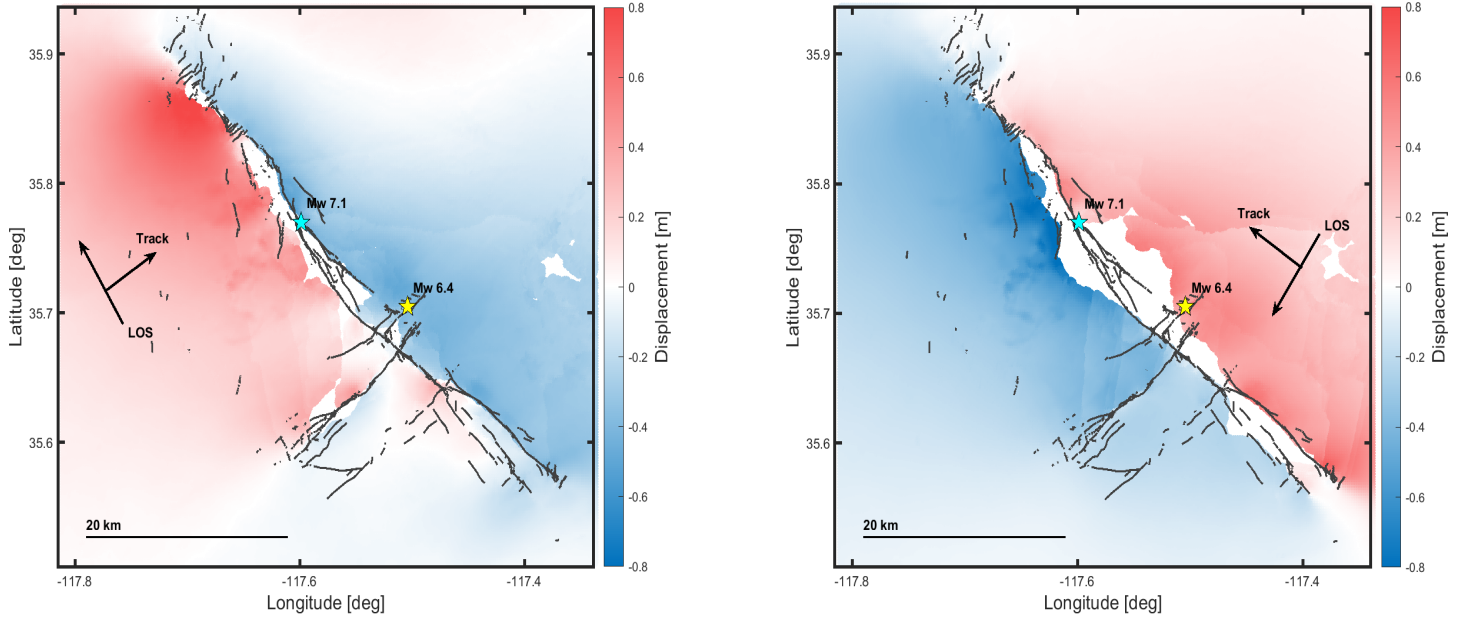


Figure 3.3: Closer view of near field displacement maps in the ascending track (left) and descending track (right). Faults and earthquake epicenters data courtesy of USGS

[Rosu et al., 2015] agree that image correlation is one of the most efficient techniques to determine horizontal ground displacements due to earthquakes, landslides, ice flows or sand dune migrations, and by using sub-pixel correlation on before and after event images, it is possible to compute the displacement field. For this reason, offset tracking processing of radar and optical images captured before and after the Ridgecrest earthquakes, is developed by means of cross correlation method.

The main idea of cross correlation is to assess the similarity between two images by setting one of them as the reference which is compared to the remaining one. The comparison is developed by first defining a window from the non-reference image that will slide all over the reference image. So, given the reference image $g_1(i,j)$ and the non-reference image or template $g_2(p,q)$, the idea is to find the offset $[\hat{u},\hat{v}]$ between g_1 and g_2 , as shown in figure 3.4.

The ideal case when finding the offsets is to reach $[\hat{u},\hat{v}]$ that maximizes the similarities of the corresponding intensity values. To do so, the best estimate of the offset $[\hat{u},\hat{v}]$ is given by maximizing the cross correlation coefficients over all possible locations, expressed as equation 3.3,

$$[\hat{u},\hat{v}] = \underset{u,v}{\operatorname{argmax}} \rho_{12}(u,v) \quad (3.3)$$

with,

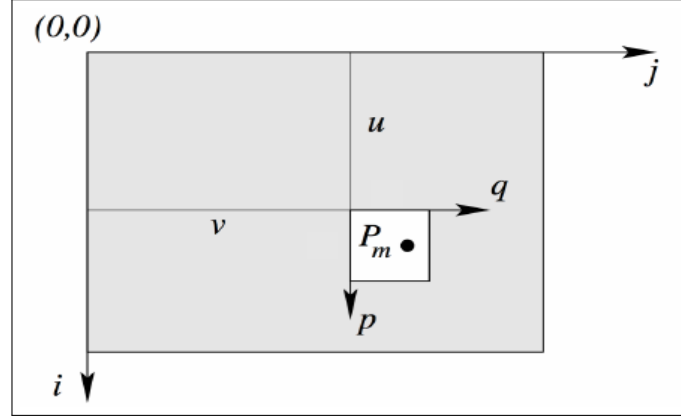


Figure 3.4: Cross correlation principle
[Stachniss, 2015]

$$\rho_{12}(u,v) = \frac{\sigma_{g_1 g_2}(u,v)}{\sigma_{g_1}(u,v)\sigma_{g_2}} \quad (3.4)$$

where $\sigma_{g_1 g_2}(u,v)$ represents the covariance between intensity values of g_1 and g_2 inside the window area at position $[u,v]$, σ_{g_1} is the standard deviation of intensity values of the query image g_1 within the window g_2 , and σ_{g_2} is the standard deviation of the intensity values defined in window g_2 [Stachniss, 2015].

3.2.2.1 Radar observations offset tracking

The principal interest of applying offset tracking is to map displacements along the range and azimuth direction [Wegnüller et al., 2016]. The displacement obtained in the range direction is defined by,

$$d_r = d_U * \cos(\theta) - d_N * \cos(\alpha - \frac{3\pi}{2}) * \sin(\theta) - d_E * \sin(\alpha - \frac{3\pi}{2}) * \sin(\theta) \quad (3.5)$$

which is exactly the same as equation 3.1, that was defined for describing the displacement along the range direction from interferometric phase processing. On the other hand, the displacement in the azimuth direction is represented by the linear equation 3.6

$$d_a = d_N * \sin(\alpha - \frac{3\pi}{2}) - d_E * \cos(\alpha - \frac{3\pi}{2}). \quad (3.6)$$

Again, assuming that observations for the ascending and the descending track are available, the matrix representation of equation 3.6 is defined by expression 3.7

$$\begin{bmatrix} d_{aAsc} \\ d_{aDes} \end{bmatrix} = \begin{bmatrix} \sin(\alpha_a - \frac{3\pi}{2}) & -\cos(\alpha_a - \frac{3\pi}{2}) \\ \sin(\alpha_d - \frac{3\pi}{2}) & -\cos(\alpha_d - \frac{3\pi}{2}) \end{bmatrix} \begin{bmatrix} d_N \\ d_E \end{bmatrix}. \quad (3.7)$$

The most visible difference between equation 3.5 and 3.6 is that the latest one do not show any Up component, nor any influence coming from the incidence angle. The observation in the azimuth direction is performed along the satellite's flight direction, which means that the incidence angle is represented by a 90° angle so that there is no sensitivity to the vertical movement.

The cross correlation processing for this study was initially produced from amplitude data using the software SNAP [ESA, 2020b] and level-1 Ground Range Detected (GRD) Sentinel-1 products, detailed explained in appendix B. As explained in section 2.2, GRD products consist of focused data which is detected, multilooked and projected to the ground range using WGS84 ellipsoid model. Ground range coordinates are the slant range coordinates projected into the ellipsoid. Pixel values represent detected amplitude only because phase information is lost. The main difference between SLC and GRD products is that SLC products preserve phase information and are processed at the natural pixel spacing, while GRD product contain the detected amplitude and are multilooked to reduce the impact of speckle [ESA, 2019b]. The results from applying cross correlation to GRD ascending and descending products are shown in figure 3.5,

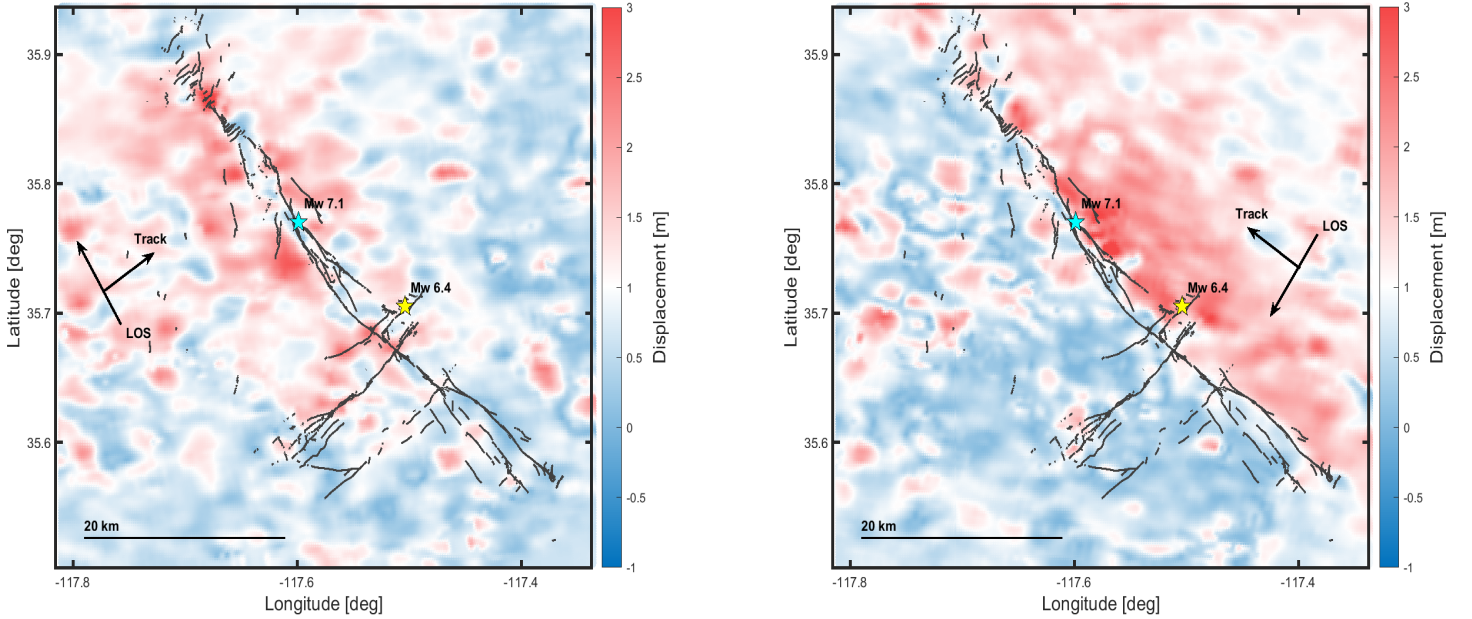


Figure 3.5: Displacement maps in the ascending track (left) and descending track (right) obtained from amplitude offset tracking processing. Faults and earthquake epicenters data courtesy of USGS

From either, ascending and descending, tracks, the results are very noisy in comparison with the smooth displacement maps shown in figure 3.3. For this reason,

the offset tracking processing was afterwards performed on phase data from SLC products, using the commercial software GAMMA [GAMMA, 2017]. GAMMA software estimates the range and azimuth registration offset fields using cross correlation optimization of the detected SLC data [GAMMA, 2019]. The processing steps for offset tracking computation are shown in figure 3.6.

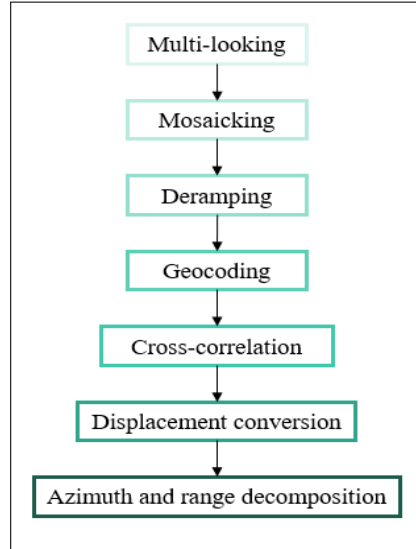


Figure 3.6: GAMMA software offset tracking processing steps

The displacement maps resulted from offset tracking processing by cross correlation of phase data in the range and azimuth direction, are shown in figure 3.7 and figure 3.8, respectively.

Comparing these two last displacements maps obtained from SLC (phase) offset tracking, with the results from amplitude, derived from GRD (amplitude) products, it is easy to realize the great spatial resolution improvement of applying offset tracking in phase rather than in amplitude observations.

According to [Wener et al., 2005], the accuracy of offset tracking is dependent on the accuracy of pixel-by-pixel co-registration and the spatial resolution of the SAR images, rather than on the accuracy of phase measurements like in the case of differential InSAR. The accuracy of offset tracking is therefore much lower than that of differential InSAR. This is the reason why the smoother and less noisier displacement maps so far obtained come from interferometric processing along the range direction. However, the importance of the displacement maps obtained from offset tracking processing is that the azimuth direction displacement can only be retrieved from this offset tracking and not from interferometric processing. In addition, both, range and azimuth direction displacement maps obtained from offset tracking are also a very important source of information near the fault trace, where interferometric processing displacement maps suffer from decorrelation, leading to a loss of information.

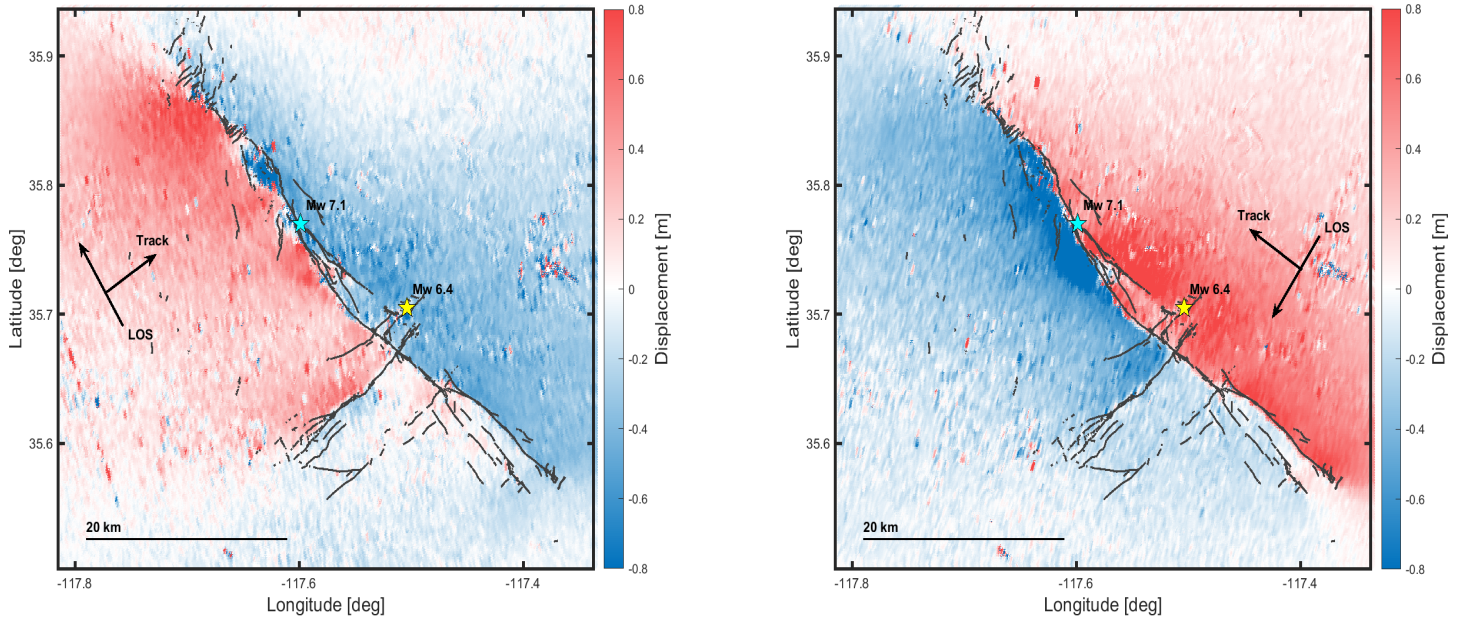


Figure 3.7: Displacement maps in the ascending track (left) and descending track (right) obtained from phase offset tracking processing along the range direction. Faults and earthquake epicenters data courtesy of USGS

Finally, analyzing the displacement maps obtained from offset tracking processing only, the results also clearly demonstrate the higher resolution that the observations along the range direction have over the ones derived in the azimuth direction. The magnitude of the displacement in the range direction from offset tracking processing is compatible with the displacement obtained from interferometric processing, which varies between -0.8 and 0.8 m, while the magnitude of displacement in the azimuth direction varies from -1.5 to 1.5 m.

3.2.2.2 Optical observations offset tracking

Optical imagery of the ground has been increasing along the time, as well as its resolutions. When analyzing the cross correlation technique applied on optical observations, offset between them can be found depending on the distance between the orbits, the viewing angles, effect of the topography, attitude of the platform, geometry detectors, and displacement on the ground. To successfully measure the ground displacement, a compensation for the offsets coming from the other mentioned effects need to be applied, which has been already explored by [Van Puymbroeck et al., 2000].

As explained in section 2.2.2, the highest resolution in Sentinel-2 images is found in data sensed from band 2,3,4 and 8, with 10 m spatial resolution each. For this reason, the input optical data captured before and after the earthquake was chosen to be from band 4. Offset tracking processing for optical data was performed with

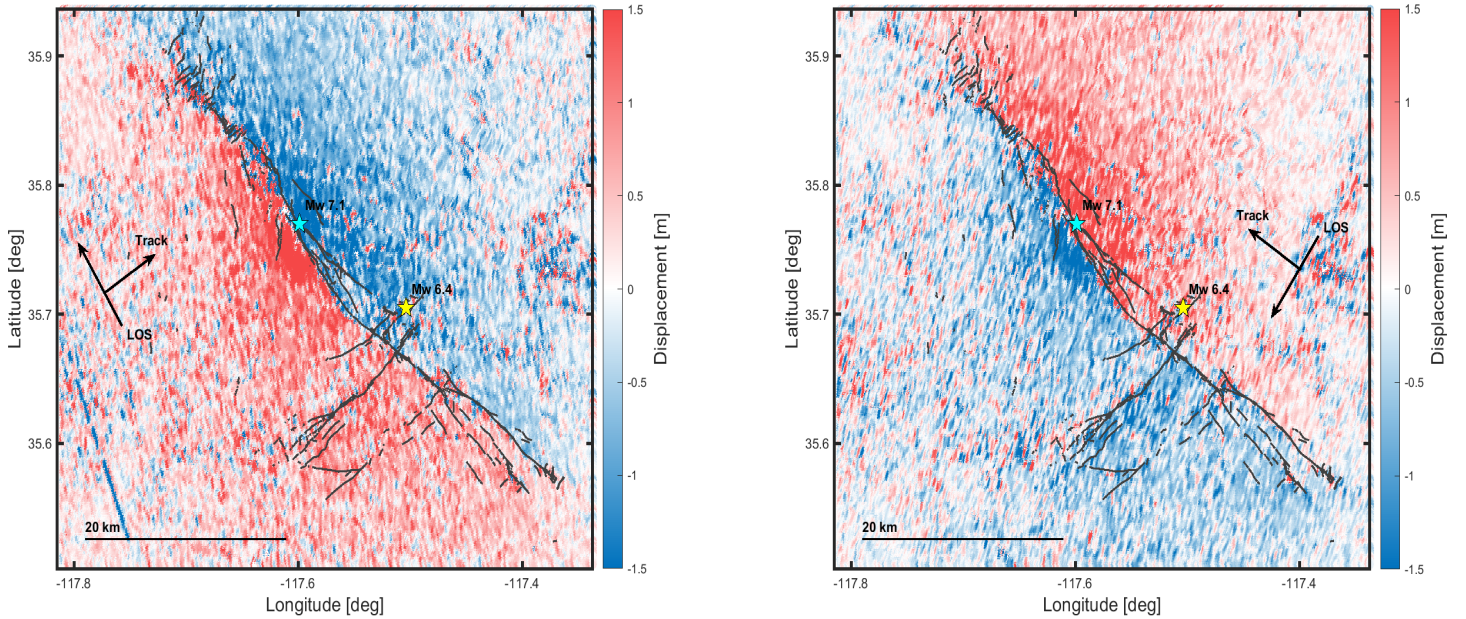


Figure 3.8: Displacement maps in the ascending track (left) and descending track (right) obtained from phase offset tracking processing along the azimuth direction. Faults and earthquake epicenters data courtesy of USGS

two free software, COSI-Corr [COSI-Corr, 2004] and MicMac [MicMac, 2018]. The processing steps for each software is detailed explained in appendix C and D, respectively.

The main idea in either case is to estimate the offset tracking based on cross correlation approach. In this case, the results obtained with these two different software show very similar patterns and magnitudes of displacement for the North-South (NS) and the East-West (EW) directions. The displacement maps obtained using COSI-Corr are shown in figure 3.9, while figure 3.10 shows the displacement maps resulted from MicMac.

The most visible pattern in both, COSI-Corr and MicMac displacement maps is the stripping effect. According to [Milliner and Donnellan, 2020], the stripping artifacts result from jitter of the spacecraft during the push-broom type acquisition of the images, but also from misalignment in the charge-coupled-device (CCD), which is an array that collects 13 bands imagery at 786 km altitude, at different resolutions. In order to confirm this spacecraft effect on the images, cross correlation was also computed using the Automated and Robust Open-Source Image Co-Registration Software (AROSICS), a free and open source Python package that performs automatic sub-pixel co-registration of two satellite images datasets based on image matching approach working in the frequency domain [Scheffler et al., 2017]. The results of this last test also show very evident stripping effect. Finally, the obtained results were also compared with the displacement maps computed for the same earthquake using Sentinel-2 images, band 4 and processed

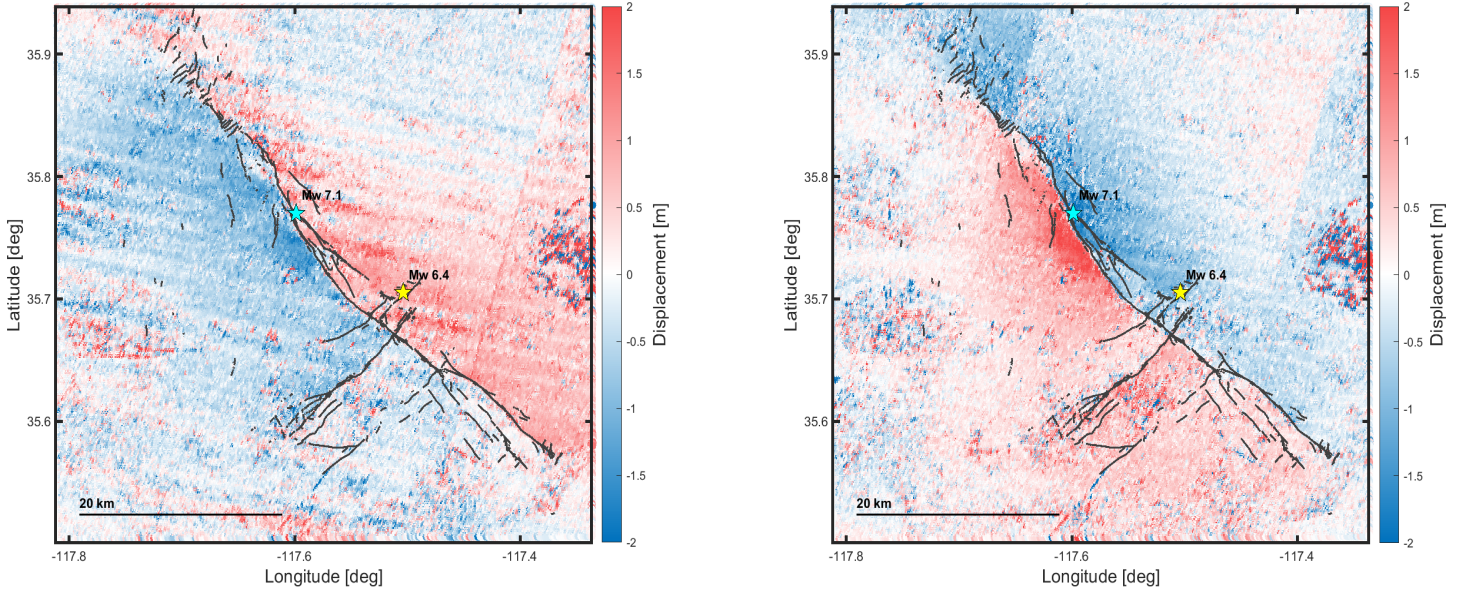


Figure 3.9: Displacement maps in the EW direction (left) and NS direction (right) obtained from phase offset tracking processing using COSI-Corr software. Faults and earthquake epicenters data courtesy of USGS

using also COSI-Corr and MicMac software (see [Valkaniotis, 2019] and [Aati and Avouac, 2019]), and the magnitudes and pattern of the displacement are showing relevant agreement with the obtained in this study.

The equation that describes the displacement observed by optical images is represented by equation 3.8,

$$d = d_N * \sin\left(\alpha - \frac{3\pi}{2}\right) - d_E * \cos\left(\alpha - \frac{3\pi}{2}\right) \quad (3.8)$$

which in this case, is expressed by the exactly equation 3.6, defined for the displacement along the azimuth direction for observations obtained from Sentinel-1 sensor. This means that the observing geometry of Sentinel-2 and Sentinel-1 satellite is the same whenever the along-track direction only is considered. However, the heading angle for the Sentinel-2 satellite is either 90° ($\pi/2$) when observing in the East direction, and 0° for the North direction observations. Therefore, replacing this angular values in equation 3.8, it observation equation is then expressed by 3.9,

$$\begin{aligned} \begin{bmatrix} d_{EW} \\ d_{NS} \end{bmatrix} &= \begin{bmatrix} \sin\left(\frac{\pi}{2} - \frac{3\pi}{2}\right) & -\cos\left(\frac{\pi}{2} - \frac{3\pi}{2}\right) \\ \sin\left(0 - \frac{3\pi}{2}\right) & -\cos\left(0 - \frac{3\pi}{2}\right) \end{bmatrix} \begin{bmatrix} d_E \\ d_N \end{bmatrix} \\ &= \begin{bmatrix} 0 & 1 \\ 1 & 0 \end{bmatrix} \begin{bmatrix} d_E \\ d_N \end{bmatrix}. \end{aligned} \quad (3.9)$$

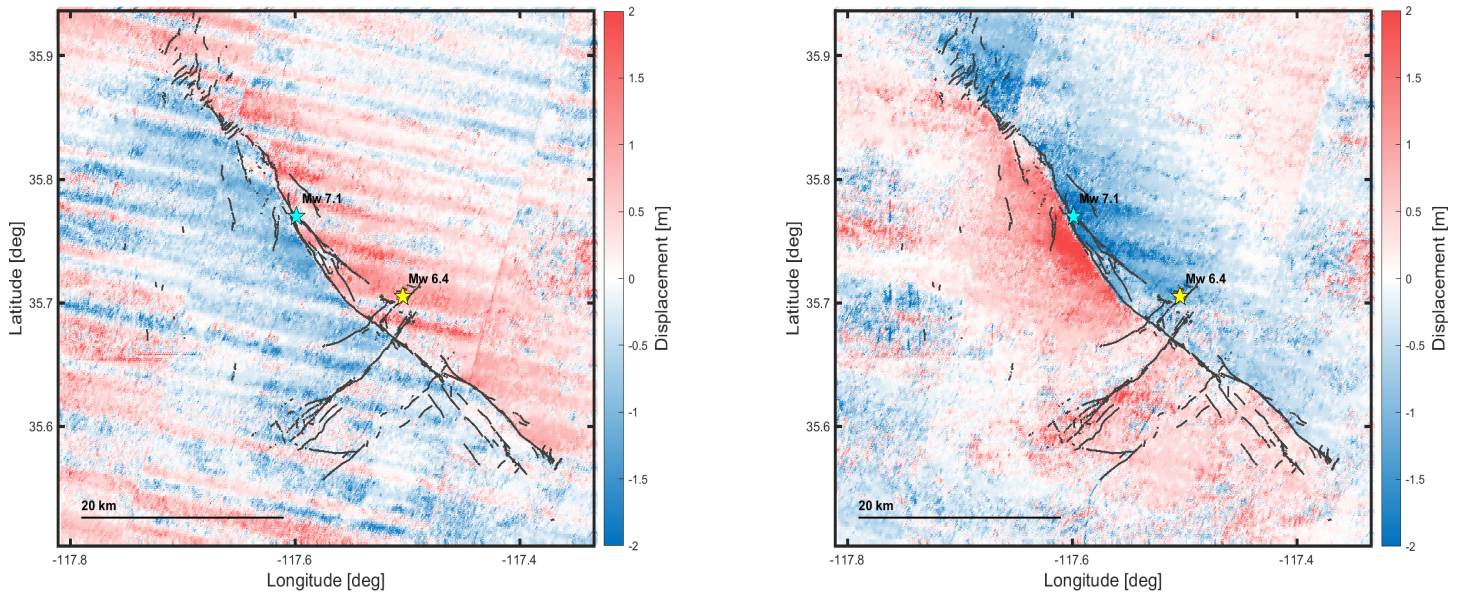


Figure 3.10: Displacement maps EW direction (left) and NS direction (right) obtained from phase offset tracking processing using MicMac software. Faults and earthquake epicenters data courtesy of USGS

Comparing the obtained displacement maps after applying cross correlation method using COSI-Corr and MicMac software, it is possible to identify that both results also agree in magnitude and in the direction of the displacement. The red colors in figures 3.9 and 3.10 represent movement along the East direction for the left side maps, and along the North direction in the right side maps, while the blue colors are assigned for the displacement in the corresponding opposite direction for each map. The magnitudes of the ground displacement in NS and EW direction reach up to -2 to 2 m.

3.3 Radar and Optical Observations Combination

One of the limitations of computing the 3-dimensional displacement from interferometric phase is, as explained before, the impossibility of retrieving 3-dimensional displacement. Having only one observation retrieved from the ascending and one from the descending track, there is one component that could never be possible to be estimated. The solution to overcome this shortcoming is to combine more interferometric displacement maps, or other sources of observations obtained over the same affected region. In this study, the aim of achieving the displacement in the East, North and Up component is derived from the combination of the radar and optical observations.

From the displacement results obtained after interferometric processing (section 3.2.1) and radar and optical data offset tracking processing (section 3.2.2), more than one combination between the obtained displacement maps is possible. In this study, the following three combinations were defined.

- **Combination 1.** This combination is achieved from ascending and descending Sentinel-1 products. The displacement maps obtained by interferometric processing applied to observations in the range direction (see figure 3.3) with the displacement maps in the range and azimuth direction derived from offset tracking processing (see figure 3.7 and 3.8) are the only input products taken into account in this case.
- **Combination 2.** This combination considers the same displacement maps from the previous combination, but additionally including Sentinel-2 displacement maps in the EW and NS directions, obtained by offset tracking processing.
- **Combination 3.** This last combination is based in the second combination, but without including Sentinel-1 offset tracking displacement maps in both, range and azimuth, directions. This means that only displacement maps from interferometric processing of Sentinel-1 and offset tracking of Sentinel-2 data are part of the combination.

For all these three combination cases, the estimation of the 3-dimensional displacement is performed applying LSA. Therefore, in addition to the three combinations previously defined, the LSA for all of the combinations was performed for three different weighting cases.

- **Case a.** No weighting is applied for the decomposition of the displacement in the East, North and Up component. The weight matrix is represented by the identity matrix.
- **Case b.** Weights are obtained from the standard deviation of all the pixels inside the far field window for each of the products independently. The inverse of the standard deviation is set to be weight for every pixel contained in each of the products. This case satisfies the first part that defines a full variance-covariance matrix, explained in section 2.3.2.
- **Case c.** Weights are obtained after performing a semi-variogram model fitting. A full variance-covariance matrix is assigned for each of the products separately, which means not only that each pixel has its own weight, but also that the relative weights between pixels are assigned in the off-diagonal. In this case, the weighting matrix fulfills the first and second part of the full variance-covariance matrix.

Having defined three products combination and three weighting cases for each combinations, 9 solutions for the 3-dimensional decomposition will be obtained. Figure 3.11 shows the scheme of the applied situations.

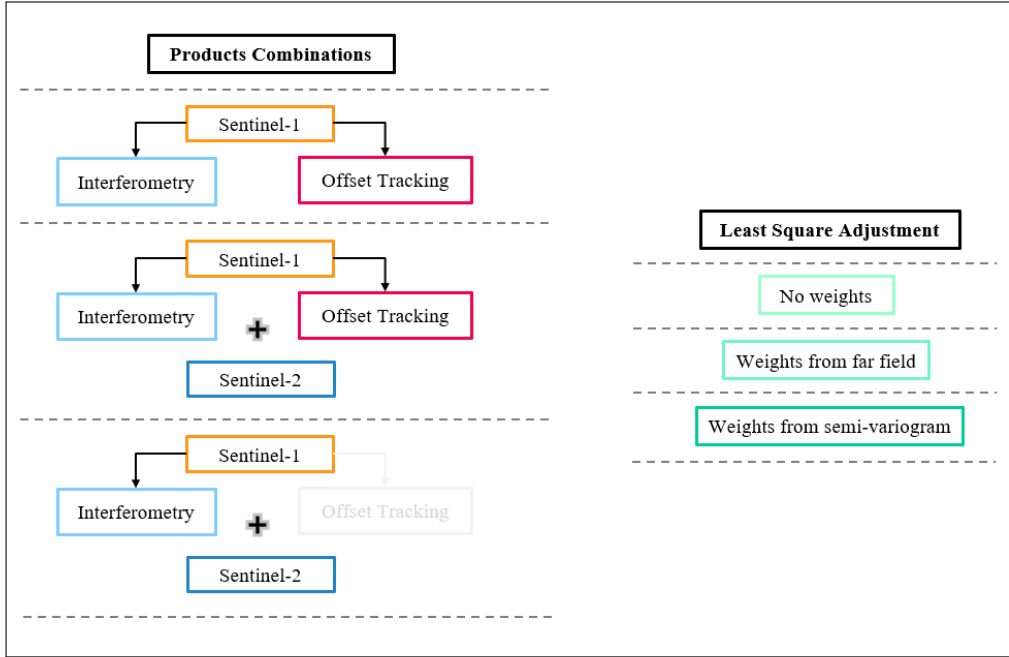


Figure 3.11: Products combination and LSA applied cases scheme

3.3.1 Functional Models

The functional model that describes each case varies according to their specific characteristics. The first combination is defined by equations 3.1 for the displacement maps in the range direction coming after interferometric processing, and by equations 3.5 and 3.6 describing the range and azimuth direction displacements resulted offset tracking processing, respectively. In matrix representation, the first functional model is defined by expression 3.10

$$\begin{bmatrix} d_{rAsc(I)} \\ d_{rDes(I)} \\ d_{aAsc(OT)} \\ d_{aDes(OT)} \\ d_{rAsc(OT)} \\ d_{rDes(OT)} \end{bmatrix} = \begin{bmatrix} \cos(\theta_a) & -\cos(\alpha_a - \frac{3\pi}{2})\sin(\theta_a) & -\sin(\alpha_a - \frac{3\pi}{2})\sin(\theta_a) \\ \cos(\theta_d) & -\cos(\alpha_d - \frac{3\pi}{2})\sin(\theta_d) & -\sin(\alpha_d - \frac{3\pi}{2})\sin(\theta_d) \\ 0 & \sin(\alpha_a - \frac{3\pi}{2}) & -\cos(\alpha_a - \frac{3\pi}{2}) \\ 0 & \sin(\alpha_d - \frac{3\pi}{2}) & -\cos(\alpha_d - \frac{3\pi}{2}) \\ \cos(\theta_a) & -\cos(\alpha_a - \frac{3\pi}{2})\sin(\theta_a) & -\sin(\alpha_a - \frac{3\pi}{2})\sin(\theta_a) \\ \cos(\theta_d) & -\cos(\alpha_d - \frac{3\pi}{2})\sin(\theta_d) & -\sin(\alpha_d - \frac{3\pi}{2})\sin(\theta_d) \end{bmatrix} \begin{bmatrix} d_U \\ d_N \\ d_E \end{bmatrix}. \quad (3.10)$$

The subscript a and r represent the azimuth and range direction, respectively. The ascending track is represented by the subscript Asc , likewise, Des for the descending track. The interferometric processing method is assigned by I , and OT for the

offset tracking processing method. This nomenclature intends to avoid possible confusions, as the equations defining the displacement along the range direction is the same for the interferometric and offset tracking processing methods.

For the second combination, the functional model is exactly the same as expression 3.10, but adding the observation equations that define the displacement coming in the NS and EW direction obtained after processing optical measurements, as shown in expression 3.11

$$\begin{bmatrix} d_{rAsc(I)} \\ d_{rDes(I)} \\ d_{aAsc(OT)} \\ d_{aDes(OT)} \\ d_{rAsc(OT)} \\ d_{rDes(OT)} \\ d_{EW} \\ d_{NS} \end{bmatrix} = \begin{bmatrix} \cos(\theta_a) & -\cos(\alpha_a - \frac{3\pi}{2})\sin(\theta_a) & -\sin(\alpha_a - \frac{3\pi}{2})\sin(\theta_a) \\ \cos(\theta_d) & -\cos(\alpha_d - \frac{3\pi}{2})\sin(\theta_d) & -\sin(\alpha_d - \frac{3\pi}{2})\sin(\theta_d) \\ 0 & \sin(\alpha_a - \frac{3\pi}{2}) & -\cos(\alpha_a - \frac{3\pi}{2}) \\ 0 & \sin(\alpha_d - \frac{3\pi}{2}) & -\cos(\alpha_d - \frac{3\pi}{2}) \\ \cos(\theta_a) & -\cos(\alpha_a - \frac{3\pi}{2})\sin(\theta_a) & -\sin(\alpha_a - \frac{3\pi}{2})\sin(\theta_a) \\ \cos(\theta_d) & -\cos(\alpha_d - \frac{3\pi}{2})\sin(\theta_d) & -\sin(\alpha_d - \frac{3\pi}{2})\sin(\theta_d) \\ 0 & 0 & 1 \\ 0 & 1 & 0 \end{bmatrix} \begin{bmatrix} d_U \\ d_N \\ d_E \end{bmatrix}. \quad (3.11)$$

Finally, the functional model for the third combination is obtained from the previous model, but removing the observation equation given for offset tracking processing applied in the range and azimuth from Sentinel-1 observations. This last model is expressed as shown in 3.12

$$\begin{bmatrix} d_{rAsc(I)} \\ d_{rDes(I)} \\ d_{EW} \\ d_{NS} \end{bmatrix} = \begin{bmatrix} \cos(\theta_a) & -\cos(\alpha_a - \frac{3\pi}{2})\sin(\theta_a) & -\sin(\alpha_a - \frac{3\pi}{2})\sin(\theta_a) \\ \cos(\theta_d) & -\cos(\alpha_d - \frac{3\pi}{2})\sin(\theta_d) & -\sin(\alpha_d - \frac{3\pi}{2})\sin(\theta_d) \\ 0 & 0 & 1 \\ 0 & 1 & 0 \end{bmatrix} \begin{bmatrix} d_U \\ d_N \\ d_E \end{bmatrix}. \quad (3.12)$$

The estimation of the 3-dimensional displacement based on these three combinations is then obtained based on the LSA method, expression 2.10, but for the three weighting cases considered in this study.

3.3.2 Stochastic Models

3.3.2.1 Case a. No weighting matrix (identity matrix)

For the first adjustment case, the weighting matrix is described by the identity matrix. It is represented by a diagonal matrix with $n \times n$ dimension, being n is the number of observations for each pixel. The weighting matrices for each of the three combinations are expressed as,

$$P_{a_1} = \begin{bmatrix} 1 & 0 & 0 & 0 & 0 & 0 \\ 0 & 1 & 0 & 0 & 0 & 0 \\ 0 & 0 & 1 & 0 & 0 & 0 \\ 0 & 0 & 0 & 1 & 0 & 0 \\ 0 & 0 & 0 & 0 & 1 & 0 \\ 0 & 0 & 0 & 0 & 0 & 1 \end{bmatrix} \quad P_{a_2} = \begin{bmatrix} 1 & 0 & 0 & 0 & 0 & 0 & 0 & 0 \\ 0 & 1 & 0 & 0 & 0 & 0 & 0 & 0 \\ 0 & 0 & 1 & 0 & 0 & 0 & 0 & 0 \\ 0 & 0 & 0 & 1 & 0 & 0 & 0 & 0 \\ 0 & 0 & 0 & 0 & 1 & 0 & 0 & 0 \\ 0 & 0 & 0 & 0 & 0 & 1 & 0 & 0 \\ 0 & 0 & 0 & 0 & 0 & 0 & 1 & 0 \\ 0 & 0 & 0 & 0 & 0 & 0 & 0 & 1 \end{bmatrix} \quad P_{a_3} = \begin{bmatrix} 1 & 0 & 0 & 0 \\ 0 & 1 & 0 & 0 \\ 0 & 0 & 1 & 0 \\ 0 & 0 & 0 & 1 \end{bmatrix}$$

with P_{a_1} , P_{a_2} and P_{a_3} being the weighting matrices for expression 3.10, 3.11 and 3.12, respectively.

3.3.2.2 Case b. Weighting matrix obtained from far field observations

In the second adjustment case, the weighing matrices are defined again by a diagonal matrix. The difference is that, in this case, the diagonal elements are no longer assumed to be 1, but expressed by,

$$1/\sigma$$

where σ represents the standard deviation of the observations allocated in the far field. One can rely on estimating the weights of the observations coming from the far field because the pixels inside this region are presumed to contain minimal tectonic deformation, implying that the error is stationary and the structure of the chosen area is representative of the rest of the deformation measurements [Milliner and Donnellan, 2020].

As each displacement map provide different magnitudes, so does the standard deviation. The weighting matrix that belongs to the expression 3.10 is defined by,

$$P_{b_1} = \begin{bmatrix} \frac{1}{0.0086} & 0 & 0 & 0 & 0 & 0 \\ 0 & \frac{1}{0.0043} & 0 & 0 & 0 & 0 \\ 0 & 0 & \frac{1}{0.2609} & 0 & 0 & 0 \\ 0 & 0 & 0 & \frac{1}{0.2420} & 0 & 0 \\ 0 & 0 & 0 & 0 & \frac{1}{0.0469} & 0 \\ 0 & 0 & 0 & 0 & 0 & \frac{1}{0.0468} \end{bmatrix}$$

$$P_{b_1} = \begin{bmatrix} 116.16 & 0 & 0 & 0 & 0 & 0 \\ 0 & 231.74 & 0 & 0 & 0 & 0 \\ 0 & 0 & 3.83 & 0 & 0 & 0 \\ 0 & 0 & 0 & 4.13 & 0 & 0 \\ 0 & 0 & 0 & 0 & 21.31 & 0 \\ 0 & 0 & 0 & 0 & 0 & 21.36 \end{bmatrix}$$

with the highest weight corresponding to the displacement obtained by interferometric processing in the ascending and descending track, followed by the last two values, which belong to the weight for the displacement in the range direction computed by offset tracking processing in the ascending and descending track. On the other hand, the lowest weights are found in the third and fourth column and row of the matrix, corresponding to the azimuth direction displacement after offset tracking processing for the observations sensed in the ascending and descending track. This situation was already expected because, as shown in table 2.2, the observations along the range direction achieve a spatial resolution of around 3 m, while for the azimuth direction its corresponding resolution is 22 m.

A curious situation from this last weighting matrix is that the magnitude of the weight corresponding to the displacement in the ascending track obtained from interferometric processing is 116.16 m^{-1} , which represents almost half of the weight for the displacement computed from observations of the descending track, corresponding to 231.74 m^{-1} . The near and far field for the displacement maps obtained after interferometric processing were already shown in figure 3.2. A closer view of the far field regions are represented in figure 3.12. The displacements from the left map, corresponding to ascending track observations, vary around 3 to 10 cm, while the displacement values of the right map, obtained from descending track observations, are between -3 to -1 cm. The distribution of the displacement values in these two far field areas can be better visualize in their corresponding histograms shown in figure 3.13.

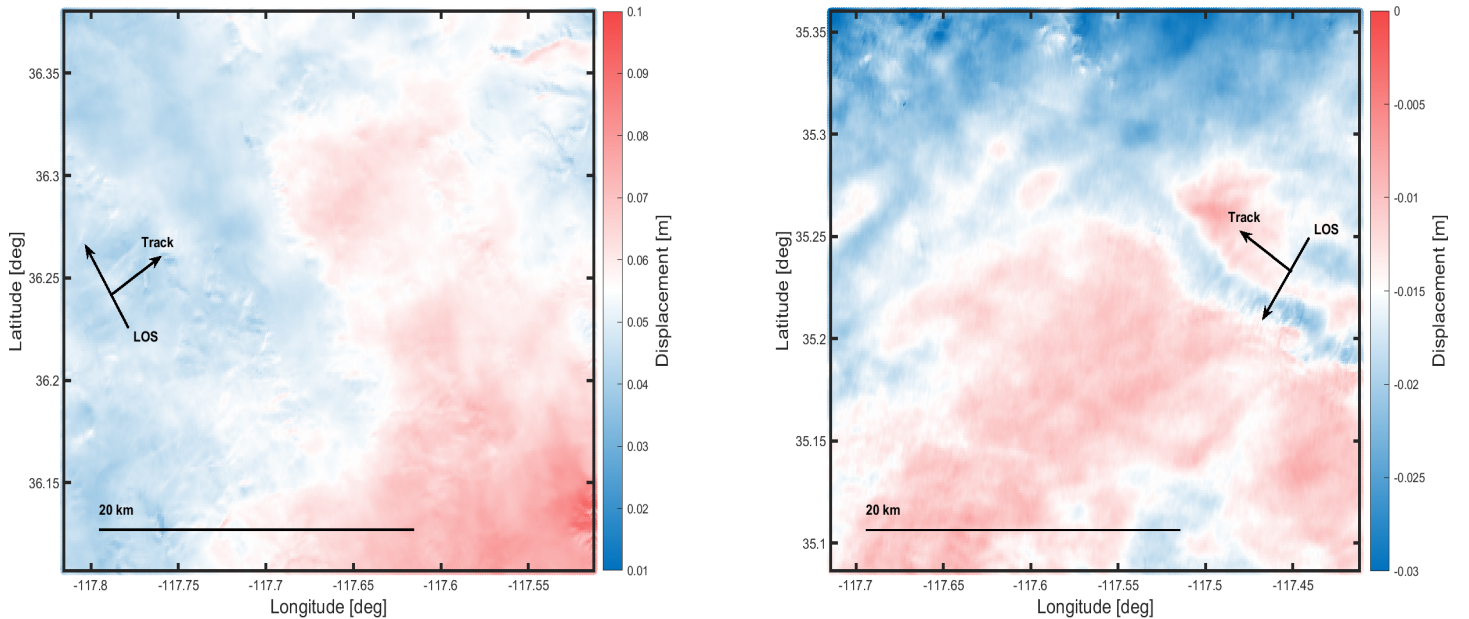


Figure 3.12: Closer view of far field displacement maps in the ascending track (left) and descending track (right) obtained from phase interferometry processing

From figure 3.13, it is possible to clearly evidence the wider distribution of the dis-

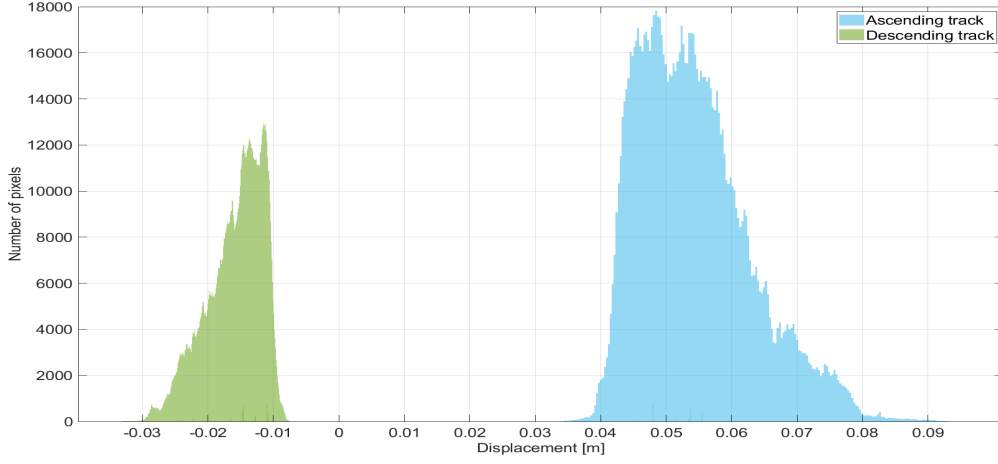


Figure 3.13: Histograms of far field displacement maps obtained from phase interferometry processing

placement values corresponding to ascending track in comparison to the narrower distribution of the values which describe the displacement in the far field for the descending track observations. In consequence, having chosen a far field where the displacement is relatively higher than the magnitudes of the displacement from another far field, leads to obtain higher standard deviation, thus lower weight.

In a similar way, the weighting matrix for the second functional model is expressed by,

$$P_{b_2} = \begin{bmatrix} \frac{1}{0.0086} & 0 & 0 & 0 & 0 & 0 & 0 & 0 \\ 0 & \frac{1}{0.0043} & 0 & 0 & 0 & 0 & 0 & 0 \\ 0 & 0 & \frac{1}{0.2609} & 0 & 0 & 0 & 0 & 0 \\ 0 & 0 & 0 & \frac{1}{0.2420} & 0 & 0 & 0 & 0 \\ 0 & 0 & 0 & 0 & \frac{1}{0.0469} & 0 & 0 & 0 \\ 0 & 0 & 0 & 0 & 0 & \frac{1}{0.0468} & 0 & 0 \\ 0 & 0 & 0 & 0 & 0 & 0 & \frac{1}{0.4482} & 0 \\ 0 & 0 & 0 & 0 & 0 & 0 & 0 & \frac{1}{0.4211} \end{bmatrix}$$

$$P_{b_2} = \begin{bmatrix} 116.16 & 0 & 0 & 0 & 0 & 0 & 0 & 0 \\ 0 & 231.74 & 0 & 0 & 0 & 0 & 0 & 0 \\ 0 & 0 & 3.83 & 0 & 0 & 0 & 0 & 0 \\ 0 & 0 & 0 & 4.13 & 0 & 0 & 0 & 0 \\ 0 & 0 & 0 & 0 & 21.31 & 0 & 0 & 0 \\ 0 & 0 & 0 & 0 & 0 & 21.36 & 0 & 0 \\ 0 & 0 & 0 & 0 & 0 & 0 & 2.23 & 0 \\ 0 & 0 & 0 & 0 & 0 & 0 & 0 & 2.38 \end{bmatrix}.$$

And lastly, the weighting matrix for the last functional model is represented by the first and the last two values of the diagonal from the previous P_{b_2} matrix, expressed as,

$$P_{b_3} = \begin{bmatrix} \frac{1}{0.0086} & 0 & 0 & 0 \\ 0 & \frac{1}{0.0043} & 0 & 0 \\ 0 & 0 & \frac{1}{0.4482} & 0 \\ 0 & 0 & 0 & \frac{1}{0.4211} \end{bmatrix} = \begin{bmatrix} 116.16 & 0 & 0 & 0 \\ 0 & 231.74 & 0 & 0 \\ 0 & 0 & 2.23 & 0 \\ 0 & 0 & 0 & 2.38 \end{bmatrix}$$

where the significant difference between the weights of the observations is clearly evident. The weights assigned for the pixels corresponding to the displacement map obtained from ascending track (116.16 m^{-1}) and descending track (231.74 m^{-1}) observations obtained from interferometric processing represent around 50 and 100 times the weights for the pixels in the EW (2.23 m^{-1}) and NS (2.38 m^{-1}) displacement maps, respectively, obtained from offset tracking of optical images.

3.3.2.3 Case c. Weighting matrix obtained semi-variogram fitting

Finally, this last weighting matrix is the only case in which a full variance-covariance matrix for each displacement map, independently, is obtained. In contrast to the last two weighting cases, where every pixel within a displacement map was assigned the same weight, either 1 or $1/\sigma$, in this last case each pixel has its own different weight. However, the limitation of computing a full variance-covariance matrix is that it is computationally costly.

Considering first, that the deformation data obtained from radar observations are highly spatially correlated, reduction of information will not be significantly affected. In consequence, the data reduction applied in this case is called quadtree. The procedure of the algorithm starts by dividing the scene into four quadrants and compute their mean value. Then, the mean value of each quadrant is analyzed independently by comparing it with a given threshold. If each value exceeds the threshold, its corresponding quadrant is divided in four new quadrants, and the mean for each of them is computed and compared again with the threshold. This process continues iterative until convergence. The data reduced in such a way represent the statistically significant portion of the signal, but having reduced the number of sampling points [Jónsson et al., 2002].

In this study, the quadtree method was applied on displacements maps obtained from interferometric processing in ascending and descending tracks only because these two maps show less noise, thus the subdivision is more reliable. In order to better understand the concept of the quadtree algorithm, figure 3.22 demonstrating the data sampling for different given thresholds.

The upper maps shown in figure 3.22 represent the quadtree subdivision obtained after applying a threshold of 0.006 m. This value was the initial threshold to be assigned because the standard deviation already computed from the ascending and descending displacement maps in the far field, obtained after interferometric processing, was 0.0086 and 0.0043 m, respectively. In consequence, the mean value

between them is 0.006 m. Having obtained the first subdivision, the result showed that many of the pixels close to the faults were not possible to be assigned to any quadrant because the deformation in this regions is higher than the threshold. The second assigned threshold was 0.01 m, and the corresponding results are shown in the middle part of figure 3.22. Still, many pixels located close to the fault were ignored. Having finally set the threshold to 0.02 m, the quadtree subdivision is more representative far and close to the faults. Consequentially, this last value was threshold used in this study for quadtree subdivision. With this method, the number of samples was reduced from 44794 to 4167. It means that the full variance-covariance matrix represents the weight for each quadrant, and no longer for each pixel. As each quadrant is a representation of grouped pixels, the pixel to which the weight is assigned to is located in the center of gravity of each quadrant.

The open-source Geodetic Bayesian Inversion Software (GBIS) developed by the University of Leeds [Bagnardi and Hooper, 2018], is the tool used to computed the full variance-covariance matrix for this last weighting case. The steps involved in the semi-variogram computation is to first remove a linear ramp from the data so that the experimental semi-variogram is estimated on the detrended dataset, and finally fit an exponential function with nugget. The parameters describing the best fitting exponential function with nugget are sill, range and nugget. In order to find to fully explore the dataset and best characterize the spatially correlated noise in the data, it is recommended to repeat the estimation of the parameter several times [Bagnardi, 2018].

When the semi-variogram for each case is obtained, the variance-covariance matrix is computed from equation 2.15. This full matrix is then inverted, and final the weighting matrix which corresponds to the each of the three functional models are represented as,

$$P_{c1} = \begin{bmatrix} P_{rAsc(I)} & 0 & 0 & 0 & 0 & 0 \\ 0 & P_{rDes(I)} & 0 & 0 & 0 & 0 \\ 0 & 0 & P_{aAsc(OT)} & 0 & 0 & 0 \\ 0 & 0 & 0 & P_{aDes(OT)} & 0 & 0 \\ 0 & 0 & 0 & 0 & P_{rAsc(OT)} & 0 \\ 0 & 0 & 0 & 0 & 0 & P_{rDes(I)} \end{bmatrix}$$

$$P_{c2} = \begin{bmatrix} P_{rAsc(I)} & 0 & 0 & 0 & 0 & 0 & 0 & 0 \\ 0 & P_{rDes(I)} & 0 & 0 & 0 & 0 & 0 & 0 \\ 0 & 0 & P_{aAsc(OT)} & 0 & 0 & 0 & 0 & 0 \\ 0 & 0 & 0 & P_{aDes(OT)} & 0 & 0 & 0 & 0 \\ 0 & 0 & 0 & 0 & P_{rAsc(OT)} & 0 & 0 & 0 \\ 0 & 0 & 0 & 0 & 0 & P_{rDes(I)} & 0 & 0 \\ 0 & 0 & 0 & 0 & 0 & 0 & P_{EW} & 0 \\ 0 & 0 & 0 & 0 & 0 & 0 & 0 & P_{NS} \end{bmatrix}$$

$$P_{c_3} = \begin{bmatrix} P_{rAsc(I)} & 0 & 0 & 0 \\ 0 & P_{rDes(I)} & 0 & 0 \\ 0 & 0 & P_{EW} & 0 \\ 0 & 0 & 0 & P_{NS} \end{bmatrix}$$

where each element of the diagonal are no longer only one value, but a full variance-covariance matrix for each of the displacement map. The best exponential function fitting for each of the displacement map obtained from interferometric and offset tracking processing of radar and optical observations are shown in figure 3.14, 3.16, 3.18 and 3.20. The left side of each image represents the experimental semi-variogram calculated on the original dataset, and the right side shows the experimental semi-variogram calculated on the detrended dataset.

Having a closer look in the range parameter, one can say that it describes the distance until which the correlation between observations exists. The range for both, ascending and descending displacement maps obtained from interferometric processing shows that the correlation between the observations is obtained at distances not longer than 1.3 km and 1.6 km, respectively. This result agrees with the fact that the atmospheric conditions have been proved to vary in almost a kilometer scale. [Hanssen et al., 1999] mention an example considering a thunderstorm, whose initiation and strength are sensitive to spatial and temporal variations in moisture of the order of 1 g per kilogram of dry air, and temperature of 1° to 3° within 1 km. In contrast, the range value for the displacement maps obtained after applying offset tracking processing along the azimuth and range direction of Sentinel-1 images shows that the correlation can reach around 400 m and 230 m, respectively. In the case of the correlation obtained for the displacement maps coming from offset tracking applied to Sentinel-2 images, the range shows a significant difference between the EW and NS direction. For the EW direction, the range reaches almost 600 m, while for the NS direction, it approaches 80 m.

As all the calculations after applying the quadtree subdivision are referred to the center of each quadrant, and in order to recover the same number of initial points for mapping representation purposes, the obtained value for the center (e.g weights) is assign to all the points that belong to the same quadrant. An example of this representation is shown in figures 3.15, 3.17, 3.19 and 3.21. Each of these maps illustrates the magnitude of the weights obtained from the semi-variogram fitting. Based on these results, the highest magnitude of the weights was obtained for the observations derived from interferometric processing, reaching values higher than $2 \times 10^6 \text{ m}^{-1}$ and $4 \times 10^6 \text{ m}^{-1}$ for the ascending and descending tracks, respectively. The second highest weight magnitude comes from the results obtained after offset tracking processing in the range direction with values higher than 1000 m^{-1} and 1400 m^{-1} for the ascending and descending observations, respectively. Finally, as expected, the two lowest assigned weights under this method corresponds to the observations for the offset tracking processing in the azimuth direction of Sentinel-1 and Sentinel-2 images.

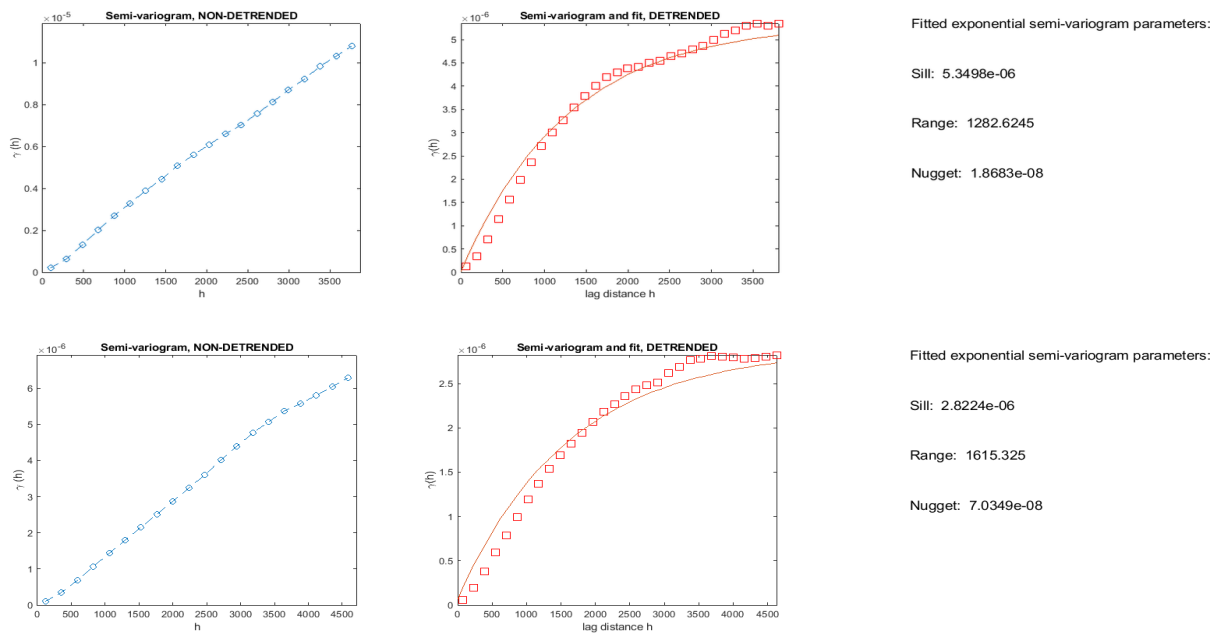


Figure 3.14: Semi-variogram fitting and parameters for displacement maps in the ascending track (up) and descending track (down) obtained from interferometric processing

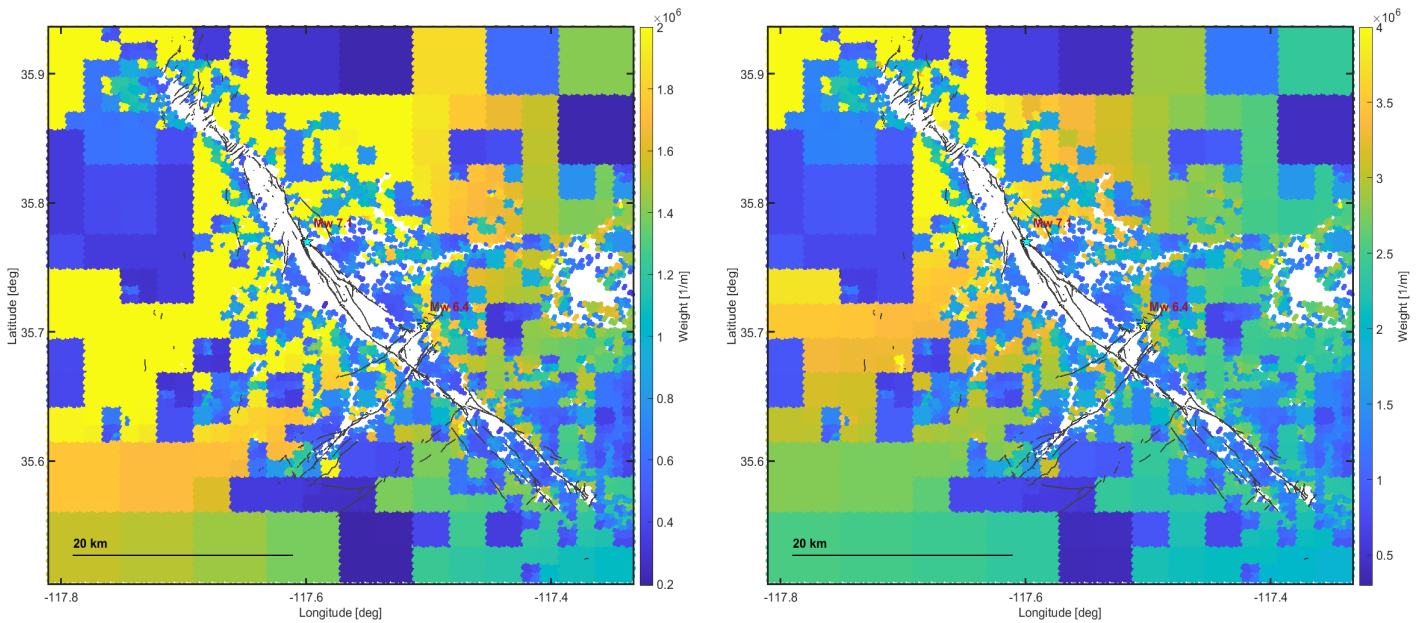


Figure 3.15: Weights assigned for the ascending track (left) and descending track (right) obtained from phase interferometric processing

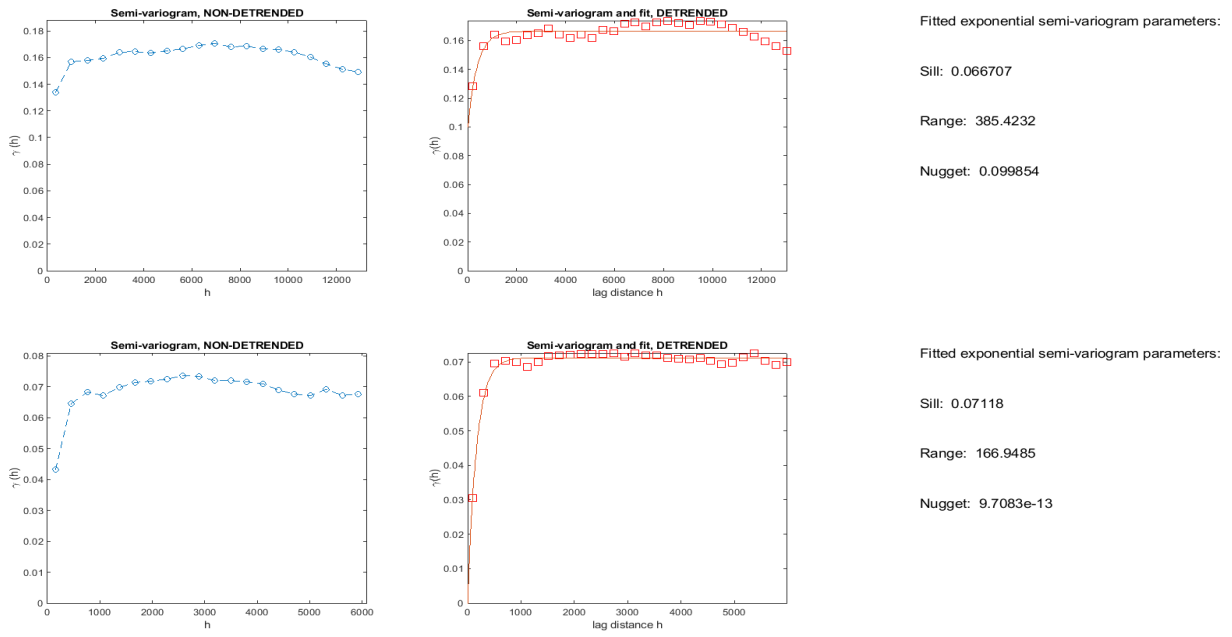


Figure 3.16: Semi-variogram fitting and parameters for displacement maps in the ascending track (up) and descending track (down) obtained from offset tracking processing along the azimuth direction

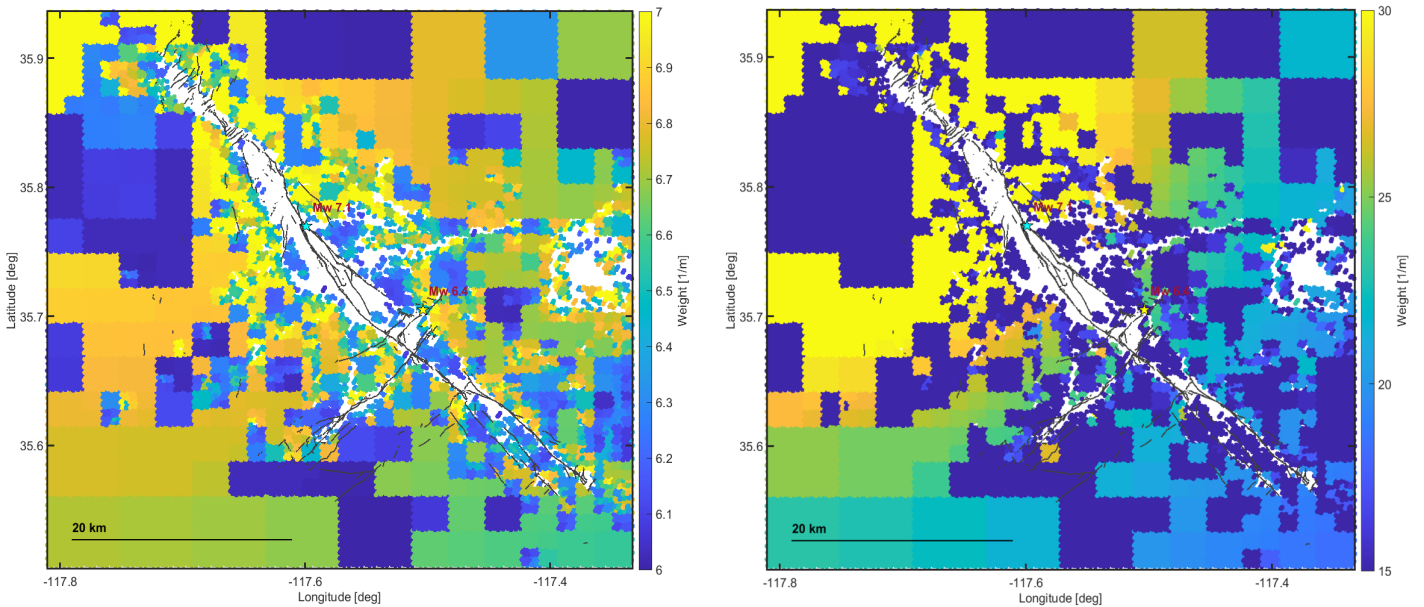


Figure 3.17: Weights assigned for the ascending track (left) and descending track (right) obtained from offset tracking processing along the azimuth direction

3.3 Radar and Optical Observations Combination

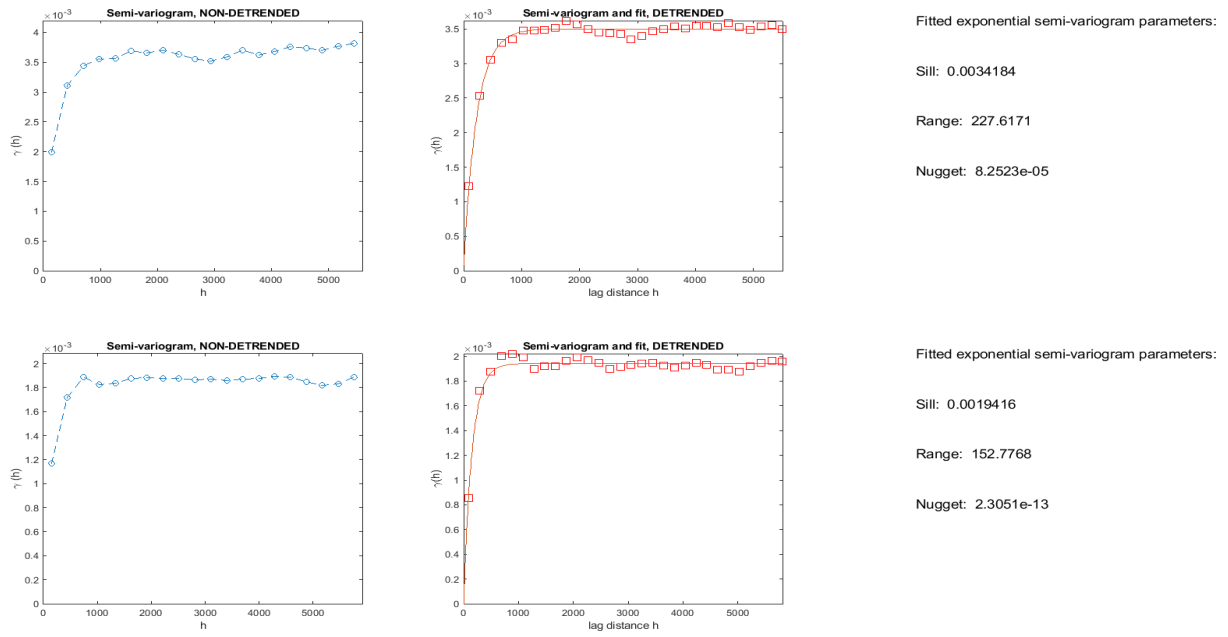


Figure 3.18: Semi-variogram fitting and parameters for displacement maps in the ascending track (up) and descending track (down) obtained from offset tracking processing along the range direction

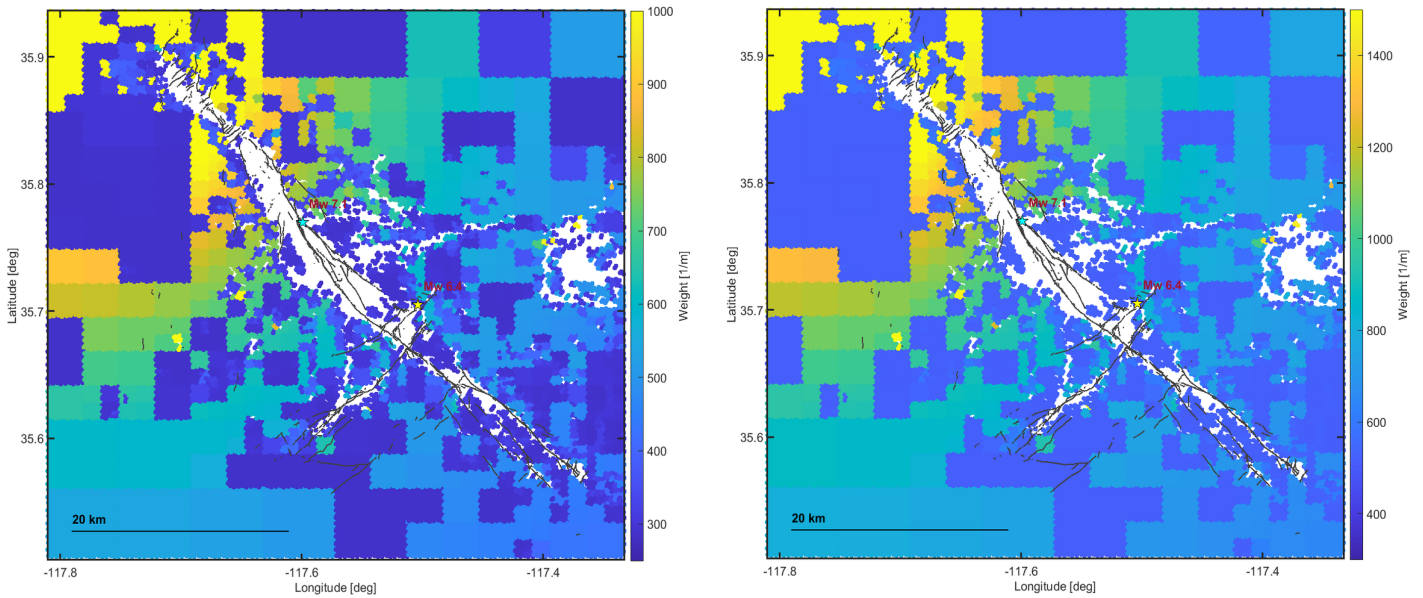


Figure 3.19: Weights assigned for the ascending track (left) and descending track (right) obtained from offset tracking processing along the range direction

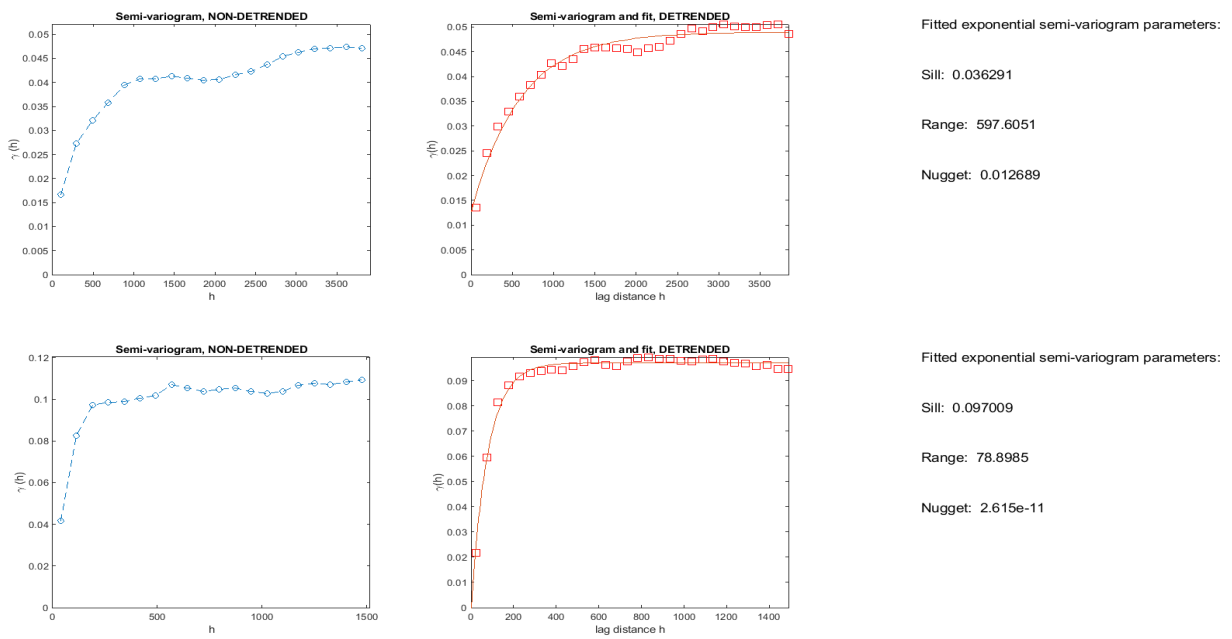


Figure 3.20: Semi-variogram fitting and parameters for displacement maps in the NS direction (up) and EW direction (down) obtained from offset tracking processing of optical observations

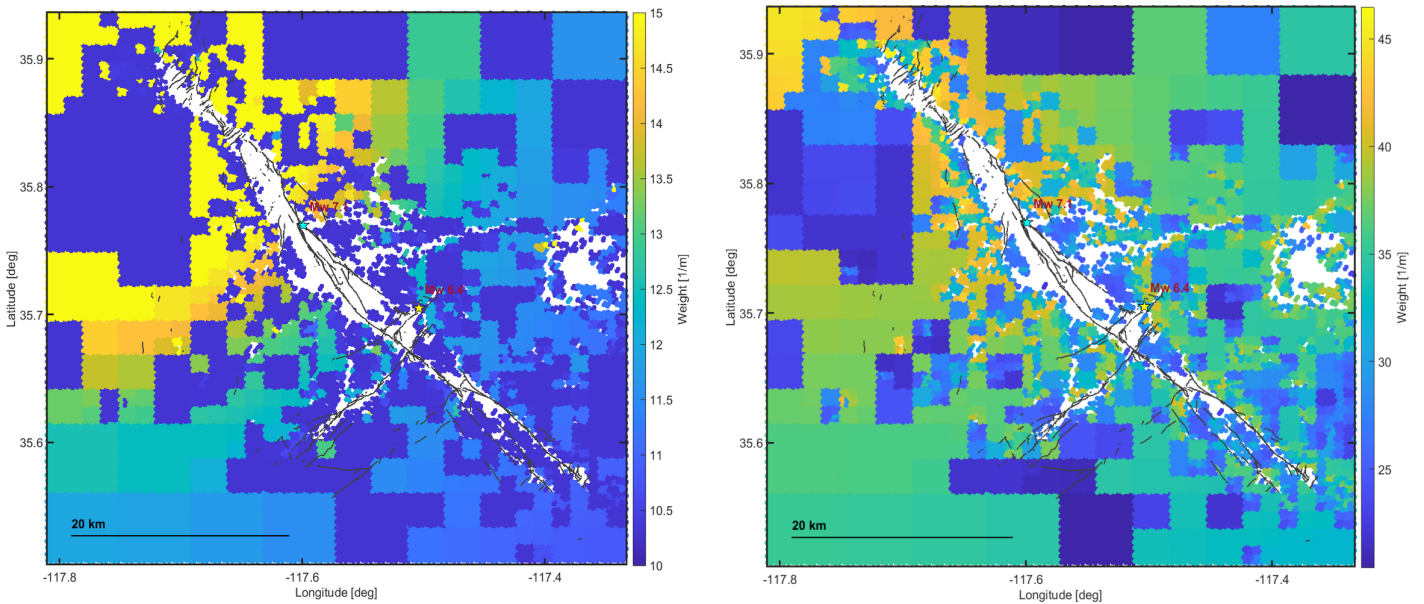


Figure 3.21: Weights assigned for EW direction (left) and NS direction (right) obtained from offset tracking processing of optical observations

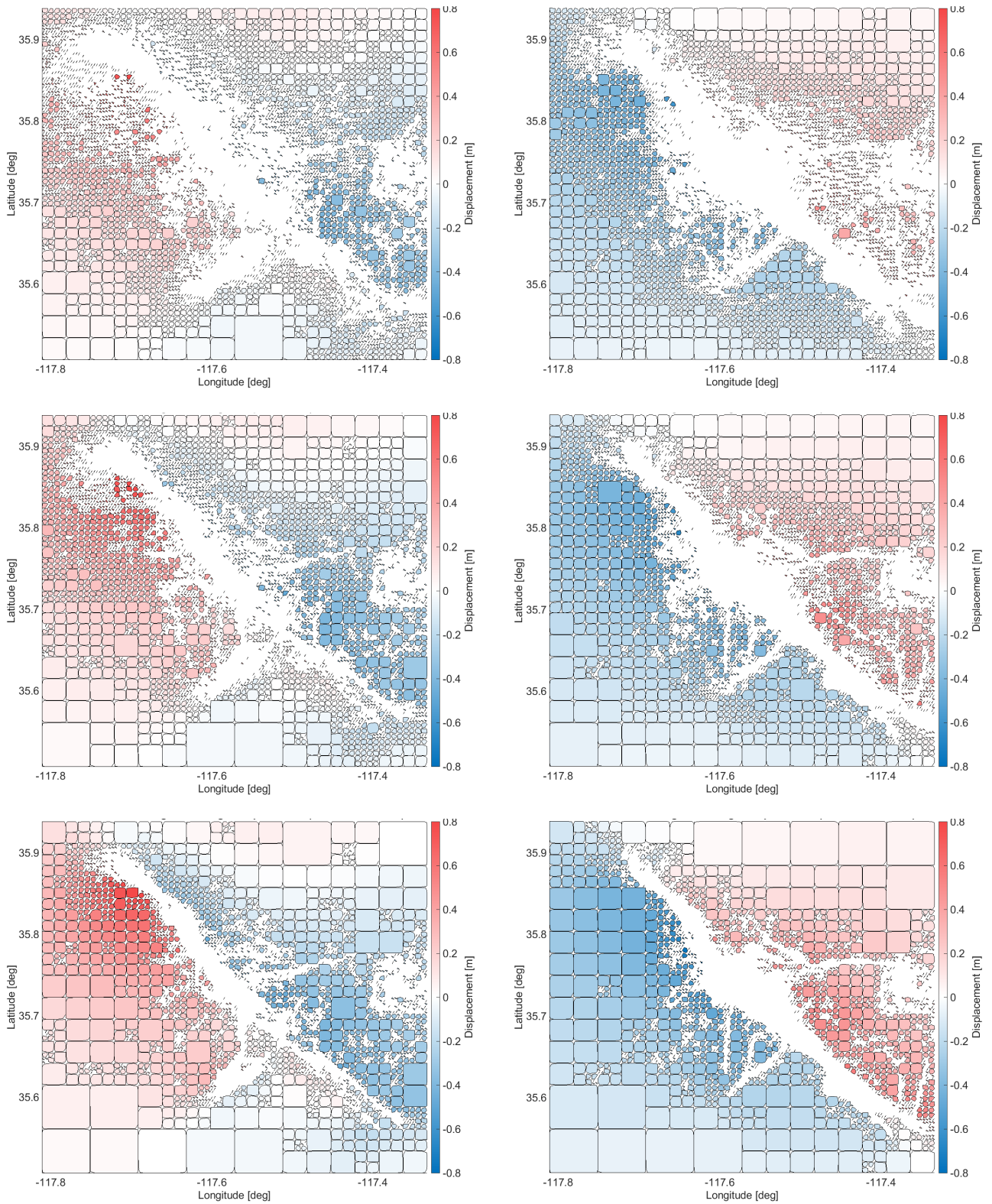


Figure 3.22: Quadtree division for the ascending track (left) and descending track (right) after setting a threshold value of 0.006 m (up), 0.01 m (middle) and 0.02 m (down)

4 Results

This last chapter provides, not only all the displacement maps that were obtained after combining radar and optical observation, but also a comparison between each combination and weighting case. Additionally, the assessment of the results with respect to GNSS measurements will give a better insight of the benefits and the limitations of the study, which leads to finally the description of the possible and future improvements to be considered.

4.1 3-Dimensional Decomposition

Having obtained displacement maps of the ground movement that happened after the 2019 Ridgecrest earthquakes based on different processing methodologies and observations, it is now clear that the limitation of each of them is the impossibility to show a full 3-dimensional displacement. Therefore, the combination of those displacement maps by applying the mathematics that allow a proper combination, resulted in the 3-dimensional displacement maps shown in figures 4.1, 4.2 and 4.3. The three figures are sorted in three columns and three rows. The maps on the left most column provide the displacement in the East component, the column in the middle corresponds to the displacement maps in the North component, and the right column maps show the displacement in the Up component. In the case of the rows, the three maps from the upper row show the corresponding results of the decomposition applying LSA without weights, the three maps in the middle are the result of LSA with weights from the far field, and the three maps at the bottom correspond to the LSA performed with weights obtained from the semi-variogram fitting. The arrows shown in every map represent its horizontal displacement.

4.1.1 Sentinel-1 (Interferometric + Offset Tracking)

Figure 4.1 shows the 3-dimensional decomposition obtained after the combination of interferometric and offset tracking processing using Sentinel-1 products only. First, comparing the East component displacement maps for the three weighting cases (**a1**, **a2** and **a3**), it is possible to identify the noisiest map belongs to the case in which no weights to the observations was considered, which belongs to map **a1**. When the weights from the far field are added to the LSA, the results at **a2**

show a much more smoother map, in which the noise is mostly located very close to the fault only. In the case for the last displacement map of the East component shown in **a3**, the areas very close to the faults are not even possible to be retrieved because this last adjustment method depends on the quadtree subdivision, and as shown in figure 3.22, there is no chance to assign quadrants in the masked areas, where no information is left. Nevertheless, the improvement of the having taken into account the weights for the adjustment shown in maps **a2** and **a3** with respect to the non-weighted case, represented in map **a1**, is clearly evident. This fact is also shown from the arrows that describe the horizontal displacement. The arrows shown in map **a3** are heading the displacement more uniformly than the arrows shown in **a1** and **a2**.

In the case of the North and Up components, the results show a similar effect between them, but different from the results in the East component. The displacement maps obtained without considering weights in the adjustment (**b1** and **c1**) also show noise displayed in the whole area. However, the displacement maps obtained considering weights from the far field (**b2** and **c2**), show hardly any improvement with respect to the non-weighted case. The noise in maps **b1** and **c1** is displayed at map **b2** and **c2**. The only case where an enhancement is evident is when the full variance-covariance matrix is applied in the adjustment (**b3** and **c3**). However, the strongest visible features revealed in these last two displacement maps is first, again the lack information in the area close to the fault, and the effect of the quadrants subdivision. This last effect will be further discuss in the coming sections.

4.1.2 Sentinel-1 (Interferometric + Offset Tracking) + Sentinel-2

The second combination case (see figure 4.2), takes into consideration all the products from the previous combination, but adding the displacement maps obtained after applying offset tracking processing to the optical images. Analyzing again first the displacement in the East component for the three weighting cases, the result from map **a1** shows a considerably significant influence of the stripping effect previously evidence in the optical data generated displacement maps (see figure 3.10). However, a great improvement is visible when the weights from the far field (**a2**), and weights from the semi-variogram fitting (**a3**) are included in the LSA. On the other hand, the North and Up component show a very similar behaviour as the results in the previous combination. In the displacement maps **b2** and **c2**, the noise is still as evident as the represented in maps **b1** and **c1**, despite having add the weights from the far field. The noisy effect is only attenuated for the case when weights obtained from semi-variogram fitting are added into the adjustment, as shown in maps **b3**, and **c3**.

The effect that is even more evident in this case than in the previous combination results, is the patches shown in maps **b3** and **c3**, which are also as a consequence of the subdivision method. The squares shown in the bottom left corner of map **b3**, show sudden changes from positive (red) to negative (blue), which is not the case in the same map corresponding to first combination. This just confirms that the patches in this case are also influenced by the stripping effect coming from the included optical observations.

4.1.3 Sentinel-1 (Interferometric) + Sentinel-2

Finally, opposite to the first and second combination cases, this last combination excludes the contribution coming from displacement maps obtained after offset tracking processing, in range and azimuth direction, applied to the radar observations. The results shown in figure 4.3 for the East (**a1**), North (**b1**) and Up (**c1**) component obtained from non-weighted LSA, are the most influenced results, so far obtained, of the noise derived from the stripping effect which belongs to the optical observations. When the weights from the far field are included in the adjustment, the only improved results is, again, obtained for the East component (**a2**), while the North (**b2**) and Up (**c2**) components are, visually, showing no improvement of weighting. In the case of the East component, the stripping effect is almost completely gone from the weighting is applied in the adjustment, as shown in maps **a2** and **a3**.

Having already shown the strong effect of the quadrant in the displacement maps corresponding to North and Up components in the previous two combination cases, this last case is not the exception. Map **b3** and **c3** are again showing the lack of smoothness in due to the subdivision effect. This last case is the most obvious result to clearly see the direct relation between the stripping effect for weighted and non-weighted adjustment. The left side of map **b2** shows inclined stripes changing from blue to red color along the map, also seen in the quadrants from the same side of map **b3**.

From a previous study (see [Jónsson et al., 2002]), the combination of displacement maps in the range direction obtained from interferometric processing with displacement maps also for range direction, but coming from offset tracking processing, has not been applied because this last displacement map show contains noise which can be avoid if the source of information for the range direction comes from the interferometric processing results only. However, not considering the displacement map in the range direction obtained from offset tracking processing lead to miss valuable information close to the fault, which is not possible to recover from interferometric products only. The consequence of this effect is demonstrated in map **c2**, when not range nor azimuth displacement was included.

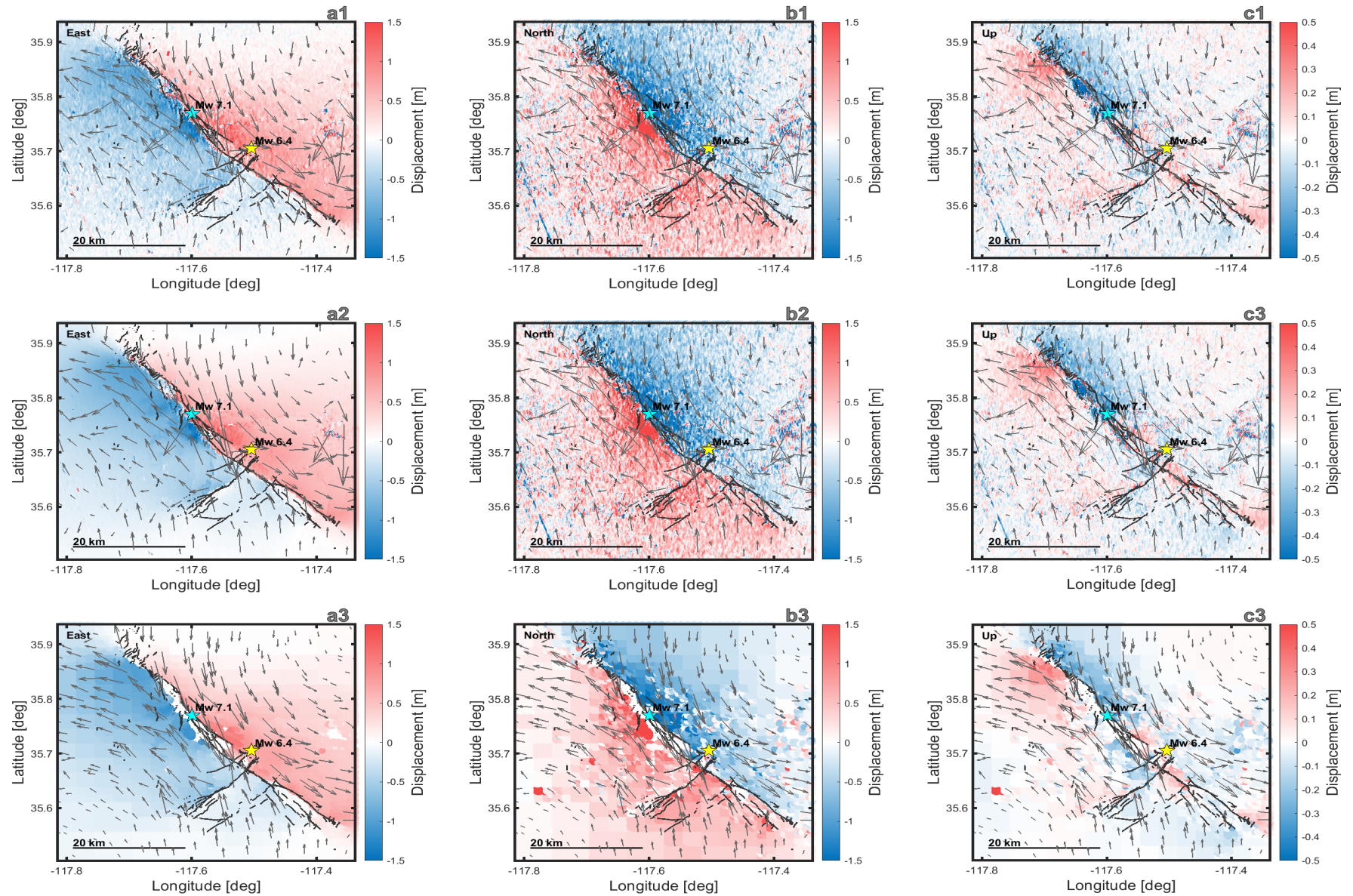


Figure 4.1: 3-dimensional displacement maps for combination of Sentinel-1 interferometry + offset tracking products and after LSA considering no weights (a1, b1, c1), weights from far field (a2, b2, c2), and weights from semi-variogram (a3, b3, c3). Faults and earthquake epicenters data courtesy of USGS

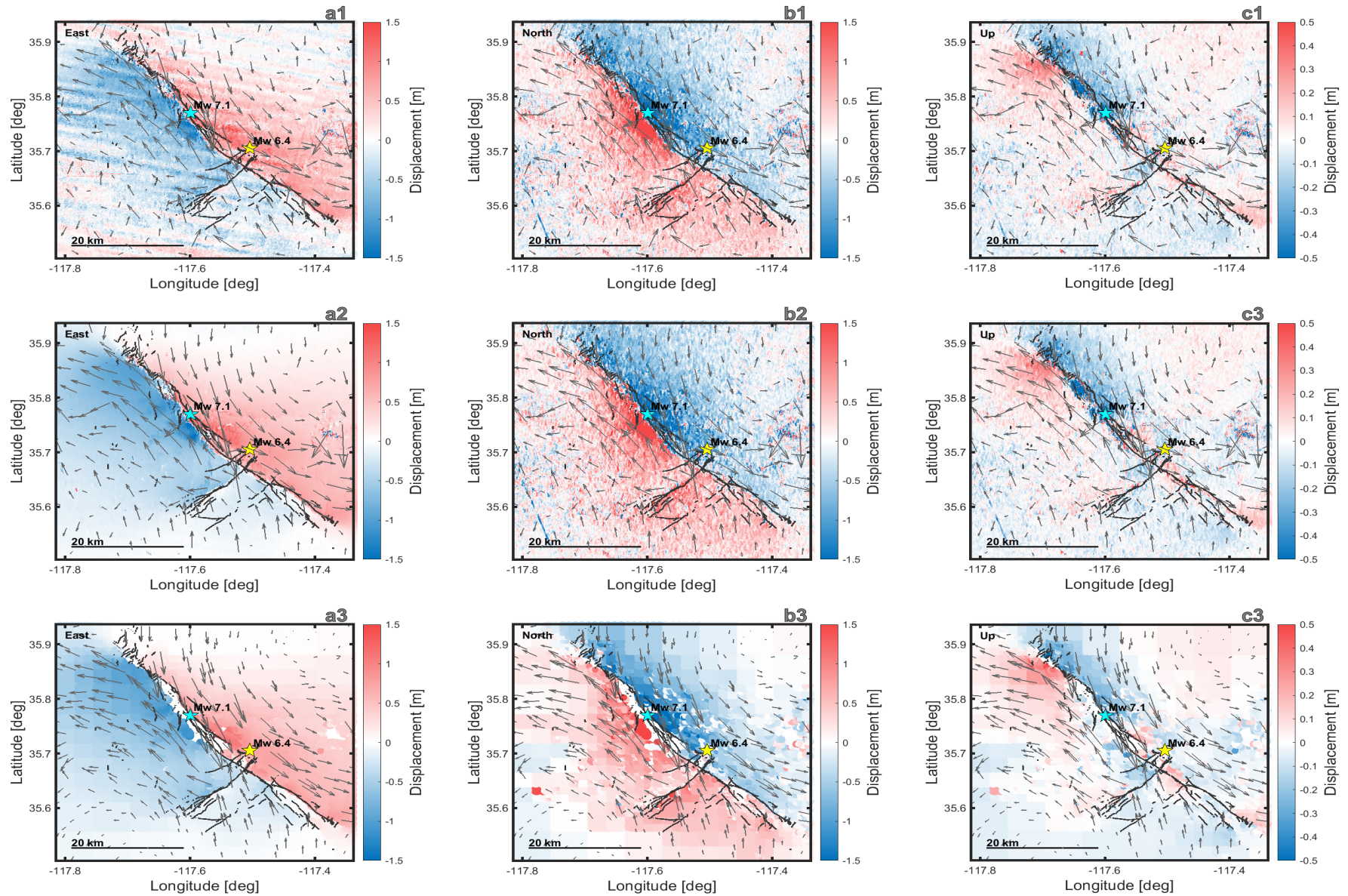


Figure 4.2: 3-dimensional displacement maps for combination of Sentinel-1 interferometry + offset tracking + Sentinel-2 products and after LSA considering no weights (a1, b1, c1), weights from far field (a2, b2, c2), and weights from semi-variogram (a3, b3, c3). Faults and earthquake epicenters data courtesy of USGS.

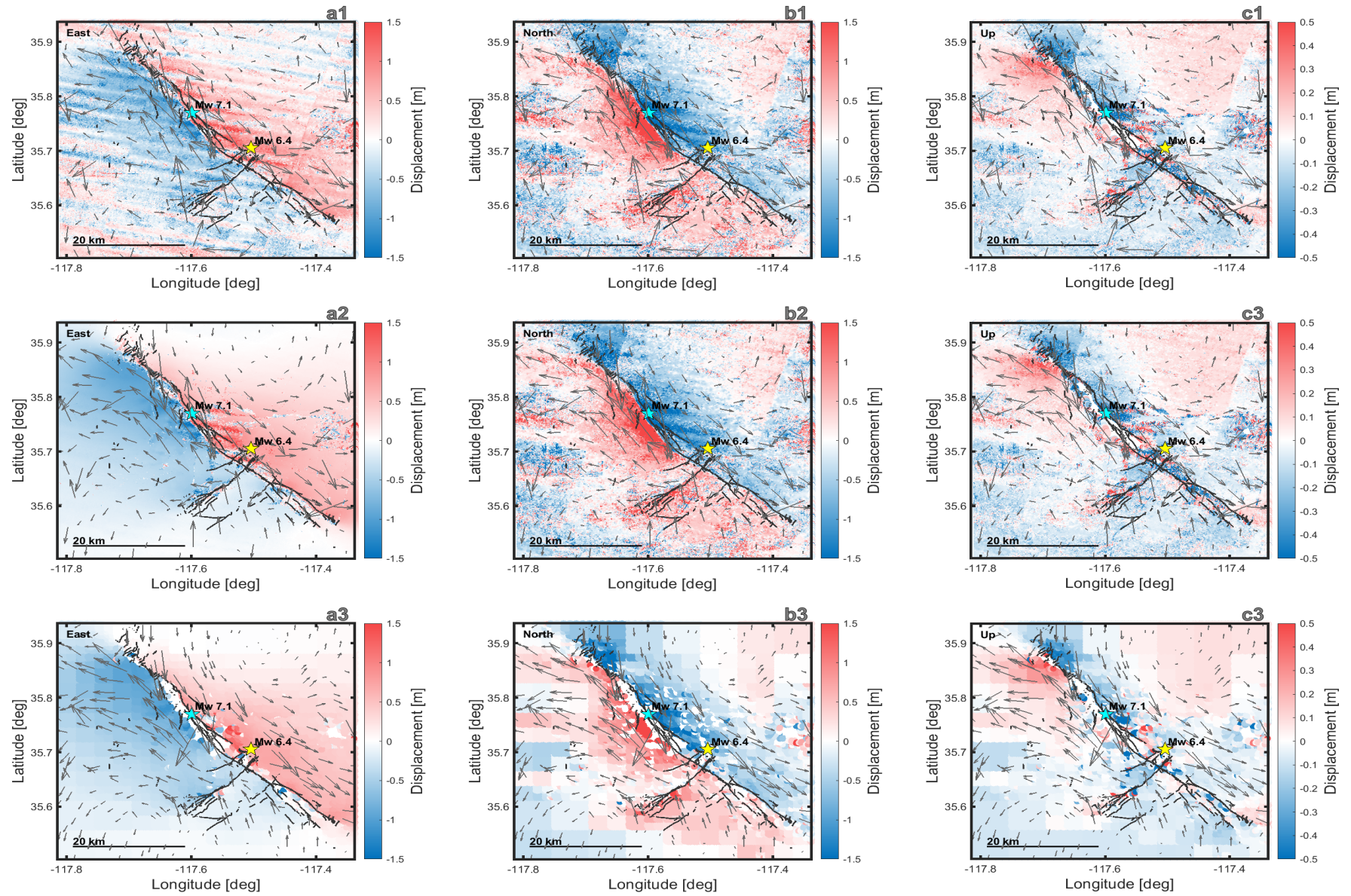


Figure 4.3: 3-dimensional displacement maps for combination of Sentinel-1 interferometry + Sentinel-2 and after LSA considering no weights (a1, b1, c1), weights from far field (a2, b2, c2), and weights from semi-variogram (a3, b3, c3). Faults and earthquake epicenters data courtesy of USGS.

To better evidenced the consequence of not including range only displacement map obtained from interferometric processing of radar images, a new combination was defined: interferometric products + offset tracking product in the azimuth direction only, from radar and optical images. This combination was compared to the already defined as the second combination, when all the obtained maps are included in the decomposition. This comparison is shown in figure 4.4. The areas inside the green rectangles from the East component maps are clearly representing the consequence of having not include the observations in the range direction other than the obtained from interferometric processing. Likewise, the orange rectangles are located in the regions where the Up component is mostly affected after the same range direction displacement maps exclusion.

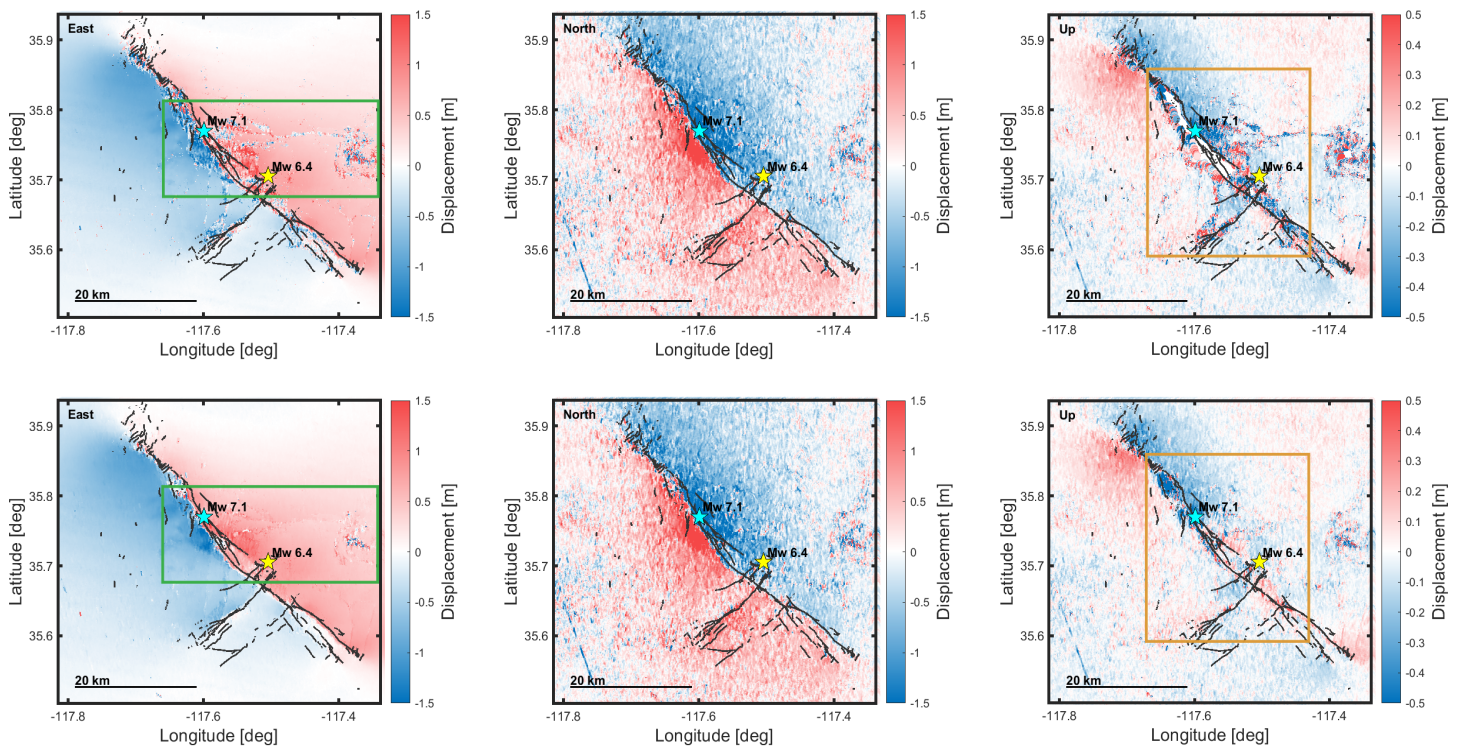


Figure 4.4: 3-dimensional decomposition for the combination of Sentinel-1 interferometry + offset tracking (azimuth only) products (up) and Sentinel-1 interferometry + offset tracking (range + azimuth) + Sentinel-2 products (down)

4.2 Validation

Having shown the displacement maps in the East, North and Up component, the results are validated by means of statistics. Figure 4.5 shows the standard deviation obtained after the adjustment for each component and for each combination case.



Figure 4.5: Standard deviation for East, North and Up component obtained from the three combination and weighting cases.

Based on the results shown in figure 4.5, the most important aspects to be highlighted are:

- The standard deviation for all the three components obtained from LSA without considering weights (cyan bars) are represented by the highest standard deviation magnitudes, in comparison with the ones obtained from the LSA using weights from far field (green bars) and from semi-variogram (purple bars).
- The standard deviation obtained after applying LSA with weights from far field is significantly reduced, in the order of 7 to 8 times, for East and Up component with respect to the standard deviation obtained without including weights in the adjustment. For the North component, the addition of weights from far field does only reduce its standard deviation by half of the value obtained when no weights were considered in the adjustment.
- The component with the lowest standard deviation for all the three combination cases is the East. The standard deviation is reduced around 40 times the value obtained from LSA considering weights from the far field (0.086 m), to the obtained when the LSA used weights from semi-variogram fitting

(0.002 m). The second most benefited component is the Up, and finally the North.

- The standard deviation for the North component is almost never better than the one corresponding to the East and Up component when either weighting cases, from far field or from semi-variogram fitting is considered. The only case when the standard deviation for the North component (0.587 m) is slightly better than the obtained for the East (0.617 m) and Up (0.656 m) is shown in the second combination case, and when no weights are considered in the adjustment.
- The standard deviation which shows the most, statistically, reliable results corresponds to the obtained from the second combination, which includes Sentinel-1 interferometric and offset tracking processing results with the ones coming from Sentinel-2 offset tracking processing, considering the two weighted LSA cases.

The 2019 Ridgecrest earthquakes sequence have been imaged not only by radar and optical sensors, but also by terrestrial and aerial light detection and ranging (lidar), drone photogrammetry, as well as campaign and continuous GNSS monitoring [Milliner and Donnellan, 2020]. Consequently, in order to additionally confirm the reliability of these results, performing a comparison of the displacement derived from images combination to the measured from GNSS stations has been also defined as a validation method due to the high accuracy of GNSS observations.

Several GNSS stations have been placed for monitoring the displacement in area of interest of this study. The stations from which were possible to retrieve the 3-dimensional displacement belong to the University of California, Riverside (UCR) and San Diego (UCSD), the University of Nevada (UNR) and the Scripps Orbit and Permanent Array Center (SOPAC). Tables 4.1 to 4.5 show all the obtained observations from the stations located inside the near field of study. Each table provides the displacement in the East and North component with its corresponding standard deviation in mm. The Up component is only provided from UNR and SOPAC.

Table 4.1: GNSS stations displacement in mm from continuous observations
University of California, Riverside (UCR)

Station	dN	sdN	dE	sdE
CCCC	225.1	1.64	-84.88	1.61
P594	-162.71	1.81	79.88	1.75
P595	-255.32	1.48	637.71	1.46
TOWG	47.13	2.46	-586.8	2.7

Table 4.2: GNSS stations displacement in mm from surveyed observations
University of California, Riverside (UCR)

Station	dN	sdN	dE	sdE
H701	70.61	3.56	-130.39	3.71
J701	84.95	3.12	-96.1	3.25
F048	92.58	3.81	-72.84	3.7
PASO	170.87	1.69	-23.15	1.6
PNCL	-354.87	4.94	790.2	4.62

Table 4.3: GNSS stations displacement in mm from surveyed observations
University of California, San Diego (UCSD)

Station	dN	sdN	dE	sdE
GS17	648.16	7.77	-81.9	6.89
GS48	553.43	13.97	-157.34	12.95

Table 4.4: GNSS stations displacement in mm from continuous observations
University of Nevada, Reno (UNR)

Station	dN	sdN	dE	sdE	dU	sdU
CCCC	213.14	0.46	-49.83	0.38	2.53	1.46
P594	-126.63	0.48	65.76	0.4	5.16	1.52
P595	-249.84	0.45	514.05	0.37	42.84	1.42

Table 4.5: GNSS stations displacement in mm from continuous observations
Scripps Orbit and Permanent Array Center, California Spatial Reference Center (SOPAC)

Station	dN	sdN	dE	sdE	dU	sdU
CCCC	215.2	5.0	-44.9	3.9	-0.2	5.0
P594	-128.5	4.9	74.6	3.8	8.8	5.0
P595	-256.1	4.3	519.6	3.4	35.4	4.4

In order to better visualize the displacement measured from each GNSS stations, figure 4.6 shows the vectors representing the horizontal displacement (East and North component) per station. Out of the whole group of stations, two groups can be identified. The stations which are constantly measuring and were already positioned before the earthquake are labelled as *continuous*, while the ones which were positioned only as part of a measuring campaign after the first earthquake (M_w 6.4) are identified as *survey*.

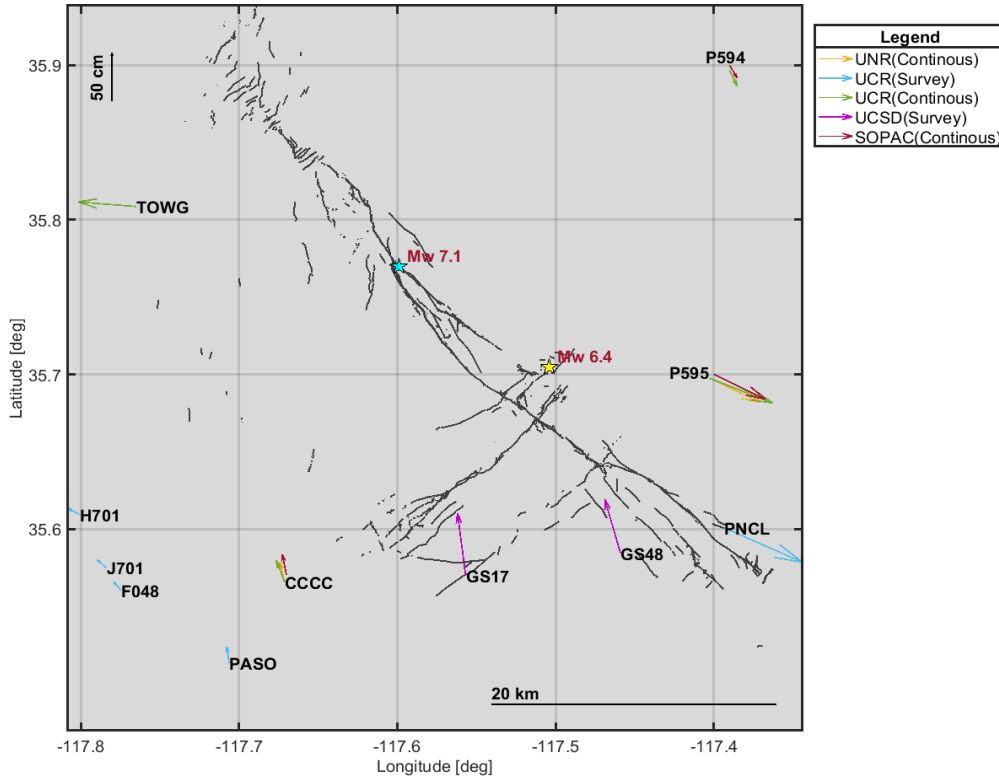


Figure 4.6: GNSS stations lying in the near field

As can be seen, stations *CCCC*, *P594* and *P595* are the stations at which the displacement has been obtained from three different solutions, showing discrepancies between them. In order to rely on a comparison to a single solution for each station, only one from the provided solutions per station has been chosen. The number of stations monitored, either continuously or surveyed, with the wider coverage of the area of interest (near field) belongs to the monitored and processed by the UCR and UCSD; therefore, stations *H701*, *J701*, *F048*, *PASO*, *PNCL*, *CCCC*, *P595*, *TOWG*, *GS17* and *GS48* are counted as reference for the validation of the displacement obtained in this study.

It is well known that GNSS observations provide 3-dimensional co-seismic surface displacement at individual observation locations. This is the reason why the spatial density is usually sparse or limited. On the other hand, imaging techniques can potentially measure the surface displacement across wide swaths with some

tens of meters between single data points [Sudhaus and Jónsson, 2009]. To be able to bring a compatible comparison of displacements between these two techniques, the first step was to identify the location of each GNSS station in every displacement map. Then, a radius around each station position was set in order to obtain only one averaged value to be assigned to each station. The idea was to extract more than one single displacement value to be compared to the displacement obtained with GNSS observations because, as mentioned above, the imaging technique is not determined point-wise, as the GNSS technique case. Therefore, taking into account that the closest distance determined between a GNSS station position and another point located in the displacement map is between 5 to 25 m, and after having applied different thresholds, the assigned radius was 100 m for the displacement maps obtained for the first and second combination and 300 m for the third case. The last combination needed a wider radius because the samples were reduced after having applied the quadtree algorithm. Finally, the horizontal displacement for the provided GNSS stations measurements and for the averaged displacement was calculated and displayed in vector representation.

In this way, figures 4.7, 4.8 and 4.9 show the discrepancies in direction between the displacement vectors obtained from GNSS observations and from the three image combination cases. Each of these figures provides three maps. The upper map corresponds to the horizontal displacement obtained from an adjustment without considering weights, the map in the middle corresponds to the displacement resulted from the adjustment using weights from the far field, and the last map is the representation of the displacement when the adjustment was performed with weights from semi-variogram fitting. All the arrows shown in magenta represent the displacement obtained from the results of this study, which from now on will be referred to as the displacement obtained from the 3-dimensional decomposition. The green and yellow arrows belong to the displacement for the surveyed and continuous GNSS stations, respectively. All the maps clearly show that the discrepancy between GNSS measurements and the decomposition performed in this study is different for each station.

Starting from figure 4.7, which provides the comparison of the GNSS stations displacement with the displacement obtained for the first combination, the vectors corresponding to station *TOWG* show, visually, a high agreement between each other. On the other hand, station *CCCC* shows a very significant discrepancy between its compared vectors in the case of non-weighted (**a1**) and weighted LSA from far field observations **b1**. The vectors representing the displacement obtained from the 3-dimensional decomposition point to the SW direction, while the vectors obtained from GNSS measurements point to the NW direction. This means that the discrepancy is mainly coming from the North component displacement. Similar situation can be seen for station *H701*. Additionally, stations *PASO*, *J701*, *F048* and *GS48*, also show discrepancy in the North component, but less significant. The situation for all the stations in map **c1** is different, as the discrepancies are clearly reduced, or improved. Focusing the attention again in station *CCCC*,

the vectors computed from the 3-dimensional decomposition point to the NW direction, very close to the vector obtained from GNSS stations. Station *TOWG* shows an agreement in which the vectors seem to be almost overlaying one another. This such improvement is mainly caused, as shown in figure 4.5, by the addition of the full variance-covariance matrix as weights from the semi-variogram fitting to the adjustment processing.

The differences obtained for the second combination case, in which Sentinel-2 offset tracking displacement maps are included in the decomposition, and shown in figure 4.8, are also specific for each station. Map **a2** shows a significant disagreement for station *PASO* and *FO48*, in which the vector obtained from the 3-dimensional decomposition is pointing almost completely towards the South, while its corresponding GNSS displacement vector points in NW direction. The direction of these vectors is then shifted to the SW when they represent the displacement obtained after LSA including weights from the far field, as shown in map **b2**. Almost the same effect is seen for station *GS48*, in which the direction of the compared vectors are strongly disagreeing. Moreover, map **c2** reveals that the displacement of station *TOWG* seemed to have been worsened in comparison to the results showed in map **c1** of figure 4.7, when the optical data was not added. The less influenced stations by the optical observations addition, compared again with the results from the previous combination, are *GS17*, *P595* and *PNCL*.

For the last comparison case, it can be directly conclude that the vector representation is, evidently, the most incompatible of all the comparisons cases, as shown in figure 4.9. Map **a3** pictures the totally opposite direction of the displacement vectors obtained for station *PASO*, and almost similar for station *FO48*. The results after having estimated the 3-dimensional decomposition based on LSA considering weights from the far field (**b3**) contributes to an improvement mainly for the same two, *PASO* and *FO48*, stations. A characteristic that is easily distinguishable for all the stations in map **c3**, when weights from semi-variogram fitting are taking part in the adjustment, is that the discrepancy of all the vectors is attributed in the NS direction only, while the EW direction agrees for every stations.

This analysis confirms the fact that the displacements are improved when the weighted LSA is performed, but also that the displacements are driven from specific and independent characteristics of the position for each station. To better judge the behaviour of all the stations numerically, the magnitude of the differences between the horizontal displacement obtained from GNSS measurements and from the 3-dimensional decomposition achieved in this study have also been computed. These differences are shown in figure 4.10 and 4.11. Both figures provide three bar charts which combine the differences obtained based on each combination and weighting case.

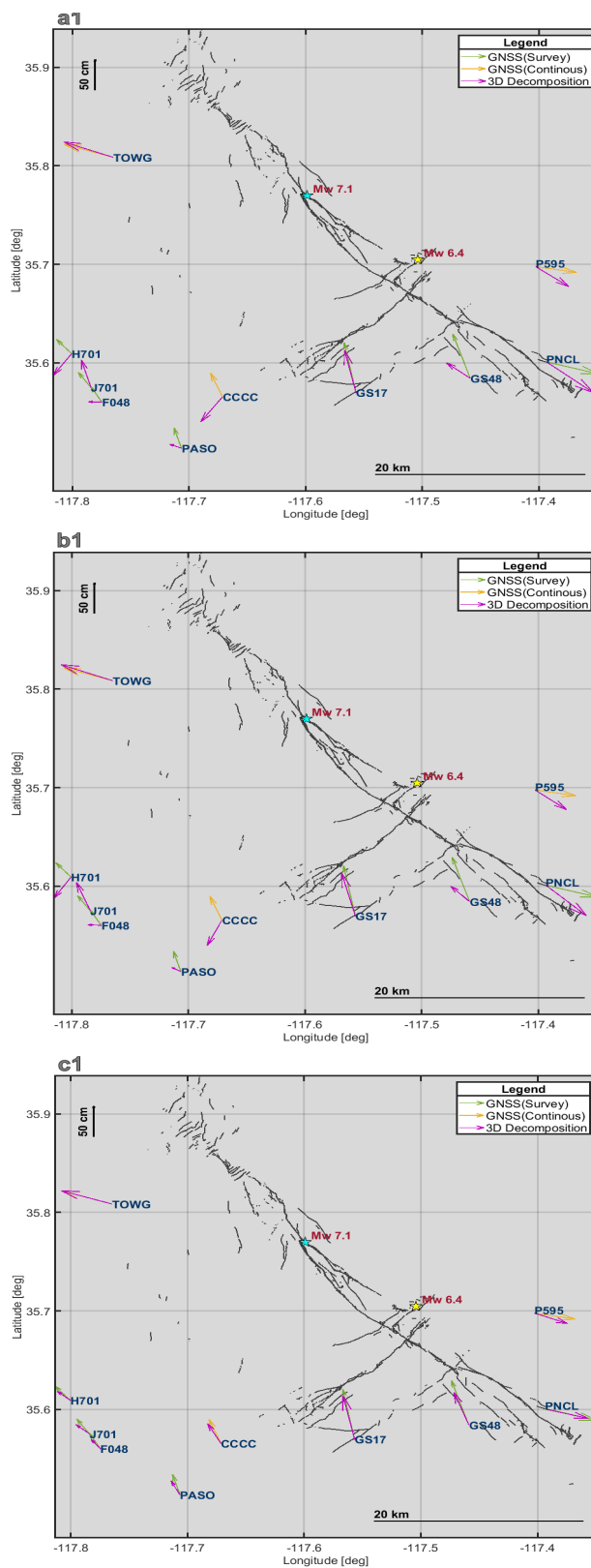


Figure 4.7: Horizontal displacement comparison between GNSS and the 3-dimensional decomposition derived displacement after combining Sentinel-1 interferometry + offset tracking products and based on LSA considering no weights (a1), weights from far field (b1), and weights from semi-variogram (c1). Faults and earthquake epicenters data courtesy of USGS, GNSS stations displacement courtesy of UCR-UCSD

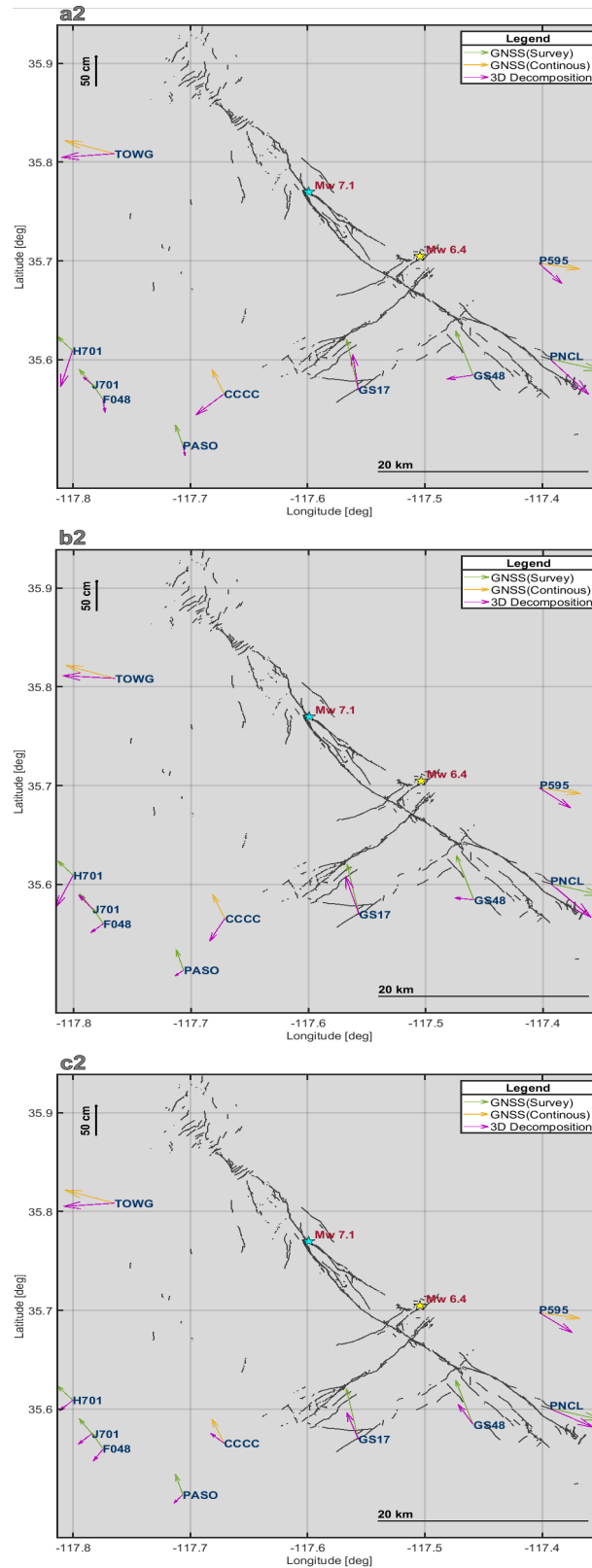


Figure 4.8: Horizontal displacement comparison between GNSS and the 3-dimensional decomposition derived displacement after combining Sentinel-1 interferometry + offset tracking + Sentinel-2 products and based on LSA considering no weights (a2), weights from far field (b2), and weights from semi-variogram (c2). Faults and earthquake epicenters data courtesy of USGS, GNSS stations displacement courtesy of UCR-UCSD

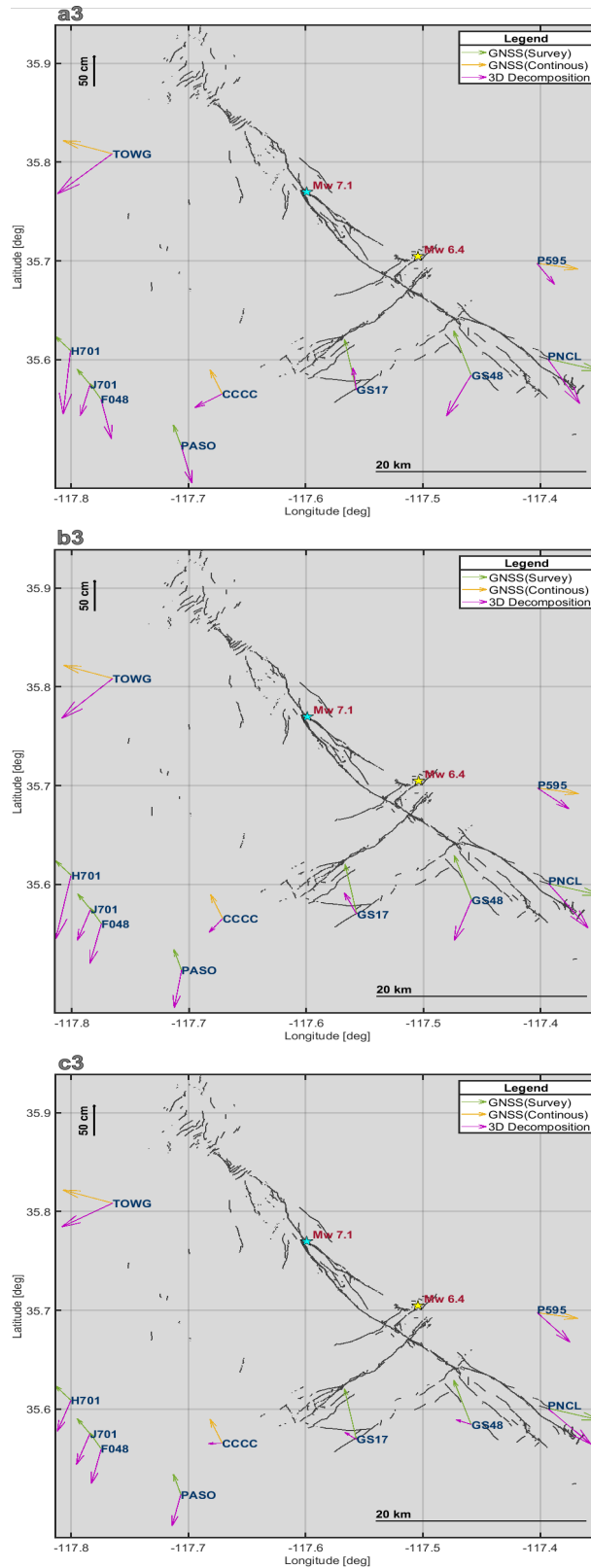


Figure 4.9: Horizontal displacement comparison between GNSS and the 3-dimensional decomposition derived displacement after combining Sentinel-1 interferometry + Sentinel-2 products and based on LSA considering no weights (a3), weights from far field (b3), and weights from semi-variogram (c3). Faults and earthquake epicenters data courtesy of USGS, GNSS stations displacement courtesy of UCR-UCSD

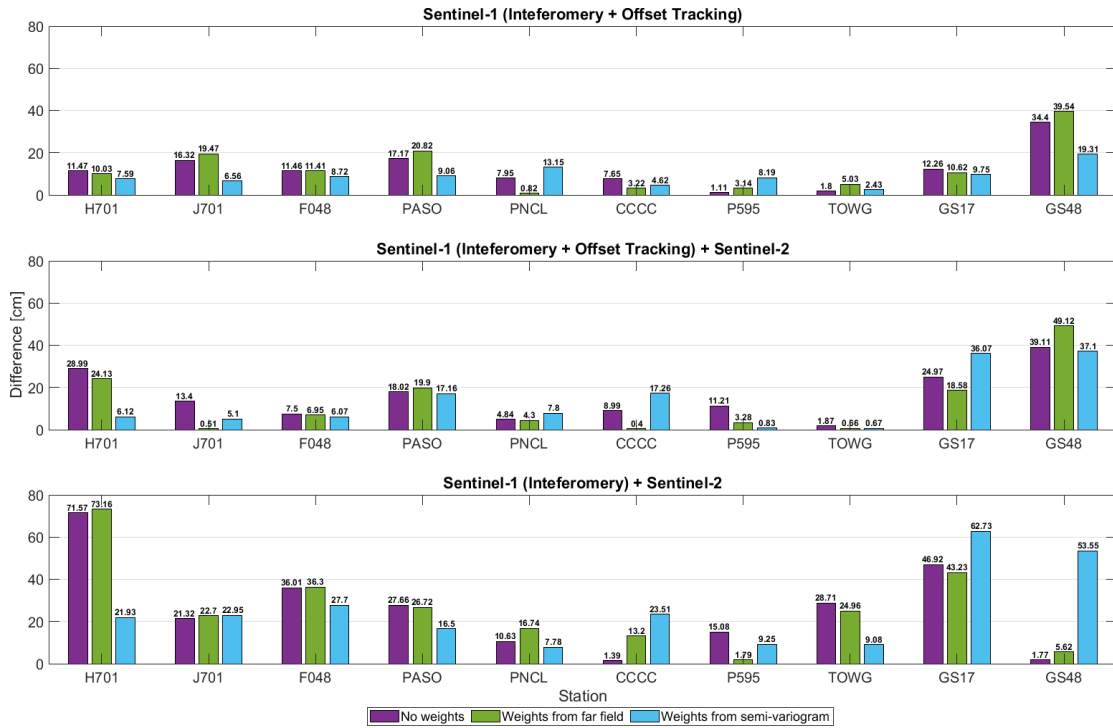


Figure 4.10: Horizontal displacement differences obtained GNSS observations and 3-dimensional decomposition, for each combination case

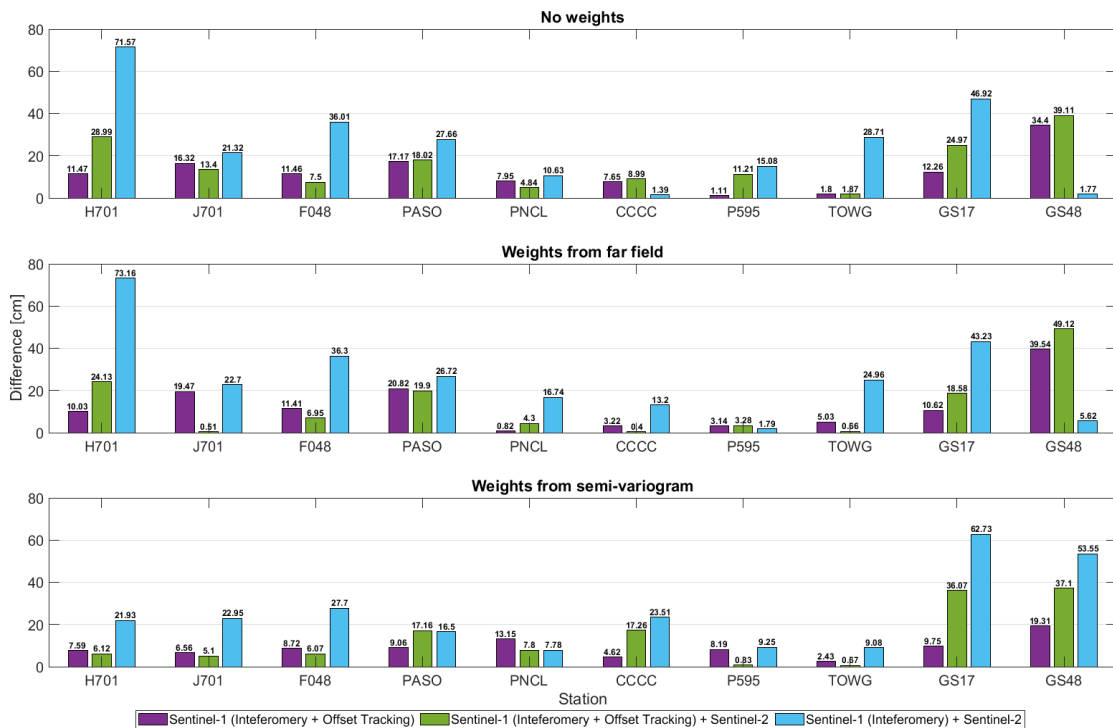


Figure 4.11: Horizontal displacement differences obtained GNSS observations and 3-dimensional decomposition, for each weighting cases

Figure 4.10 represents the discrepancy between the horizontal displacement obtained from GNSS observations and from the 3-dimensional decomposition for the three image combination cases. The up most chart will be referred as the results coming from the first combination, the middle chart as the ones coming from the second combination, and the lower chart as the proper for the third or last combination.

At first sight, the differences represented by the bars coming from the chart located in the bottom of figure 4.10 are, in general, showing the highest magnitudes, meaning that the third combination of the displacement maps is not the most suitable. However, one can see that for station *GS48*; the lowest discrepancy between the compared vectors is obtained in the last combination derived from the adjustment without weights (1.77 cm) and with weights from far field (5.62 cm). The case for station *F048* and *TOWG* is, in contrast, showing a better agreement between the vectors derived from the horizontal displacement of GNSS measurements and the second combination, while station *GS17* is definitely closer the magnitude of displacement obtained from GNSS observations when its displacement comes from the first combination.

Figure 4.11 is then is represented in a different arrangement as figure 4.10. In this second case, the upper most chart is representing all the three combinations when no weights are considered in the adjustment, the middle chart belongs to the case when considering weights from far field, and the lower chart corresponds to results of the weighted adjustment using the weighting matrix obtained from semi-variogram fitting. Analyzing the magnitude of the discrepancy of the vectors obtained from GNSS observation and from the three different weighting cases, figure 4.11 shows that the magnitudes for almost every station are lowered when weights coming from the full variance-covariance matrix, based on the semi-variogram fitting, is considered. The case with almost no significant improvement of having added weights to its estimation is evidenced for *TOWG* station. On the contrary, the difference in magnitude for station *J701*, when the displacement is obtained from the second combination and from the adjustment with weights from the far field, is only 0.51 cm in discrepancy with respect to the GNSS calculated magnitude, while its difference when no weights are considered reaches 13.4 cm. Finally, the few cases which are showing better agreement when no weights are considered in the adjustment are coming from station *P595* when estimated from the first combination and from station *GS48* resulting from the third combination case.

In order to have an overview of the best agreement in direction and magnitude together, between the compared vectors per station based on each combination and weighting case, table 4.6 compiles the obtained results. The three applied combinations are sorted in columns, *combination 1*: Sentinel-1 interferometric + offset tracking processing, *combination 2*: Sentinel-1 interferometric + offset tracking + Sentinel-2 offset tracking processing, and *combination 3*: Sentinel-1

interferometric + Sentinel-2 offset tracking processing. Each of these columns are subdivided in another three columns, which represent the weighting cases, *a*: no weights, *b*: weights from far field, and *c*: weights from semi-variogram fitting. The best obtained agreement in direction for each station is marked by \vec{v} , likewise for magnitude by $|\vec{v}|$.

Table 4.6: Direction and magnitude best agreement between GNSS per station

Station	Combination 1			Combination 2			Combination 3		
	a	b	c	a	b	c	a	b	c
H701			\vec{v}			$ \vec{v} $			
J701									\vec{v}
F048			\vec{v}			$ \vec{v} $			
PASO			\vec{v}						
PNCL			\vec{v}						
CCCC			\vec{v}			$ \vec{v} $			
P595			\vec{v}			$ \vec{v} $			
TOWG			\vec{v}			$ \vec{v} $			
GS17			\vec{v}						
GS48			\vec{v}						$ \vec{v} $

Based on the provided information on table 4.6, the stations whose vectors delivered the best agreement in direction and magnitude with respect to GNSS displacement vectors, obtained from a unique combination and weighting case are *PASO*, *PNCL* and *GS17*. All these stations show that the best combination is the first one when obtained from the LSA using the weights calculated from the semi-variogram fitting. The rest of the stations vectors provide the best agreement in direction and magnitude from the results obtained on a different combinations and weighting cases. For example, station *H701* agrees better in magnitude with the displacement measured by the GNSS technique when the 3-dimensional decomposition is obtained from the second combination, while the best agreement

in direction comes from the first combination, in both cases, considering the adjustment performed with weights from semi-variogram fitting. However, in general, table 4.6 shows that the most suitable combinations are the first considering weight form semi-variogram fitting, and the second combination considering either weighted adjustment cases. Finally, as expected, there are no stations which show to have achieved the best agreement considering combinations without using weights.

4.3 Limitations

After having analyzed the obtained results for each combination and weighting case, it is also important to analyze the limitations faced during the 3-dimensional decomposition, which also contributed to these the final outcomes.

One of the most limiting and significant factors of having obtained less degree of agreement in the direction and magnitude of the vectors for most of the stations is the noise introduced from Sentinel-2 products. In this case, noise is mainly referred to the stripping effect that was clearly visible on the EW and NS direction displacement maps obtained after offset tracking processing, shown in figure 3.10. After having demonstrated that this effect is coming from the sensors, and after direct communication with experts from California Institute of Technology (CALTECH), the suggestion for reducing the the stripping effect is by removing the median offset along each stripe direction. However, they added that a better way to perform this correction might be by taking into account the changing orientation of the look direction across the image. This two possible solutions to avoid the stripping effect was, of course, not covered in this, but is now contemplated for future improvements.

In addition, from the study performed by [Milliner and Donnellan, 2020], pixel offset tracking was better obtained from a new image correlation technique called Outlier-Resistant Correlator than from the common cross correlation method, using Planet Labs images instead of Sentinel-2 products. Planet Labs images are free of the stripping effect, and their spatial resolution higher. The limitation in this case, is that, opposite to Sentinel-2 products, Planet Labs images are not free of charge. However, an important contribution of the mentioned study is the comparison done for the final results obtained from offset tracking processing to Sentinel-2 and Planet Labs images. After having attempted to correct for the stripping effects in Sentinel-2 images, the obtained slip profiles for these two products have a strong agreement, demonstrated by a correlation coefficient of 0.95. Figure 4.12 shows the comparison of the surface-slip profiles for the foreshock and mainshock, measured from the deformation maps for Planet Labs and Sentinel-2 images.

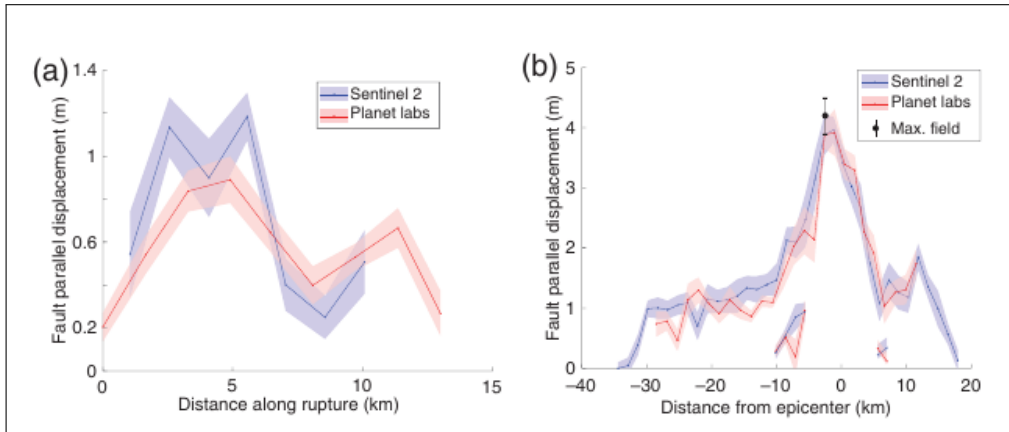


Figure 4.12: Surface-slip profiles for the foreshock (left) and mainshock (right) obtained from Sentinel-2 and Planet Labs images [Milliner and Donnellan, 2020]

Another limiting factor that needs to be mentioned is coming from the differences in the frequency between the observations obtained from Sentinel-1 and Sentinel-2 satellites with respect to the GNSS receivers. As explained in section 2.2, the temporal resolution of Sentinel-1 is 12 days, and 10 days for Sentinel-2. In contrast, the GNSS measurements are performed in a rate of one observation every 15 to 30 s. Considering that the observed frequency is very different, and that the GNSS observations were performed almost the same day when the events occurred, the validation of the 3-dimensional displacement is restricted to a certain degree of agreement due to the this observing condition of each technique.

4.4 Conclusions

The results obtained from the 3-dimensional decomposition coming from all the three performed combinations demonstrated that the right side of the main fault was moved around 1.5 m to East, while the left side was affected in the same magnitude, but to the West. The displacement in the North direction was evidenced mainly in the left side of the main fault, and the right side was dominated by a displacement towards the South, also reaching, for both cases, a magnitude of around 1.5 m. The less affected component was the Up. The ground was displaced from -0.5 m to 0.5 m in the Up and direction, heterogeneously distributed in both sides of the faults. The behaviour of these three components is clearly similar from all the results, despite the image combination and the weighting case. In this sense, all the outcomes are reliable. The different degree of confidence of the results is analyzed when trying to reach enhanced results by assigning weights to the observations.

The far field weighting case can be considered to be suitable for the variance estimation assuming that the far field is really free of noise so that it can be a significant sample of the complete area, including the near field. However, a much more adequate method to obtain the weights was demonstrated to be achieved from the semi-variogram fitting. All the results with this last case were smoother and less noisy than the obtained with the far field weighting method.

Additionally, the displacement computed from any of the weighted LSA cases is always, without any doubt, offering very much enhanced results for the East than for the North and Up components. This effect confirms the higher sensitivity that the observations from a side-looking system of a near-polar orbit satellite has over the EW direction when sensing the Earth's surface.

It is also important to mention that, even though the quality of the displacement maps are much more enhanced when considering their proper weights, a possible improvement to be tested can come from adding, not only the relative weights for each pixel within the same image but, the relative weights of the pixels between images. This study did not accomplish the computation of relative weights from image to image, but future calculations will, certainly, include this aspect. However, there are more options that could also be considered for the correct determination of the weights. For example, applying constraints. This means that, based on the obtained results, when performing the 3-dimensional decomposition by means of LSA, a constraint to the error structure can be set in order to avoid observations that are highly deviated from the expectations. The idea is to work with an algorithm that handles the possibility to remove a point which its deformation is out of the reality. When no such algorithm is achieved, an alternative could be to apply a proper scaling factor to the full variance-covariance matrix obtained from the semi-variogram fitting, meaning that each weighting matrix will be penalized if the observations provide noisy results, and rewarded when they provide more accurate results.

Finally, the 3-dimensional decomposition, close to the fault, is an important source of reliable information of how the surface slip varies along the rupture. Therefore, the efforts to bring together displacement maps coming from different viewing geometries, or sensing techniques, and that contribute to one of the limitations of the highly accurate interferometric products, which is the loss of coherence near to the faults, should still be studied, as it will always be place for proper improvements.

Appendix A

Phase Interferometric Processing

In order to compute the ground displacement of a specific region, Sentinel-1 images are one of the products which offer useful information for this application. The Interferometric Wide swath mode (IW) satisfies applications over land, such as earthquakes, by capturing images in three swaths. Each of the swaths is composed of burst that are separately processed as Single Look Complex (SLC) products [Veci, 2015].

In this case, ground displacement is obtained from phase observations only, which means that amplitude observations are not part of the processing. Figure A.1 shows the processing steps that need to be applied until phase unwrapping.

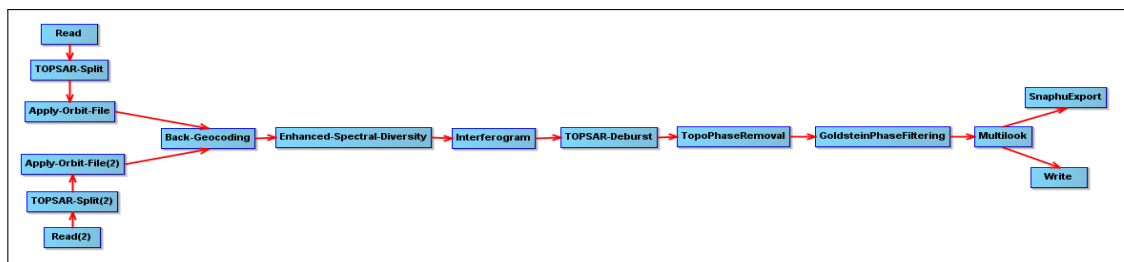


Figure A.1: Displacement processing until phase unwrapping

The processing steps are:

1. *Read*: Import the SLC products, the one before the earthquake (master) and the corresponding image after the earthquake (slave).
2. *TOPSAR-Split*: Allows to select one out of the three sub-swaths and the number of burst that covers the area of study. Processing least number of burst makes the processing faster, but the covered region will be smaller.
3. *Apply Orbit File*: Refines the orbit state vectors given on the metadata of SAR products by using precise orbit files which are normally available after some days or even weeks of the product generation.

4. *Back Geocoding*: Coregisters the master and slave images that belong to a same sub-swath by using their corrected orbits and a specified Digital Elevation Model (DEM).
5. *Enhanced-Spectral-Diversity*: Estimates a constant range offset for the previously chosen sub-swath by using incoherent cross-correlation. The estimation is done per burst from a block of data located at the center of each burst. The final constant range offset for one sub-swath is obtained from the average of the estimates applied to each burst. After that, a constant azimuth offset for the whole sub-swath is also obtained by applying Enhanced Spectral Diversity method. This method estimates the range offset in the overlapping regions and the final azimuth offset is obtained again, from average. Finally, this operator performs range and azimuth correction for each burst based on the computed offsets.
6. *Interferogram*: Computes the interferogram with the option of subtracting flat-earth phase. The flat-earth phase is part of the interferometric signal due to the curvature of the reference surface. This phase is computed in points distributed all over the image, and a second order polynomial is fitted to these observations. In this step, the fringes forming the interferogram will not be caused by earth curvature.
7. *TOPSAR Deburst*: Re-samples the image to a common pixel spacing grid in range and azimuth direction.
8. *Topographic Phase Removal*: Estimates and subtracts the topographic phase from the interferogram.
9. *Goldstein Phase Filtering*: Reduces the residues for the phase unwrapping step and enhances its accuracy.
10. *Multilooking*: Reduces speckled appearance and generates the squared pixels so that range and azimuth spacing are approximately the same, which improves the image interpretation.
11. *Snaphu Export*: Exports the bands in a compatible format with SNAPHU processing tool, creates a configuration file (*snaphu.conf*) where the processing parameters are stored, and constructs a container product which will store metadata and bands to be used when the SNAPHU results are being imported back into SNAP.
12. *Phase Unwrapping*: Unwraps the phase from the interferogram formation by using the external tool SNAPHU. For a successful phase unwrapping, there are important steps that need to be carefully applied.
 - Access the complete version of the configuration file *snaphu.conf.full* located in the *config* sub-folder from the downloaded SNAPHU package. Copy the very last section (Connected Component Control) into the

snaphu.conf file generated in the previous step, and uncomment the parameters which are defined in this section (e.g CONNCOMPFILE).

- Run the command line given in the header from the *snaphu.conf* file (e.g. `snaphu -f snaphu.conf Phase_ifg_VV_04Jul2019_10Jul2019.snaphu.img 3130`)
 - Copy the coherence file with the *.hdr* extension and name it as *snaphu.conncomp.hdr*. This is an ENVI format file which needs to be modified.
 - Edit data type to 1, which means it is an 8-bit unsigned integer ranging value from 0 to 255, and that image pixels are commonly represented as byte data [L3Harris, 2019]. Additionally, modify band names to *snaphu.conncomp*.
 - Import the *.hdr* file to SNAP from *File* → *Import* → *Generic Formats* → *ENVI*.
 - Right clic on *snaphu.conncomp* band and then clic on *Band Maths* → *Edit Expression* to obtain a most proper masked band by setting 0 values to NaN and keep 1 values the same.
 - Import the unwrapped result obtained from SNAPHU by *Radar* → *Interferometric* → *Unwrapping* → *Snaphu Import*.
13. *Phase to Displacement*: Covert the result into displacement by *Radar* → *Interferometric* → *Products* → *Phase to Displacement*. Once the displacement has been obtained, the next steps should be followed:
- Right clic on *displacement* band and then clic on *Band Maths* → *Edit Expression* to compute a multiplication between the relative displacement and the masked result obtained from *snaphu.conncomp* file.
 - Create a polyline in a region outside the deformation area and compute the statistics of these region from *Analysis* → *Statistics*.
 - Subtract the mean value obtained in the previous statistic analysis from the masked displacement result applying *Band Maths*.
14. *Geocoding*: Georeference the absolute masked displacement by *Radar* → *Geometric* → *Terrain Correction* → *Range–Doppler Terrain Correction*.

Appendix B

Amplitude Offset Tracking Processing

Once the results from ground displacement are obtained, there is possible to realize that there is a lack of information existing in the are where no coherence was possible to be obtained, which means, the deformation was too high so no correlation between the image before and the image after the earthquake was possible. Therefore, an alternative to retrieve the displacement in the regions with no coherence is offset tracking.

In order to obtain accurate results, a pre-processing needs to first be applied to the Sentinel-1 products, as shown in figure B.1



Figure B.1: Offset Tracking Pre-processing

The pre-processing steps are:

1. *Read*: Import the GRD products, the one before the earthquake (master) and the corresponding image after the earthquake (slave).
2. *Apply Orbit File*: Refines the orbit state vectors given on the metadata of SAR products by using precise orbit files which are normally available after some days or even weeks of the product generation.
3. *Thermal Noise Removal*: Removes the noise provided by Look Up Table (LUT) for each measurement data set. For GRD products, thermal noise vectors are converted to ground range coordinates and applied to the data by subtracting the noise from the power-detected image. When calibrating the product, the noise vector must be scaled by the corresponding calibration LUT, and once the calibrated noise profile has been obtained, the noise can be removed from the GRD data by subtraction [ESA, 2019c].

4. *Calibration*: Provides imagery in which pixel values can be directly related to the detected backscatter of the reflecting surface.

The pre-processing steps have to be applied for each of the GRD products. After this procedure has been done, figure B.2 shows the following steps needed to be applied for offset tracking processing.

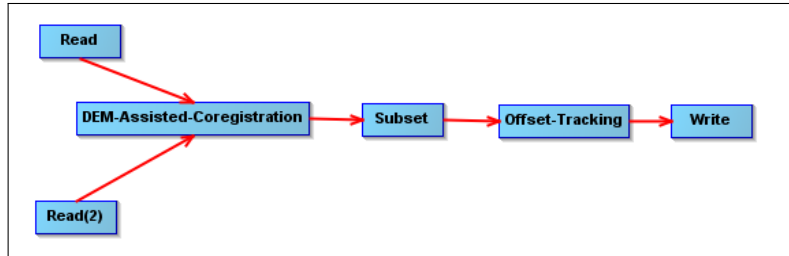


Figure B.2: Offset Tracking Processing

1. *Read*: Import the GRD calibrated products obtained after pre-processing.
2. *DEM-Assisted-Coregistration*: Coregisters calibrated products by using their orbits and a DEM.
3. *Subset*: Defines a subset out of the whole image in order to apply any further processing steps.
4. *Offset Tracking*: Estimates the movement of the surface between master and slave images in range and in azimuth direction. This operator performs cross-correlation on specific Ground Control Points (GCP) patches from both images, and computes the velocities based on the computed shift of each GCP. Additionally, a velocity map is computed through interpolation of the velocities computed from the GCP grid.

Once the velocity map has been computed, the velocity vector can be easily displayed using QGIS, from the following steps.

1. Import the .csv file of the velocity points generated from the grid, as shown in figure B.3. The csv. file contains information arranged by columns:
 - Latitude of the GCP from the master image
 - Longitude of the GCP from the master image
 - Latitude of the GCP from the slave image
 - Longitude of the GCP from the slave image
 - Distance [m]
 - Velocity [m/day]

- Heading East from North [deg]
- Range shift [m]
- Azimuth shift [m]

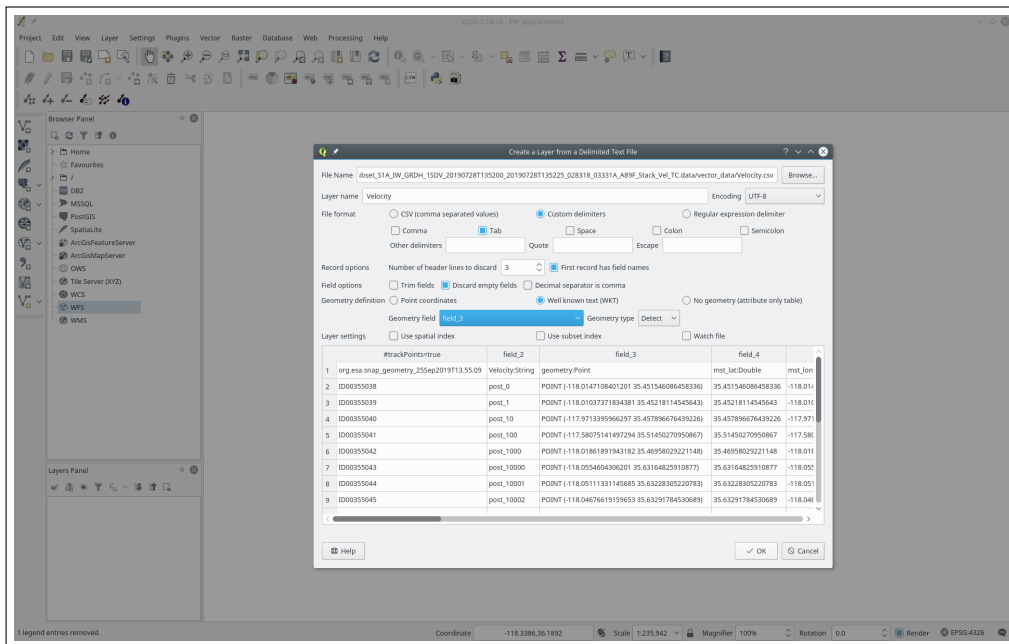


Figure B.3: Velocity points import - QGIS

2. Define the projection corresponding to the displayed velocity points by right clic over the layer and select *Properties* → *General* → *Coordinate reference system*.
3. Save the imported points by right clic of the layer and select the option *Save*.
4. Define a sample out of the total number of points in order to get a better visualization result. Clic on *Select by expression* option and introduce the expression to extract random points. For example, figure B.4 shows the expression used to extract 30% of the points.
5. Clic on *Processing* → *Toolbox* and search for *Save selected features*. Select as *Input Layer* the exported velocity points, and choose the corresponding name and path for the selected sample.
6. Install the *Vector field renderer* plug-in in order to be able to visualize the direction and magnitude of the velocity vectors.
7. Define a suitable visualization criteria for the vectors based on their velocity and heading, as shown in figure B.5
8. Import the velocity map generated in SNAP in order overlap it with the velocity vectors.

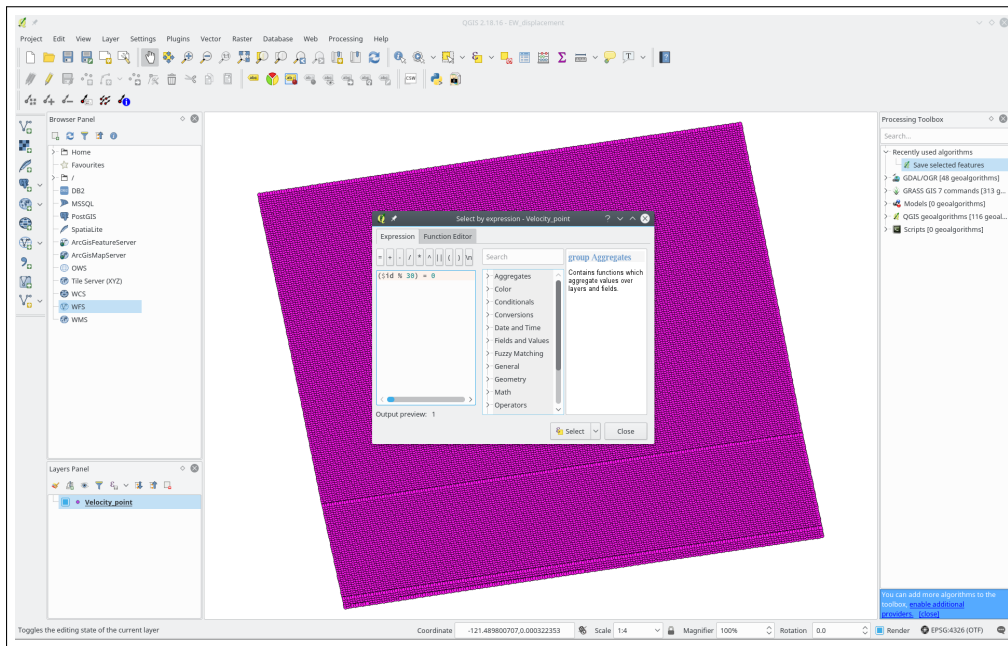


Figure B.4: Sample points extraction - QGIS

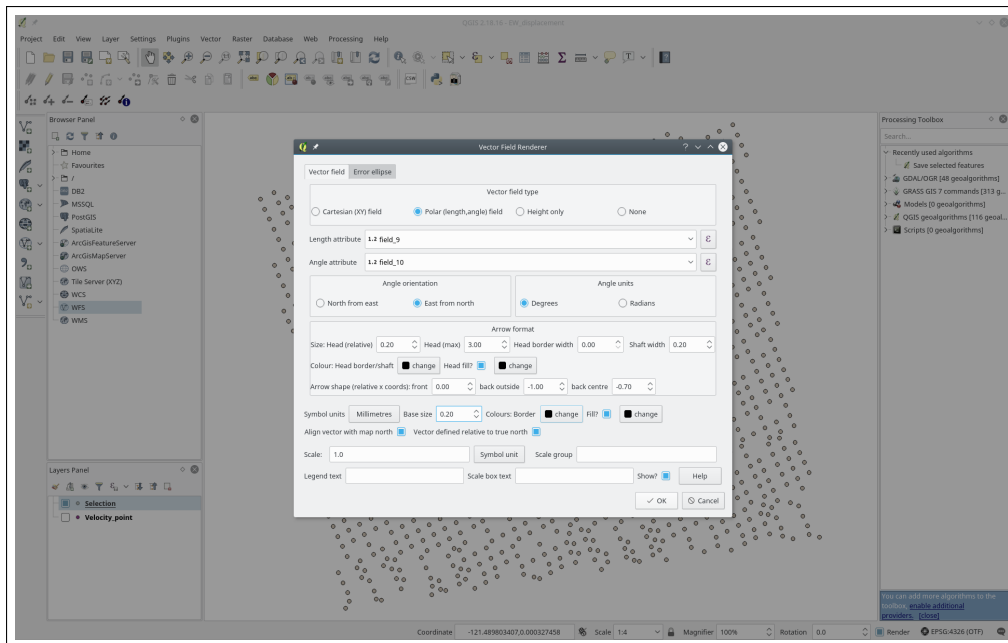


Figure B.5: Velocity vectors definition - QGIS

Appendix C

Cosi-Corr Image Processing

Subpixel correlation can be obtained by the tool called Cosi-Corr, which belongs to ENVI software. In this case, the following steps have to be applied.

1. Clic on *Cosi-Corr* → *Correlation* → *Correlation*
2. Select the input image for the corresponding pre-event and post-event image. The input images are the .tif files which were previously converted from .jp2.
3. Clic on the *Options* button. The *Frequency Correlator Parameters* window will be appeared. From this window it is possible to change the parameters of the cross-correlation method, as shown in figure

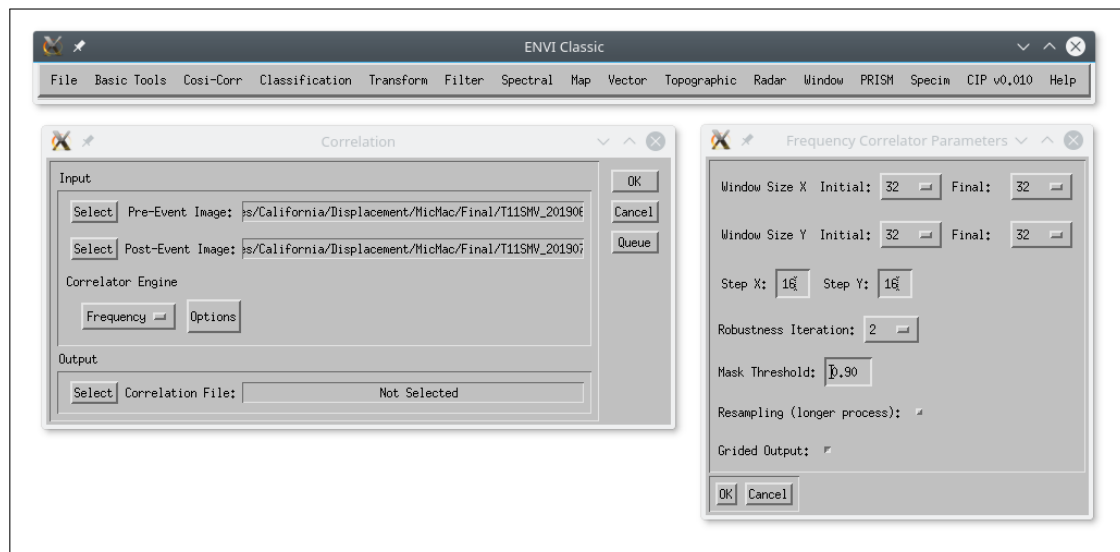


Figure C.1: Frequency Correlator Parameters Window - ENVI

The parameters that can be modified by the user are:

- *Windows Size Initial*: Initial size, in pixels, for the x and y direction, of the sliding window.

- *Windows Size Final*: Final size, in pixels, for the x and y direction, of the sliding window. *Step*: Step, in pixels, between two sliding windows for the x and y direction.
- *Robustness Iteration*: Number of iterations, generally between 2 and 4, per measurement that a frequency mask should be recomputed in order to reduce noise.
- *Mask Threshold*: Threshold that allows the masking of the frequencies according to the amplitude of the log-cross-spectrum, which should normally be close to 1.
- *Resampling*: Option to eliminate, theoretically, most of the biases at sub-pixel scale.
- *Gridded Output*: Option to obtain displacement map with the top-left corner coordinates to be integer multiple of the ground resolution, useful when several correlation of the same are need to be overlaid.

The output image will be the correlated product with three bands: East/West displacement, North/South displacement and Signal to Noise Ratio (SNR).

4. Export the first and second band into GeoTIFF format. Clic on *File* → *Save File As* → *TIFF/GeoTIFF*. A new window will be opened in order to define the spatial and spectral subset.
5. Clic on *Spectral Subset* and select the first band (East/West). Once this step is done, repeat the same process to export the second band (North/South).
6. Clic on *Cosi-Corr* → *Tools* → *Image Detrending*. Import the exported product from the previous step, and apply a spatial subset from the main deformation area.
7. Load the detrended product and then clic on *File* → *Save File As* → *TIFF/GeoTIFF*. Select the source where the detrended product will be stored.
8. Open the latest detrended product and one product before (trended) using QGIS. This step helps to compare the difference between these two products.

Appendix D

MicMac Image Processing

For processing Sentinel-2 data in order to compute subpixel correlation using the free software MicMac, the following steps need to be followed:

1. Convert images from .jp2 to .tiff format
2. Run MM2DPoSism command
3. Convert NS and EW displacement from pixel into metric units

D.1 Image format conversion

The conversion from .jp2 to .tif format can be successfully done by using the free software OTB, which can be downloaded from OTB download website. Once installed, the conversion is applied by launching Mapla launcher, as shown in figure D.1

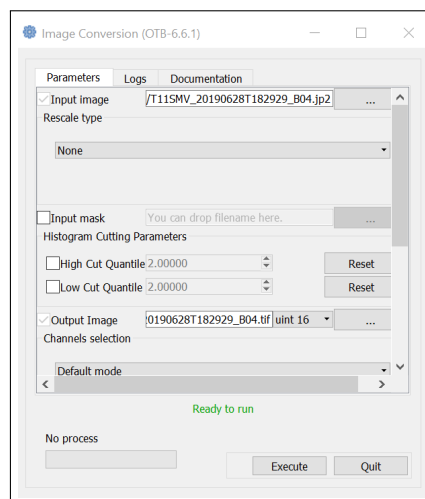


Figure D.1: Format conversion using OTB

The input image is the .jp2 Sentinel-2 product and output image will be the .tif product. It is important to mention that the output image has to be obtained as an unsigned integer 16-bit (uint16) product, otherwise; it will not be valid for MicMac. Finally, clic on 'Execute' and the conversion will be done in a few minutes.

D.2 MicMac **MM2DPoSisism** command runnig

When using Sentinel-2 products, the proper bands to apply subpixel image correlation are the ones with 10 m spatial resolution, which means band 2,3,4 and 8. There is no significant difference between band 2,3 and 4, but Copernicus uses band 4 for frame coregistration. Important to mention is that band 8 has to be carefully used as it is highly sensitive to vegetation feature reflectance which can dramatically change in few days.

MM2DPoSisism command can be run in MicMac in two ways:

1. Typing the command line directly.
2. Invoking an editable XML containing input file paths and run parameters. This option leads to manipulate more parameters so that the processing can be modified, therefore; a depth knowledge of the software code and theory is required.

This manual focuses in the first processing option. An example of the command line is:

```
mm3d MM2DPoSisism T11SMV_20190628T182929_B04.tif T11SMV_20190708T182929_B04.tif
```

The previous syntax starts with mm3d command, which is needed to invoke MicMac's tools, followed by the MM2DPoSisism command and the name of the master and slave image in .tif format. In this case, the master image was taken on the 28th of June 2019, while the slave image was taken on the 8th of July 2019.

By running the syntax as explained, the processing will be performed on default parameters. In order to have a high processing performance, a few parameters will be explained so that they can be easily modified.

- **SsResolOpt**: Is the subsampling parameter which represents the pixel size value for correlation. The default value is 4. Suggested values when working on earthquakes are 1 or 2. If the value is lowered the processing time increases, but the obtained results are sharper.

- **SzW**: Is the correlation window applied in the coregistration process. The default value is 4, which corresponds to a window of 9x9. More window options are 1 = 3x3, 2 = 5x5, 3 = 7x7 and so on. By increasing the window size, a more filtered displacement raster is obtained, but also fine features can be smoothed or even missed. The important consideration is that the window should be larger than the expected displacement. It is suggested to use values higher than 5 in case of landslides with large displacements.
- **DirMEC**: Is the custom name for correlation folder. The default name is MEC. The results of the coregistration will be saved inside this folder, where the most important files are Px1_Num6_DeZoom1_LeChantier.tif, Px2_Num6_DeZoom1_LeChantier.tif and Correl_LeChantier_Num_5.tif.

Having explained these editable parameters, examples of the new syntax for two different processing situations are:

```
mm3d MM2DPoSism T11SMV_20190628T182929_B04.tif T11SMV_20190708T182929_B04.tif SsResolOpt=1 SzW=3 DirMEC="Displacement_1/"
mm3d MM2DPoSism T11SMV_20190628T182929_B04.tif T11SMV_20190708T182929_B04.tif SsResolOpt=2 SzW=5 DirMEC="Displacement_2/"
```

D.3 Pixel to metric displacement conversion

After running the desired syntax for subpixel image coregistration, the displacement is obtained in pixel units, therefore; to assess the results, it is important to convert them into metric units. This process has to be done for EW and NS displacement as shown in equations D.1 and D.2, respectively.

$$NS \text{ component} = (Px2_Num6_DeZoom1_LeChantier.tif) * (-10m) \quad (D.1)$$

$$EW \text{ component} = (Px1_Num6_DeZoom1_LeChantier.tif) * (10m) \quad (D.2)$$

$$Total \text{ displacement} = \sqrt{(NS^2) + (EW^2)} \quad (D.3)$$

D.4 Additional processing steps

The results obtained after computing the displacement in metric units are still not able to be used because MM2DPoSism command does not keep the georeference.

A solution for this problem is obtained by creating a word file for one of the input Sentinel-2 images , for example. This process can be done using QGIS by the following steps:

1. Clic on *Raster* → *Conversion* → *Translate(Convert Format)*
2. Select T11SMV_20190628T182929_B04.tif in *Input Layer*
3. Select a path and give T11SMV_20190628T182929_B04 as the *Output File*
4. Clic in the pencil icon next to the box at bottom and add "-co worldfile=yes", as shown in figure D.2.

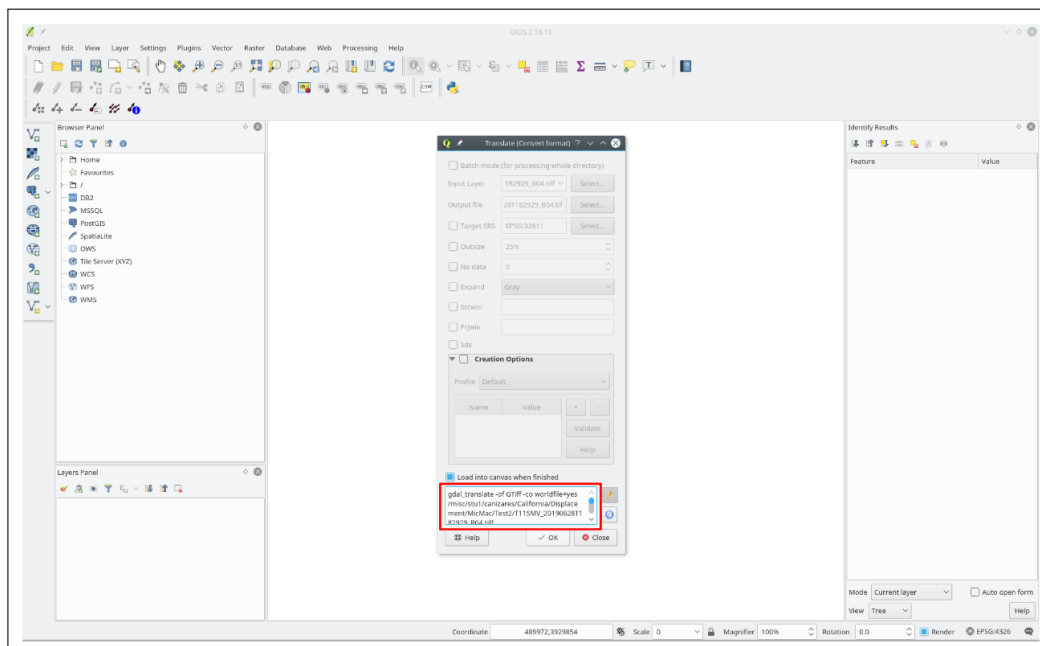


Figure D.2: Translate (Convert Format) parameters - QGIS

5. Check the two created files. One file should be given in .tif format, and the second one should be a .wld file.
6. Copy the .wld file inside the MEC folder three times, and rename them as Px1_Num6_DeZoom1_LeChantier.tfw, Px2_Num6_DeZoom1_LeChantier.tfw and Correl_LeChantier_Num_5.tfw.
7. Open the Px1_Num6_DeZoom1_LeChantier.tif file in QGIS and check if the coordinates correctly match with the region, as shown in figure D.3.
8. Compute the conversion from pixel to metric units. Clic on *Raster* → *Raster Calculator*, as shown in figure D.4.

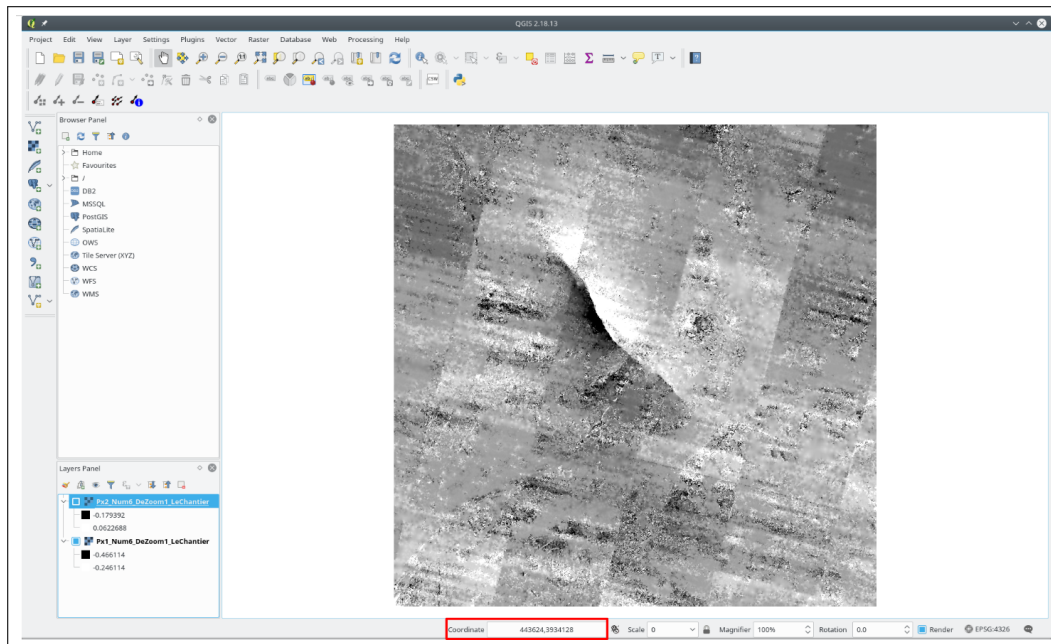


Figure D.3: EW direction georeferenced image - QGIS

9. Open the product showing the displacement in metric units but now using SNAP software. If the product is analyzed with the tool *Pixel Info*, information such as the displacement and the coordinates can be obtained, as shown in figure D.5. However, it is possible to see that the latitude - longitude and x-y coordinates are not correctly assigned.
10. Write the previous result as a GEOTIFF product using the `geotiffwrite` Matlab function. After this step, the coordinates can be checked again using SNAP in order to verify if they are correctly assigned. Figure D.6 shows the results of the product with the new coordinates.
11. Open the latest product in ENVI. Figure D.7 shows three zoom windows from different views of the product, which are useful to analyze the computed displacement. However, this last product is affected by noise which can be removed by applying a detrend procedure.
12. Apply step 6, 7 and 8 explained in appendix C in order to detrend, export and check the displacement for East/West and North/South component.

Figure D.8 shows the detrended product laying over the product affected by a trend. At first sight, the difference seems to be minimal; however, the displacement values shown in the bottom left corner vary significantly.

It is important to notice that once the detrended product has been exported as GeoTIFF, two files are generated. One file is, obviously the `.tif` product and the second is a `.tfw` file, also known as world file. A world file is commonly used by

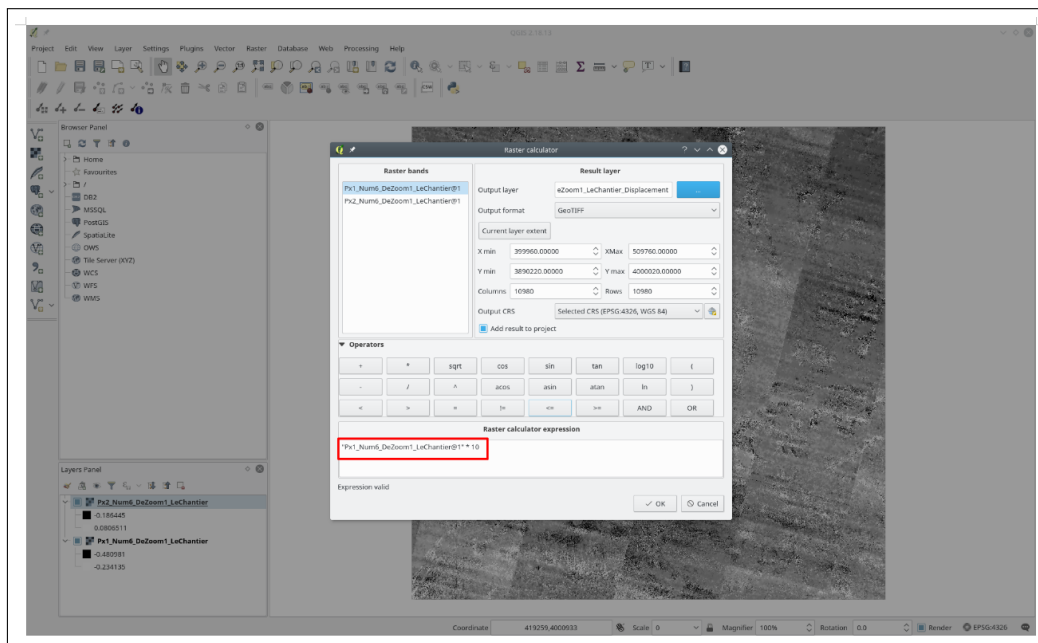


Figure D.4: Raster Calculator - QGIS

Geographic Information Systems (GIS) in order to georeference raster images. It consists of six coefficients of an fine transformation describing them as:

- Line 1: Pixel size in x-direction in map units (positive)
- Line 2: Rotation about y-axis
- Line 3: Rotation about x-axis
- Line 4: Pixel size in y-direction in map units (negative)
- Line 5: Upper left corner x-coordinate
- Line 6: Upper left corner y-coordinate

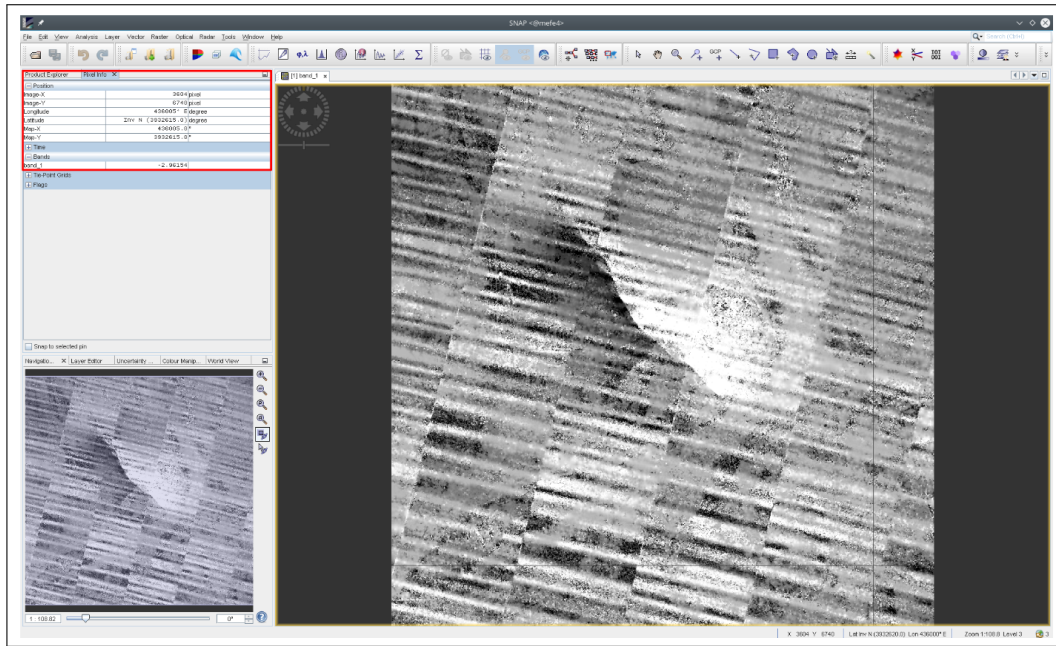


Figure D.5: Pixel information before geotiff conversion - SNAP

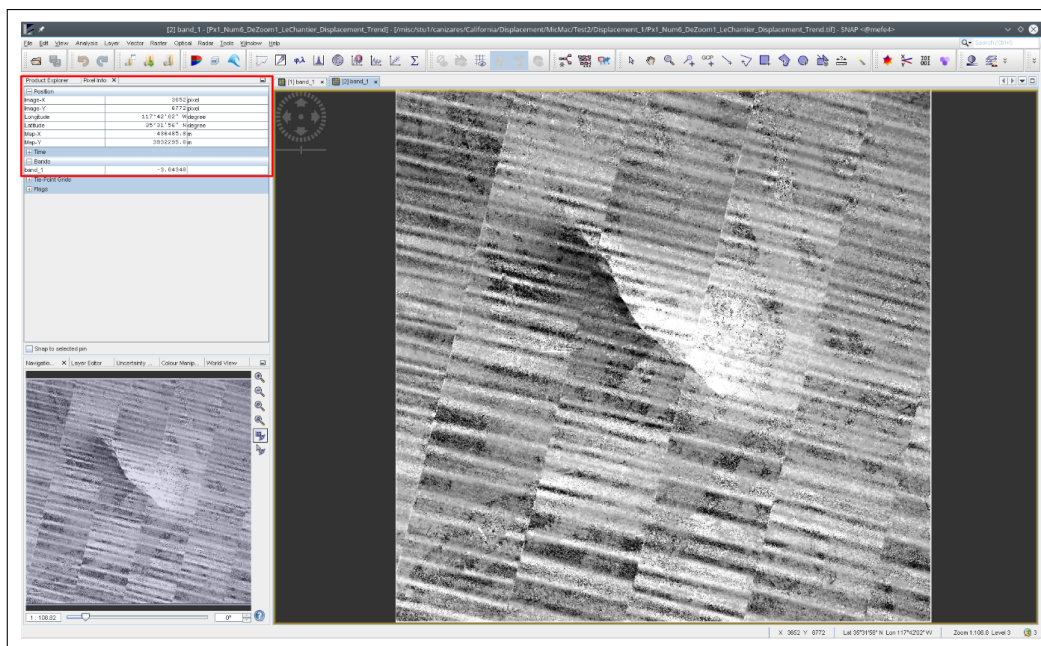


Figure D.6: Pixel information after geotiff conversion - SNAP

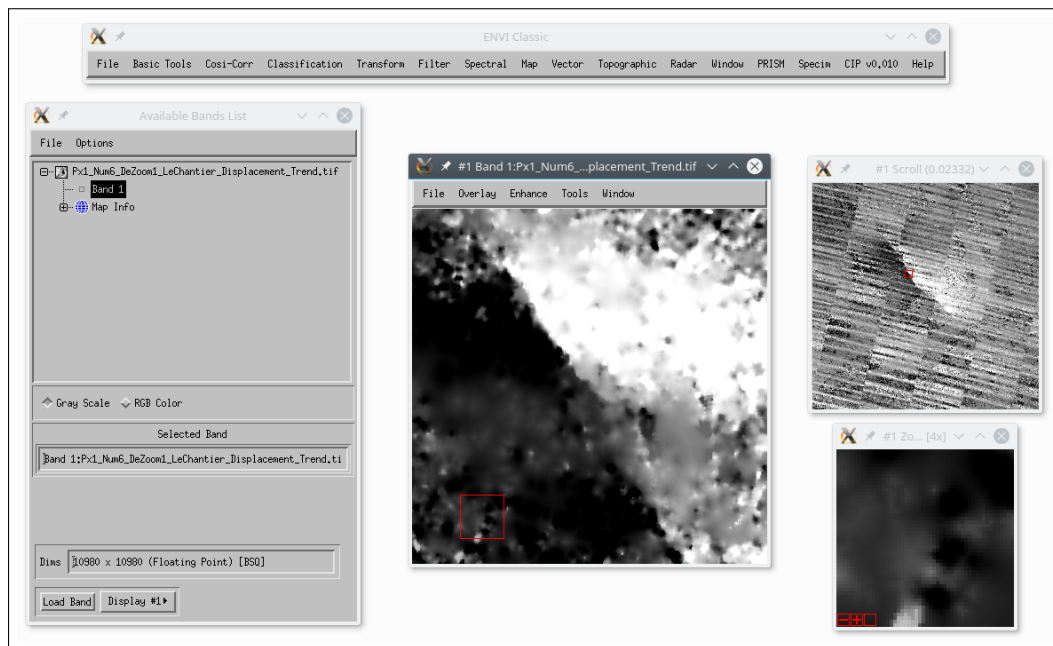


Figure D.7: Trended ground displacement - ENVI

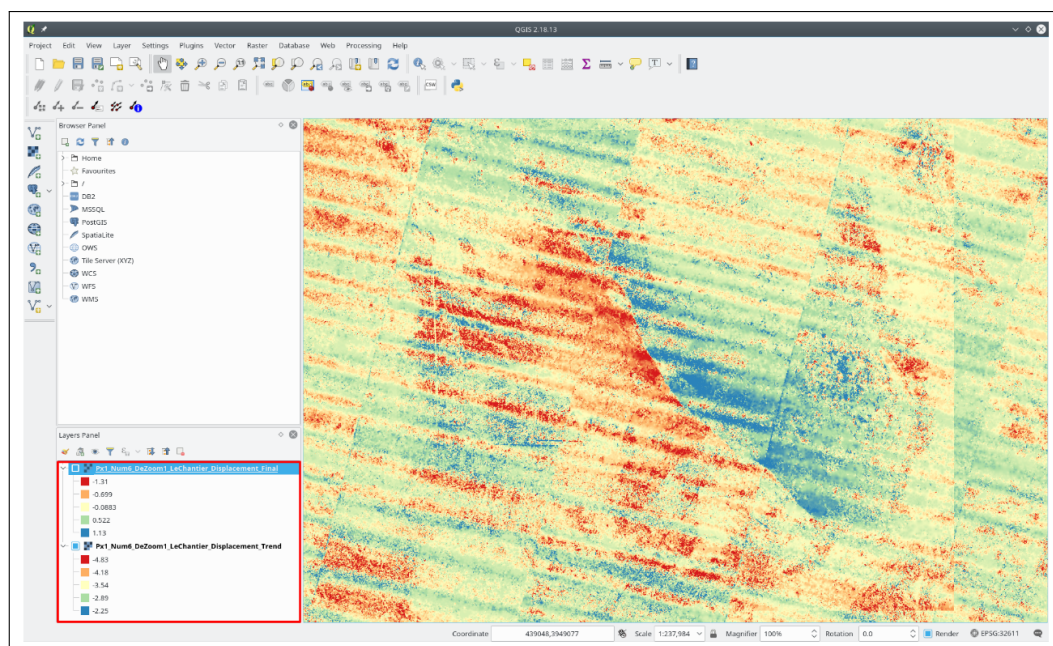


Figure D.8: Trended and Detrended Products - QGIS

Bibliography

- [Aati and Avouac, 2019] Aati, S. and Avouac, J. (2019). Surface deformation of the Mw 6.4 and Mw 7.1 Ridgecrest earthquakes measured from subpixel correlation of Copernicus Sentinel-2 optical images. <https://zenodo.org/record/3542274#.XkwS94wo9pg>, Last check: 17.02.2020.
- [Awange et al., 2010] Awange, J., Grafarend, E., Pálanicz, B., and Zaletnyik, P. (2010). Algebraic geodesy and geoinformatics. (ISBN: 978-3-642-12123-4).
- [Bagnardi, 2018] Bagnardi, M. (2018). Gbis user manual.
- [Bagnardi and Hooper, 2018] Bagnardi, M. and Hooper, A. (2018). Inversion of surface deformation data for rapid estimates of sources parameters and uncertainties: A bayesian approach. *Geochemistry, Geophysics, Geosystems*, 19:2194–2211.
- [Bechor, 2006] Bechor, N. (2006). *Extending Interferometric Synthetic Aperture Radar measurements from one to two dimesions*. PhD dissertation, Stanford University.
- [Chen et al., 2020] Chen, K., J, A., Aati, S., Milliner, C., Zheng, F., and Shi, C. (2020). Cascading and pulse-like ruptures during the 2019 ridgecrest earthquakes in the eastern california shear zone. *Nature Communication*, 11.
- [COSI-Corr, 2004] COSI-Corr (2004). COSI-Corr Software. http://www.tectonics.caltech.edu/slip_history/spot_coseis/download_software.html, Last check: 14.02.2020.
- [CRISP, 2001] CRISP (2001). Optical Remote Sensing. <https://crisp.nus.edu.sg/~research/tutorial/optical.htm>, Last check: 23.02.2020.
- [Decriem et al., 2010] Decriem, J., Árnadóttir, T., Hooper, A., Geirsson, H., Sigmundsson, F., Keiding, M., Ófeigsson, B., Hreinsdóttir, S., Einarsson, P., LeFemina, P., and Bennett, R. (2010). The 2008 may 29 earthquake doublet in sw iceland. *Geophysical Journal International*, 181:1128–1146.
- [Dzurisin, 2007] Dzurisin, D. (2007). *Volcano Deformation: Geodetic Monitoring Techniques*. Number ISBN: 978-3-540-49302-0. Praxis Publishing, Chichester.
- [Emardson et al., 2003] Emardson, T., Simons, M., and Webb, F. (2003). Neutral atmospheric delay in interferometric synthetic aperture radar applications: Statistical description and mitigation. *Journal of Geophysical Research*, 108:41–48.

- [Emery and Camps, 2017] Emery, W. and Camps, A. (2017). Introduction to satellite remote sensing: Atmosphere, ocean, land and cryosphere applications. (ISBN: 978-0-12-809254-5).
- [ESA, 2007] ESA (2007). Insar principles: Guidelines on sar interferometry processing and interpretation. *ESA Publications*, (ISBN: 92-9092-233-8).
- [ESA, 2012] ESA (2012). *Sentinel-1: ESA's Radar Observatory Mission for GMES Operational Services*. Number ISBN: 978-92-9221-418-0. ESA Communications, Leiden.
- [ESA, 2019a] ESA (2019a). Overview Copernicus. https://www.esa.int/Our_Activities/Observing_the_Earth/Copernicus/Overview3, Last check: 14.08.2019.
- [ESA, 2019b] ESA (2019b). Radar Course. https://earth.esa.int/web/guest/missions/esa-operational-eo-missions/ers/instruments/sar/applications/radar-courses/content-3/-/asset_publisher/mQ9R7ZVkJg5P/content/radar-course-3-introduction-to-interferometry, Last check: 16.08.2019.
- [ESA, 2019c] ESA (2019c). Sentinel-1 Mission. <https://sentinel.esa.int/web/sentinel/missions/sentinel-1>, Last check: 15.08.2019.
- [ESA, 2020a] ESA (2020a). Sentinel-2 Mission. <https://sentinel.esa.int/web/sentinel/missions/sentinel-2>, Last check: 12.01.2020.
- [ESA, 2020b] ESA (2020b). Sentinel Application Platform. <https://step.esa.int/main/toolboxes/snap/>, Last check: 18.02.2020.
- [Fiako, 2001] Fiako, Y. (2001). The complete (3-d) surface displacement field in the epicentral area of the 1999 mw 7.1 hector mine earthquake, california, from space geodetic observations. *Geophysical Research Letters*, 28:3063–3066.
- [Fielding et al., 2019] Fielding, E., Liu, Z., Stephenson, O., Zhong, M., Liang, C., Moore, A., Yun, S., and M, S. (2019). Surface deformation related to the 2019 mw7.1 and mw6.4 ridgecrest earthquakes in california from gps, sar interferometry, and sar pixel offsets. *Seismological Research Letters*.
- [Gabriel et al., 1989] Gabriel, A., Goldstein, R., and Zebker, H. (1989). Mapping small elevation changes over large areas: Differential radar interferometry. *Journal of Geophysical Research*, 94:9183–9191.
- [GAMMA, 2017] GAMMA (2017). GAMMA Remote Sensing. <https://www.gamma-rs.ch/>, Last check: 14.02.2020.
- [GAMMA, 2019] GAMMA (2019). Gamma software manual. (version 1.6).
- [Ghinali, 2018] Ghinali, C. (2018). Adjustment computation. (ISBN: 9781119390312).

- [Gradin et al., 2016] Gradin, R., Klein, E., Métois, M., and Vigny, C. (2016). Three-dimensional displacement field of the 2015 mw 8.3 illapel earthquake (chile) from across and along-track sentinel-1 tops interferometry. *Geophysical Research Letters*, 43:2552–2561.
- [Gupta, 2003] Gupta, R. (2003). *Remote Sensing Geology*. Springer, Berlin Heidelberg, second edition.
- [Hanssen, 2001] Hanssen, R. (2001). *Radar Interferometry: Data Interpretation and Error Analysis*. Number ISBN: 0-306-47633-9. Kluwer Academic, Dordrecht.
- [Hanssen et al., 1999] Hanssen, R., Weckwerth, T., Zebker, H., and R, K. (1999). High-resolution water vapor mapping from interferometric radar measurements. *Science*, 283:1297–1299.
- [Hartmann et al., 2018] Hartmann, K., Krois, J., and Waske, B. (2018). E-Learning Project SOGA: Statistics and Geospatial Data Analysis. Department of Earth Sciences, Freie Universitaet Berlin. <https://www.geo.fu-berlin.de/en/v/soga/Geodata-analysis/geostatistics/Geostatistical-Interpolation/Modeling-the-Semivariogram/index.html>, Last check: 23.02.2020.
- [Henderson and Lewis, 1998] Henderson, F. and Lewis, A. (1998). *Principles and Applications of Imaging Radar*, volume 2. John Wiley Sons, New York, third edition.
- [Hu et al., 2012] Hu, J., Li, Z., Ding, X., and Zhu, J. (2012). 3d coseismic displacement of 2010 darfield, new zeland earthquake estimated from multi-aperture insar and d-insar measurments. *Journal of Geodesy*, 86:1029–1041.
- [Hu et al., 2014] Hu, J., Li, Z., Ding, X., Zhu, J., Zhang, L., and Sun, Q. (2014). Resolving three-dimensional surface displacements from insar measurements: A review. *Earth Science Reviews*, 133:1–17.
- [IREA, 2020] IREA (2020). Optical Remote Sensing. http://www.irea.cnr.it/en/index.php?option=com_k2&view=itemlist&task=category&id=1&Itemid=161, Last check: 08.02.2020.
- [Jónsson et al., 2002] Jónsson, S., Zebker, H., Segall, P., and F, A. (2002). Fault slip distribution of the 1999 mw 7.1 hector mine, california, earthquake, estimated from satellite radar and gps measurements. *Bulletin of the Seismological Society of America*, 92:1377–1389.
- [Khorram et al., 2012] Khorram, S., van der Wiele, C., Nelson, S., and Koch, F. (2012). Remote sensing. (ISBN: 978-1-4614-3102-2).
- [Kubik, 1970] Kubik, K. (1970). The estimation of weights of measured quantities within the method of least squares. *Bulletin Géodésique (1946-1975)*, 95:21–40.

- [L3Harris, 2019] L3Harris (2019). Idl data types. https://www.harrisgeospatial.com/docs/IDL_Data_Types.html.
- [Liang et al., 2012] Liang, S., Li, X., and Wang, J. (2012). Advanced remote sensing. (ISBN: 978-0-12-385954-9).
- [Massonnet and Feigl, 1998] Massonnet, D. and Feigl, K. (1998). Radar interferometry and its applications to changes in the earth’s surface. *Reviews of Geophysics*, 36:441–500.
- [Massonnet et al., 1993] Massonnet, D., Rossi, M., Carmona, C., Adragna, F., Peltzer, G., Feigl, K., and Rabaute, T. (1993). The displacement field of the landers earthquake mapped by radar interferometry. *Nature*, 364:138–142.
- [Massonnet and Souyris, 2008] Massonnet, D. and Souyris, J.-C. (2008). Imaging with synthetic aperture radar. (ISBN: 978-2-940222-15-5).
- [Mehrabi et al., 2019] Mehrabi, H., Voosoghi, B., Motagh, M., and Hassen, R. (2019). Fields from insar through tikhonov regularization and least-squares variance component estimation. *Journal of Surveying Engineering*, 145:2736–2749.
- [MicMac, 2018] MicMac (2018). MicMac Software. <https://micmac.engg.eu/index.php/accueil>, Last check: 14.02.2020.
- [Milliner and Donnellan, 2020] Milliner, C. and Donnellan, A. (2020). Using daily observations from planet labs satellite imagery to separate the surface deformation between the 4 july mw 6.4 foreshock and 5 july mw 7.1 mainshock during the 2019 ridgecrest earthquake sequence. *Seismological Research Letters*, 364:1–12.
- [Motagh et al., 2010] Motagh, M., Schurr, J., Anderssohn, B., Cailleau, T., Walter, T., Wang, J., and Villotte, P. (2010). Subduction earthquake deformation associated with 14 november 2007, mw 7.8 tocopilla earthquake in chile: Results fom insar and aftershocks. *Tectonophysics*, 490:60–68.
- [Rosen, 2014] Rosen, P. (2014). Principles and theory of radar interferometry. *Jet Propulsion Laboratory*.
- [Rosu et al., 2015] Rosu, A., Pierrot-Deseilligny, M., Delorme, A., Binet, R., and Klinger, Y. (2015). Measurement of ground displacement from optical satellite image correlation using the free open-source software micmac. *ISPRS Journal of Photogrammetry and Remote Sensing*, 100:48–59.
- [Scheffler et al., 2017] Scheffler, D., Hollstein, A., Diedrich, H., Segl, K., and Hostert, P. (2017). Arosics: An automated and robust open-source image co-registration software for multi-sensor satellite data. *Remote Sensing*, 9.
- [Simons and Rosen, 2015] Simons, M. and Rosen, P. (2015). Interferometric synthetic aperture radar geodesy. *Treastise of Geophysics*, pages 391–446.

- [Skolnik, 1981] Skolnik, M. (1981). *Introduction to Radar Systems*. Number ISBN: 0-07-057909-1. McGraw-Hill, Singapore.
- [SkyGeo, 2020] SkyGeo (2020). Insar technical background. <https://www.skygeo.com/insar-technical-background/>, Last check: 27.02.2020.
- [Stachniss, 2015] Stachniss, C. (2015). Photogrammetry I - Matching. *Lecture Notes Summer Semester 2015*.
- [Sudhaus and Jónsson, 2009] Sudhaus, H. and Jónsson, S. (2009). Improved source modelling through combined use of insar and gps under consideration of correlated data errors: application to the june 2000 kleifarvatn earthquake, iceland. *Geophysical Journal International*, 176:389–404.
- [Sudhaus and Jónsson, 2011] Sudhaus, H. and Jónsson, S. (2011). Source model for the 1997 zirkuh earthquake (mw=7.2) in iran derived from jers and ers insar observations. *Geophysical Journal International*, 185:676–692.
- [Valkaniotis, 2019] Valkaniotis, S. (2019). Subpixel optical correlation co-seismic offsets fro the Mw 6.4 and Mw 7.1 Ridgecrest, California earthquakes, from Copernicus Sentinel-2 data. https://zenodo.org/record/3275073#.XkaVnzMo_OE, Last check: 14.02.2020.
- [Van Puymbroeck et al., 2000] Van Puymbroeck, N., Michel, R., Binet, R., Avouac, J., and Taboury, J. (2000). Measuring earthquakes from optical satellite images. *Applied Optics*, 39:3486–3494.
- [Veci, 2015] Veci, L. (2015). Tops interferometry tutorial. *ESA*.
- [Webster and Oliver, 2007] Webster, R. and Oliver, M. (2007). *Geostatistics for environmental scientists*. (ISBN: 978-0-470-02858-2).
- [Wegnüller et al., 2016] Wegnüller, U., Werner, C., Strozzi, T., Wiesmann, A., and Frey, O. (2016). Sentinel-1 support in the gamma software. *Procedia Computer Science*, 100:1305–1312.
- [Wener et al., 2005] Wener, C., Wegmüller, U., Strozzi, T., and Wiesmann, A. (2005). Precision estimation of local offsets between pairs of sar slcs and detected sar images. *Proceedings in international geoscience and remote sensing symposium*, pages 4803–4805.
- [Wright et al., 2004] Wright, T., Parsons, B., and Lu, Z. (2004). Toward mapping surface deformation in three dimensions using insar. *Geophysical Research Letters*, 31:L01607.
- [Xu et al., 2019] Xu, X., Sandwell, D., and B, S.-K. (2019). Co-seismic displacements and surface fractures from sentinel-1 insar: 2019 rigdecrest earthquakes. *Seismological Research Letters*, pages 1–7.

- [Yun, 2007] Yun, S.-H. (2007). *Volcano Deformation Modeling Using Radar Interferometry: A Mechanical Model of the Large-deformation 2005 Sierra Negra Volcanic Eruption Derived from InSAR Measurements*. Number ISBN: 978-3-8364-7598-3. VDM Verlag, Saarbrücken.
- [Zebker and Villasenor, 1992] Zebker, H. and Villasenor, J. (1992). Decorrelation in the interferometric radar echoes. *IEEE Transactions on Geoscience and Remote Sensing*, 30:950–959.